
The interplay of magnetic fields and star formation processes using SPMHD simulations

Eirini Batziou



Munich 2018

Das Zusammenspiel von Magnetfeldern und Sternenstehung in Galaxien unter der Benutzung von SPMHD Simulationen.

Masterarbeit
an der Universitäts Sternwarte München
der Ludwig–Maximilians–Universität
München

vorgelegt von
Eirini Batziou
Matrikelnummer: 11615009
aus Athen, Griechenland

betreut von PD Dr. Klaus Dolag

München, den 20. Aug 2018

The interplay of magnetic fields and star formation processes using SPMHD simulations

Master Thesis
at the University Observatory Munich
Ludwig-Maximilians-University of Munich

submitted by
Eirini Batziou
Matriculation Number: 11615009
from Athens, Greece

Supervised by PD Dr. Klaus Dolag

Munich, 20 of August 2018

Contents

Abstract	ix
1 Introduction	1
1.1 Magnetic Fields in Galaxies	2
1.1.1 Detection Methods	2
1.1.2 Origin of magnetic fields in galaxies and amplification	3
1.1.3 Magnetic fields and Star Formation	5
1.2 Numerical Simulations	6
1.2.1 Gravitational Dynamics	6
1.2.2 Hydrodynamics	7
1.2.3 Additional Physics	11
2 Star Formation models	15
2.1 Star Formation model in GADGET	15
2.1.1 The sub-grid model	15
2.1.2 Selection of parameters	20
2.1.3 Code implementation	23
2.2 An alternative formulation of the model	23
2.2.1 Model equations	24
2.3 Pressure based star formation model	29
2.3.1 Equations of the multiphase model	29
2.3.2 Selection of parameters	34
2.4 Magnetic seeding model	38
2.4.1 Supernova seeding model equations	39
3 Simulations	41
3.1 MHD shock tube tests	41
3.2 Simulations of isolated disk galaxies	45
3.2.1 Numerical set up	45
3.2.2 Results: Galaxy with SH03 star formation model	47
3.2.3 Results: Galaxy with the new, pressure based, star formation model	51
3.3 Simulations of an idealized disk galaxy with a gas halo	58
3.3.1 Numerical set up	58

3.3.2 Results	59
4 Summary and Conclusions	79
Aknowledgements	109

Abstract

Cosmological simulations deal with very large structures and there is not enough resolution to couple all the dynamical range of processes taking place, so it is very important to model consistently phenomena that occur in unresolved scales. One example of sub-resolution model is proposed by [Springel and Hernquist, 2003] in which the star formation and the supernova feedback can be modeled by a multiphase structure of the Interstellar Medium (ISM). In their approach, the ISM consists of cold and hot gas and includes radiative heating, cooling, star formation and feedback from supernova. This model predicts a self-regulated star formation quiescent mode for the gaseous part of disk galaxies and has only one free parameter: the overall time-scale for star formation. First improvement of this model is to express the star formation rate in terms of external pressure, which allows to include further physical processes such as magnetic fields. This is done by assuming that the cold and hot phase of the ISM are in pressure equilibrium [Murante et al., 2010] and the star formation arises from the molecular fraction of the gas, which is proportional to external pressure [Blitz and Rosolowsky, 2006]. After implementing the MHD extension of the star formation model in GADGET code [Springel, 2005, Springel et al., 2001] and having studied the behaviour of this model with simulations, we then can include a more complicated feedback model including magnetic field seeding from Supernova (SN) [Beck et al., 2013]. In particular, as it has already confirmed that the magnetic field in protogalaxies can be produced by the dynamo effect in contracting protostars [Bisnovatyi-Kogan et al., 1973]. Mass loss by stars and SN explosions can then enrich the ISM with magnetic fields and provide a seed field in the galactic dynamo. It is interesting to examine how this feedback model works with the MHD extension of the star formation model in idealized disk galaxies.

Chapter 1

Introduction

Galaxies have been a topic of extensive research in Astronomy and Astrophysics over many years. The first observations of galaxies were done by ancient Greeks, Arabs and Persians who noticed that the bright nebula along the night sky is a celestial and not an atmospheric object. However was not until the late 16th century when Charles Messier cataloged various nebulae throughout the sky and classified several of them as spiral nebulae. At that time, these 'nebulae' were thought to be part of our Milky Way and only in 1924, Edwin Hubble, could resolve their structure and the stars using a large telescope. Thus, he calculated the distance of these objects which was found to be significantly larger than the distance between the Earth and the center of the Milky Way. After that, the research in galaxies remained particularly active since scientists used different wavebands in order to observe them.

Apart from the rich observational data that we nowadays have for galaxies it is equally important to develop the theoretical understanding of the physics that governs these objects. Gravitational dynamics cannot offer an analytic solution for a bound system of more than 2 objects. Therefore, the need of the development of numerical methods is inevitable. The first methods to numerically solve physical problems were developed in the 1950s and with the continuously rising computational power the progress is exponential. In the field of galaxies and large structures the numerical methods are significant due to the large amount of processes and coupled phenomena that are taking place. For example, particle-in-cell (PIC) [Harlow and Evans, 1955] and particle-mesh (PM) [Hockney and Eastwood, 1988, Efstathiou et al., 1985], direct N-body simulations [Press and Schechter, 1974], as well as grid-free (particle methods) [Gingold and Monaghan, 1977, Lucy, 1977] methods for fluids are used in the codes in order to solve the equations that describe the astrophysical systems. Initially, the numerical simulations of galaxies were performed taking only into consideration the gravitational interaction between particles, i.e. stars and the gas interactions which are described by hydrodynamics. However, recently, the codes for galaxies include many more complicated processes, such as cooling [Katz et al., 1995], star formation [Yepes et al., 1997, Hu et al., 2016, Springel and Hernquist, 2003], turbulence [Chorin, 1967], magnetic fields [Dolag and Stasyszyn, 2009] or thermal conduction [Dolag et al., 2004].

With these two powerful tools, we are able to study in detail the formation and evolution of galaxies. Thereby, it is important to be based on the acquired theoretical knowledge but also to keep in mind the observational constraints in order to build realistic models for galaxies. This is the main driven force of this thesis, in which we try to couple the magnetic field in the galaxies with the star formation processes in the framework of numerical simulations.

1.1 Magnetic Fields in Galaxies

Magnetic Fields ¹ are ubiquitous in the Universe and observed in different scales, from the interior of stars to galaxies and galaxy clusters. They are always present where ionized matter is involved and thus a major component of the dynamics in the visible matter. The first detection of magnetic fields in galaxies came in 1932 when the radio emission of the Milky Way was measured.

1.1.1 Detection Methods

There are various ways to measure the magnetic field in astrophysics. A very common phenomenon is the optical and far-infrared polarization of the light from a distant luminous source. The particles (usually dust grains) that are located between the source and the observer can have random orientation but a few of them could be oriented with their major axis parallel to the magnetic field. This leads to polarization of the light which is an indicator of the perpendicular component of the magnetic field B_{\perp} .

Synchrotron radiation is a smoking gun of the existence of magnetic fields since it is produced when charged particles are moving around magnetic field lines. In the Milky Way the cosmic rays propagating through the interstellar magnetic fields are the origin of the diffuse radio emission. The energy spectrum of the cosmic-ray electrons is linked to the resulting energy spectrum of the synchrotron emission. To be more specific, a power-law energy spectrum of cosmic-ray electrons with spectral index of γ produces a power-law synchrotron spectrum $I \sim \nu^{\alpha}$, with spectral index $\alpha = (\gamma + 1)/2$. The maximum of the synchrotron radiation can be approximated as $\nu_o \approx \frac{1}{2\pi} \frac{qB}{mc} \gamma^2$, which is written as $\nu_o \approx 2 \cdot 10^6 B \gamma^2$ Hz for electrons with Lorentz factor γ . With this way we can estimate the magnetic field if we know properties of the electron energy distribution and the other way around. In order to determine the magnetic field, usually we make the assumption that is in energy equipartition with the cosmic rays and the turbulent gas motions of the interstellar medium. Thus, their energy densities are comparable :

$$U_{\text{cosmic rays}} \sim \frac{B_{\text{tot}}^2}{8\pi} \sim \frac{\rho v^2}{2}. \quad (1.1)$$

¹For this section we follow the review of [Beck, 2016]

Another popular way of detecting magnetic field is through Faraday rotation, which causes a rotation of the plane of polarization which is linearly proportional to the component of the magnetic field in the direction of propagation. The rotation angle β is given by

$$\beta = \lambda^2 RM, \quad (1.2)$$

where λ is the wavelength of the observation and RM the Rotation Measure, which is calculated as

$$RM = \frac{e^3}{2\pi m^2 c^4} \int_o^d n_e(s) B_{\parallel}(s) ds. \quad (1.3)$$

In the last equation, e is the charge of the electron, c is the speed of light in vacuum, m is the mass of the electron, $n_e(s)$ is the density of the electrons and B_{\parallel} is the magnetic field along the line of sight. The magnetic field of the galaxy can be split into two components, the regular and turbulent field. The regular field is sensitive to the field direction so only these fields give rise to Faraday rotation.

The most direct way of detecting the magnetic field in astrophysical context is the Zeeman effect [Zeeman, 1897]. When magnetic field is present, the spectral lines of an atom are split into two components with frequency

$$\nu_o \pm \frac{eB_{\parallel}}{4\pi mc} \quad (1.4)$$

with ν_o the frequency without any external field. Thus, knowing the theoretical values of the emission lines we can easily determine the magnetic field in the line of sight.

1.1.2 Origin of magnetic fields in galaxies and amplification

In order to build up the observed magnetic field of a spiral galaxy we need a way to seed it, a way to amplify it and finally a way to order and sustain it. The origin of the first magnetic fields in the Universe is still highly debated. The large scale intergalactic magnetic field, in the order of 10^{-12} G could have primordial origin, i.e., could be generated in the early Universe according to [Durrer and Neronov, 2013]. A common belief is the well known Biermann battery [Biermann, 1950, Xu et al., 2008]. The Biermann battery is a process to seed very weak magnetic field from zero initial conditions, which happens if we add an extra term in the Ohms law. However the large scale primordial field is hard to be maintained in galaxies due to their differential rotation which winds up the magnetic field. A seed magnetic field is considered to be generated in protogalaxies or in the intergalactic medium due to Weibel-type instabilities [Lazar et al., 2009], [Schlickeiser, 2012]. Another scenario is that seed fields came from the first black holes, stars or supernovae explosions [Hanayama et al., 2005]. Whichever is the origin of the seed or primordial fields, these should be amplified in order to reach observable values. An efficient way to amplify the fields is the small scale dynamo within a timescale of 10^6 yrs. This includes turbulence in the gas produced by supernovae explosions [Ferriere, 1996] or by spiral shocks [Kim et al., 2006]. The small scale dynamo can amplify seed fields in

fields with strength of μG and results in a turbulent magnetic field configuration. The ordering of the turbulent magnetic fields in galaxies is a result of the differential rotation of the gas [Kotarba et al., 2009], which is supported by the magneto-rotational instability [Pakmor and Springel, 2013]. The most prominent way to sustain the ordered magnetic field in galactic scales is the $\alpha - \Omega$ dynamo with a timescale of 10^8 yrs [Beck et al., 1996]. This occurs due to the differential rotation (Ω - effect) of gas flows driven by supernova explosions or cosmic rays, carrying magnetic fields which are twisted from the Coriolis force (α - effect) in addition to magnetic diffusivity. This is called mean field approximation, because the small and large scale effects can be mathematically separated in the equation following the evolution of the magnetic field, which is written as

$$\frac{\partial \mathbf{B}}{\partial t} = \nabla \times (\mathbf{v} \times \mathbf{B}) + \nabla \times \alpha \mathbf{B} + \eta \nabla^2 \mathbf{B}. \quad (1.5)$$

In equation (1.5) the first term in the left-hand side expresses the amplification through the large-scale velocity field of the galaxy, the second term represents the α effect and the last one the losses due to magnetic diffusivity. Studies [Beck et al., 1994], [Arshakian et al., 2009] show that the mean field approximation in galactic disks generate large ordered fields from turbulent magnetic fields within 1 Gyr. The total magnetic field of a galaxy is calculated as the vector sum of the turbulent magnetic field that is generated from the small scale dynamo and the ordered magnetic field which is generated from the large scale $\alpha - \Omega$ dynamo. Both actions are needed in order to reach observable values and configurations. Among spirals the total magnetic field is found to be $B_{tot} = 9 \pm 2 \mu G$, [Niklas, 1995]. Gas rich galaxies have total magnetic field strengths of $20 - 30 \mu G$ while in starburst galaxies the field strength can reach values up to $50 - 100 \mu G$ (i.e. [Adebahr et al., 2013]). In order to estimate the significance of the magnetic fields, it is useful to compare the energy densities of different components of the interstellar medium (ISM). These are: the magnetic field, the turbulence of the neutral gas, the cosmic rays and the thermal energy density of the warm ionized gas of the ISM.

An observational example is shown in figure 1.1, in which the radial variations of the energy densities in the galaxy IC 342 are shown. The component of the turbulent motion of the neutral gas in the ISM is shown in blue, the total magnetic field in black, the cosmic rays, which are in equipartition with the ordered magnetic field, in green and the thermal energy of the warm gas in red ($T = 10^4 K$). The radial profiles show that the ISM is a low β plasma since the magnetic energy density is higher than the thermal. Although the turbulence is higher near the center of the galaxy, the magnetic field dominates in the outer parts. These results are similar to the observational outcomes of [Cox, 2005] for the Milky way. Therefore, it is clear that the magnetic fields are dynamically important for the physics of the interstellar medium and their presence and effects should be taken into consideration in galaxy formation simulations.

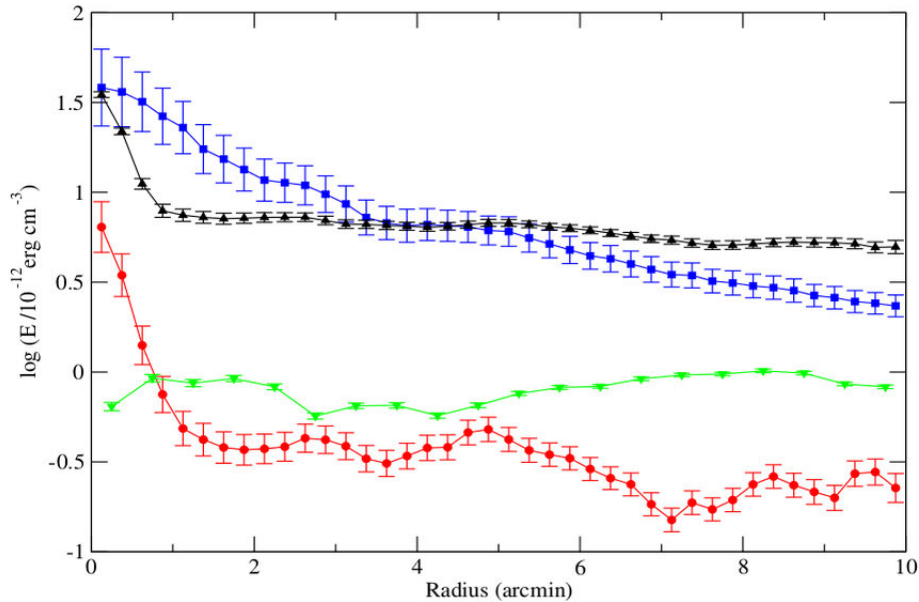


Figure 1.1: Energy densities of different components of the ISM. The component of the turbulent motion of the neutral gas is shown in blue, the total magnetic field in black, the cosmic rays, which are in equipartition with the ordered magnetic field, in green and the thermal energy of the warm was in red ($T = 10^4$ K). Taken from [Beck, 2016]

1.1.3 Magnetic fields and Star Formation

As magnetic fields are a significant component of the ISM, it is important to understand how they affect or are affected by the star formation in a galaxy. A global correlation holds between the total radio emission of a galaxy, which has synchrotron origin, and the infrared luminosity of star-forming galaxies. This is a tight correlation that holds for many orders of magnitude and is slightly non-linear in log-log scale (exponent 1.09 ± 0.005) [Bell, 2003]. [Schleicher and Beck, 2013] explain this correlation by relating star formation and magnetic field strength in terms of turbulent magnetic field amplification, where turbulence is a result of supernova feedback. Observations [Tabatabaei et al., 2013] show a correlation between the magnetic fields and the star formation density of a galaxy. In this study they investigated the correlation between the radio continuum (synchrotron) and the far-infrared emission of NGC 6976 using *Herschel*. With these observations it is possible to determine the magnetic field strengths of the galaxy and star formation activity. In figure 1.2 is shown that the total and turbulent magnetic field strength are correlated with the star formation density Σ_{SFR} . This correlation points out that turbulent magnetic fields are efficiently produced in active star forming regions, which agrees with previous studies [Chyży, 2008]. In star forming regions feedback mechanisms, such as supernovae, increase the turbulence of the ISM. This can be a seed to the small scale dynamo that was previously discussed in order to amplify the turbulent magnetic field.

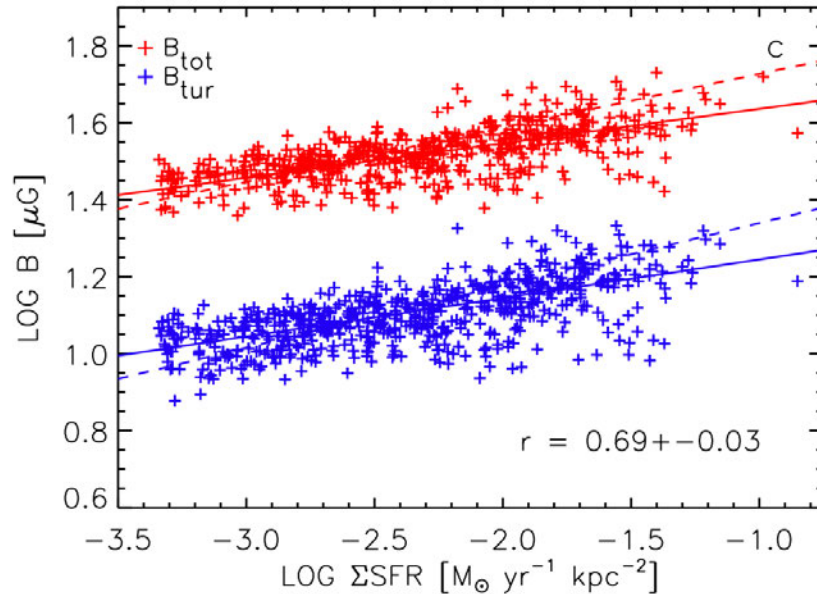


Figure 1.2: Magnetic field strengths (total and turbulent) measured by the degree of polarization versus the surface density of the star formation rate. [Tabatabaei et al., 2013]

1.2 Numerical Simulations

Numerical simulations are an important tool in modern astrophysics that has shown rapid progress over the last decades. Different methods have been developed in order to solve the equations that govern the dynamics of the Universe. Cosmological simulations are crucial in the understanding of structure formation and explaining the dynamics of large structures such as galaxies and galaxy clusters. The first and simplest simulations of galaxies were the N-body simulations and were done considering only gravitational interactions between particles [Press and Schechter, 1974], which was an evolution of the restricted 3 body problem [Toomre and Toomre, 1972]. Apart from the N-body simulations, the need of understanding additional physical processes gave rise to the development of new hydrodynamic methods. The two general categories of numerical schemes in order to discretize continuous quantities are the particle methods, which discretize mass and the grid methods, which discretize space. Here we are using the particle based cosmological code GADGET [Springel et al., 2001, Springel, 2005]. Its basic characteristics will be explained below.

1.2.1 Gravitational Dynamics

Gravity is the main driving force of the structure formation, since dark matter dominates over baryons in the Universe and thus is the core of any cosmological code. For the calculation of the gravitational force between the particles the most obvious way is the direct summation of the force between all the particles. This computation would result in

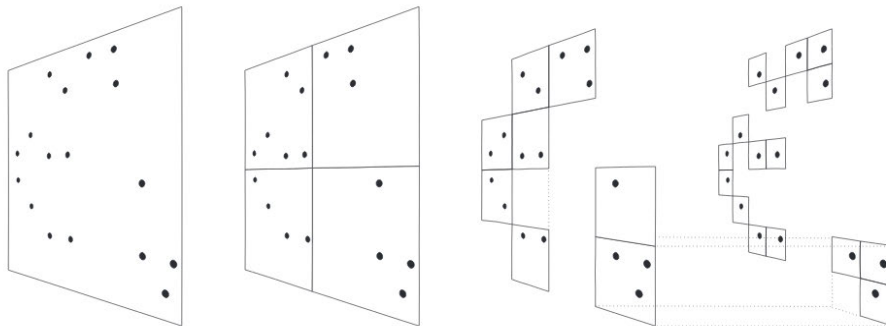


Figure 1.3: Schematic representation of the oct-tree method (2D). The particles are first included in a single cube (root node) and then are every time divided until one node includes one particle. Taken from [Springel et al., 2001].

the accurate result that comes from the total gravitational potential, however, it is rather expensive and requires $\mathcal{O}(N^2)$ calculations. An alternative way to perform this calculation is by computing the gravitational acceleration with a single interaction with a node of the "tree structure", where one node contains a corresponding set of particles. The number of operations required for the calculation of the accelerations of all particles decreases to $\mathcal{O}(N \log N)$. This method is called the Tree method and has many alternatives. The main idea behind this method is that particles are grouped together into nodes so the contribution of distant particles is computed as a single force. An example of a tree algorithm is the *oct tree*, in which all particles are contained in a cube (node). Then this cube is split in its 8 octants and each one of the smaller cube is split to its 8 octants as well. This procedure ends when there is one or no particles in the last cube. The last level of cubes are the "leaves" of the tree. The calculation of the gravitational force is done by starting at the first cube and then "walking" in the different branches taking into consideration the importance of each branch. An illustration in 2D of the oct-tree is shown in figure 1.3. Another way of a tree algorithm is the binary tree which follows the opposite procedure. First the calculation of the force starts at the leaves - i.e. final stages of the tree - and stops at the root node.

1.2.2 Hydrodynamics

In particle codes like GADGET the method to solve the hydrodynamic equations is called Smooth particle Hydrodynamics (SPH)² and is a Lagrangian method. SPH is a technique of solving numerically the hydrodynamic equations by discretizing the mass of the fluid. Was developed in astrophysics by [Gingold and Monaghan, 1977] and [Lucy, 1977]. In this case the particles are acting as markers in order to discretize and solve the equations of hydrodynamics:

²For this section we follow the review of [Price, 2012]

$$\begin{aligned}\frac{d\rho}{dt} + \rho \nabla \cdot \mathbf{v} &= 0 \\ \frac{d\mathbf{v}}{dt} + \frac{\nabla P}{\rho} &= 0 \\ \frac{du}{dt} + \frac{P}{\rho} \nabla \cdot \mathbf{v} &= 0\end{aligned}$$

with $\frac{d}{dt} = \frac{\partial}{\partial t} + \mathbf{v} \cdot \nabla$. From the last set of equations the first equation is the mass continuity equation, the second are the Euler or momentum equations and the last is the energy conservation equation. Before thinking how the hydrodynamic equations are written in SPH formulation, we should answer the fundamental question, how to compute the density from a random distribution of particles. The most simple approach is to construct a grid including all the particle distribution and calculate the mean density in each cell. This particle-mesh approach is shown in the left panel of figure 1.4. However this method can easily over/underestimate regions of the system in the case of highly anisotropic particle distribution. Another way, shown in the middle panel of figure 1.4, is to remove the grid and calculate the density by sampling the local particle distribution. This can be a noisy estimator since there is an uncertainty if one particle in the edge of the sampling region is considered to be part of it or not. The further and natural evolution of this method is to sample the local particle distribution by smoothing it according to the distance between the central region and other particles. That means that particles that are located further away have smaller contribution in the density calculation. This is called kernel density estimator and the density is written as

$$\rho_i = \sum_j m_j W_{ij}(x_{ij}, h) \quad (1.6)$$

for a particle with density ρ_i , position denoted by the vector \mathbf{r}_i and relative distance x_{ij} between the particles i and j . W is the weight function (or smoothing kernel) and h is a characteristic scale that is also function of density:

$$h(x_i) = \eta \left(\frac{m_i}{\rho_i} \right)^{1/3} \quad (1.7)$$

and η is the ratio of the smoothing length to the mean distance between particles. The kernel function cannot be any random function but should fulfill a couple of properties.

The kernel should have:

- a positive weighting, should decrease monotonically with the relative distance of the particles x_{ij} and have smooth derivatives
- symmetry with respect to the relative distance of 2 particles, i.e., $W(x_{ij}, h) = W(x_{ji}, h)$

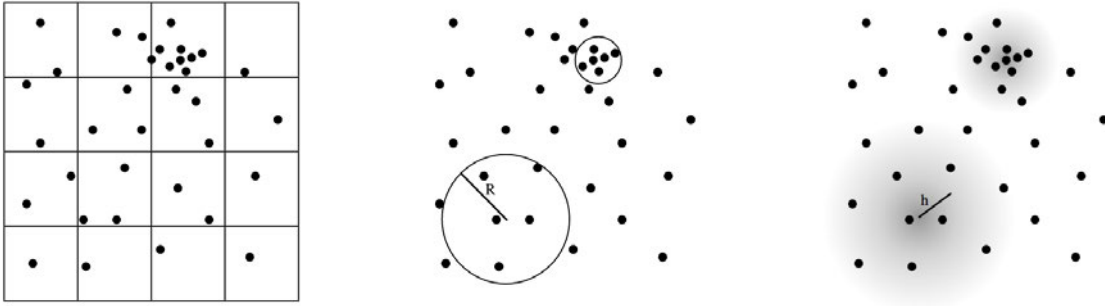


Figure 1.4: Different approaches to calculate the density from a random particle distribution. Left panel: particle-mesh method, central panel: calculation doing local sampling of the density, right panel: kernel density estimator. Taken from [Price, 2012].

- a flat behaviour in the center of the particle distribution so with a small change in the particle's position will not affect the density estimation

For all the simulations performed here we use the Wendland C4 kernel [Dehnen and Aly, 2012].

If we write the kernel W as $W(x_{ij}, h) = \frac{1}{h^d} w(q)$. with $q = x_{ij}/h$, then the function $w(q)$ for the Wendland C4 kernel is

$$w(q) = \frac{495}{32\pi} (1 - q)^6 \left(1 + 6q + \frac{35}{3} q^2 \right) \quad (1.8)$$

For $q > 1$ the function w is set to $w(q) = 0$ and this kernel function needs 200 neighbours in 3 dimensions.

The Lagrangian of a discretized system of point masses m_i is written as

$$\mathcal{L} = \sum_i m_i \left(\frac{1}{2} v_i^2 - u_i \right) \quad (1.9)$$

where v_i is the velocity of the particle i and u_i its internal energy. The equations of motion for the system are derived from the principle of least action $S = \int L dt$ such that $\delta S = \int \delta L dt = 0$. Thus the SPH expression of the equations of motion is

$$\frac{d\mathbf{v}_i}{dt} = - \sum_j m_j \left(f_i^{co} \frac{P_i}{\rho_i^2} \frac{\partial W_{ij}(h_i)}{\partial \mathbf{r}_i} + f_j^{co} \frac{P_j}{\rho_j^2} \frac{\partial W_{ij}(h_j)}{\partial \mathbf{r}_i} \right) \quad (1.10)$$

with f^{co} being a corrector factor given by

$$f_{i,j}^{co} = \left(1 + \frac{h_{i,j}}{3\rho_{i,j}} \frac{\partial \rho_{i,j}}{\partial h_{i,j}} \right)^{-1}. \quad (1.11)$$

The change of the energy of the system follows the equation

$$\frac{du_i}{dt} = f_i^{co} \frac{P_i}{\rho_i^2} \sum_j m_j (\mathbf{v}_i - \mathbf{v}_j) \cdot \frac{\partial W_{ij}(h_i)}{\partial \mathbf{r}_i} \quad (1.12)$$

in which we used the notation $W_{ij}(h_i) = W(x_{ij}, h_i)$. In the case of pure hydrodynamics (equation (1.10) the energy), momentum and angular momentum are exactly conserved. The SPH method solves these equations without any dissipation terms. Although, fluid flows often develop discontinuities, for example shocks. In this case an extra term is needed in order to describe correctly the fluid. This additional term in the velocity equation (1.10) has the form

$$\frac{d\mathbf{v}_i}{dt}|_{\text{visc}} = - \sum_j m_j \Pi_{ij} \frac{\partial \bar{W}_{ij}}{\partial \mathbf{r}_i} \quad (1.13)$$

where \bar{W}_{ij} is the arithmetic average of $W(x_{ij}, h_i)$ and $W(x_{ij}, h_j)$. This artificial viscosity causes changes in the entropy of the system that follows

$$\frac{dA_i}{dt} = \frac{1}{2} \frac{\gamma - 1}{\rho_i^{\gamma-1}} \sum_j m_j \Pi_{ij} \mathbf{v}_{ij} \cdot \frac{\partial \bar{W}_{ij}}{\partial \mathbf{r}_i} \quad (1.14)$$

with Π_{ij} the quantity which parametrizes the artificial viscosity. In GADGET it follows [Monaghan and Gingold, 1983] and [Balsara, 1995] and takes the form

$$\Pi_{ij} = \begin{cases} [-\alpha c_{ij} \mu_{ij} + \beta \mu_{ij}^2] / \rho_{ij} & \text{if } \mathbf{v}_{ij} \cdot \mathbf{r}_{ij} < 0 \\ 0 & \text{otherwise} \end{cases} \quad (1.15)$$

with

$$\mu_{ij} = \frac{h_{ij} \mathbf{v}_{ij} \cdot \mathbf{r}_{ij}}{|\mathbf{r}_{ij}|}. \quad (1.16)$$

In equation (1.15) and equation (1.16) the quantities μ_{ij} and ρ_{ij} are arithmetic means for the particles i and j of the mean molecular weight and density respectively, and c_{ij} is the sound speed. The parameters α and β are usually chosen to be $\alpha \simeq 0.5 - 1.0$, $\beta = 2\alpha$ and they regulate the strength of the viscosity. In the equation of motion the viscosity acts as an extra pressure term $P_{\text{visc}} \simeq \rho_{ij}^2 \Pi_{ij} / 2$.

So far the pure hydrodynamic case was examined. It is important though to consider full MHD treatment for problems in which the magnetic field is dynamically important. The MHD extension in GADGET was implemented by [Dolag and Stasyszyn, 2009]. When the magnetic field is included then the equation of motion changes and is written as

$$\begin{aligned} \frac{d\mathbf{v}_i}{dt} = & - \sum_j m_j \left(f_i^{\text{co}} \frac{P_i + B_i^2 / 2\mu_o}{\rho_i^2} \cdot \frac{\partial W_{ij}(h_i)}{\partial \mathbf{r}_i} + f_j^{\text{co}} \frac{P_j + B_j^2 / 2\mu_o}{\rho_j^2} \cdot \frac{\partial W_{ij}(h_j)}{\partial \mathbf{r}_i} \right) \\ & + \frac{1}{\mu_o} \sum_j \left(\frac{f_i^{\text{co}}}{\rho_i^2} B_i (B_i \cdot \frac{\partial W_{ij}(h_i)}{\partial \mathbf{r}_i}) + \frac{f_j^{\text{co}}}{\rho_j^2} B_j (B_j \cdot \frac{\partial W_{ij}(h_i)}{\partial \mathbf{r}_i}) \right). \end{aligned} \quad (1.17)$$

The presence of the magnetic field adds an extra pressure term in the equation of motion (second term of equation (1.17)) because we need to account for $\nabla \cdot \mathbf{B} = 0$. It is important to notice that in the MHD version of the Lagrangian

$$\mathcal{L}_{\text{MHD}} = \sum_i m_i \left(\frac{1}{2} v_i^2 - u_i - \frac{1}{2\mu_o} \frac{B_i^2}{\rho_i} \right) \quad (1.18)$$

the magnetic field and the change of the magnetic field cannot be written as function of particle coordinates. Thus, is not possible to use directly the Euler-Lagrange equations to derive the equation of motion equation (1.17). Instead, a more general variational principle is employed, which is given by

$$\delta\mathcal{L} = m_j \mathbf{v}_j \cdot \delta \mathbf{v}_j - \sum_i m_i \left(\frac{\partial u_i}{\partial \rho_i} \Big|_s \delta \rho_i + \frac{1}{2\mu_o} \left(\frac{B_i}{\rho_i} \right)^2 \delta \rho_i + \frac{1}{\mu_o} \mathbf{B}_i \cdot \left(\frac{\mathbf{B}_i}{\rho_i} \right) \right). \quad (1.19)$$

Now the variational principle is written with respect to an infinitesimal change in the spacial coordinate of the particle and we are able to express the change in the magnetic field as a function of the change in the particle coordinate. This is equivalent to a Lagrangian expression for the time derivative of the magnetic field. That means that not only the density calculation is needed for the equations of motion but also the evolution of the magnetic field. In ideal MHD the induction equation in Lagrangian form is given by

$$\frac{d}{dt} \left(\frac{\mathbf{B}}{\rho} \right) = \left(\frac{\mathbf{B} \cdot \nabla}{\rho} \right) \mathbf{v}. \quad (1.20)$$

The last equation in SPH formulation is written as

$$\frac{d}{dt} \left(\frac{\mathbf{B}_i}{\rho_i} \right) = \sum_j m_j (\mathbf{v}_i - \mathbf{v}_j) f_i^{\text{co}} \frac{\mathbf{B}_i}{\rho_i} \nabla W_{ij}(h_i) \quad (1.21)$$

A few tests of the MHD version of the code are presented in Chapter 3 and were extensively tested in [Dolag and Stasyszyn, 2009]. According to [Dolag and Stasyszyn, 2009] the use of regulation schemes are useful to suppress noise and $\text{div}(\mathbf{B})$ errors but need careful treatment so sharp features are not over-smoothed.

1.2.3 Additional Physics

In order to study structure formation problems it is essential to include various physical processes in a cosmological code. In GADGET, radiative cooling and heating is included as presented in [Katz et al., 1995] assuming collisional ionization equilibrium and optically thin gas. Star formation and feedback are following the work of [Springel and Hernquist, 2003] and are explained in detail in Chapter 2 as well. Other processes, such as thermal conduction [Dolag et al., 2004, Jubelgas et al., 2004] and growth of supermassive black holes as implemented by [Di Matteo et al., 2005] and [Springel et al., 2005], are included but not used in the simulations presented here.

Numerical galaxy formation and evolution is a complicated and multi-aspect problem. We prefer high resolution simulations in order to understand the physics that is crucial in the formation and evolution of the galaxy but also a realistic cosmological environment. The critical aspects of a galaxy simulation is to use realistic initial conditions, to include physical processes that are relevant and important in the galaxy formation and to choose the appropriate computational tools in order to produce results that can be compared with the

observations. In galaxies, apart from gravity, it is significant to employ a realistic model for the interstellar medium (ISM) that includes cooling and heating of the ISM, star formation, supernovae feedback, winds from massive stars, cosmic rays and magnetic fields but also the ubiquitous turbulence. Apart from the dynamical processes inside the galaxy, it is also essential to include the interaction of the galaxy with its circum-galactic medium. This involves inflowing gas but also outflows from the galaxy. The majority of the processes that are taking place in a galaxy are coupled, for example the presence of the magnetic field will alter the star formation in a galaxy and also the cosmic ray propagation. On the other hand, the stellar population will influence the magnetic field structure and through supernova explosions cosmic rays are affected as well. In simulations of cosmological boxes (figure 1.5) or even for simulations of isolated galaxies, star formation is a process that is taking place in scales far below the resolution limit. For this reason it is essential to build realistic sub-grid models in order to reproduce the unresolved physics. However, so far there has never been the attempt to adapt such sub-grid models for star formation in order to include additional physics, for example magnetic fields, which summarizes the motivation for this thesis. In the next chapter we will explain the star formation model that the cosmological code GADGET applies and then an extension which allows the coupling of the magnetic field with the star formation in a galaxy. In the last chapter we present simulations that were performed with the extension of the sub-grid model for star formation.

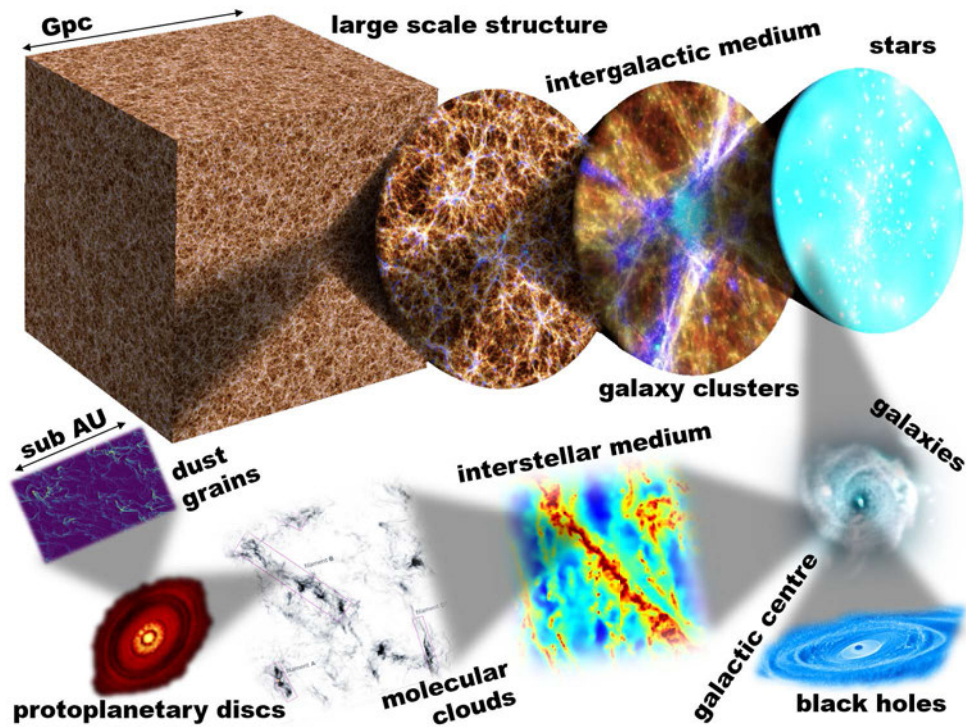


Figure 1.5: Visual representation of different components of cosmological simulations. The common paradigm for cosmological simulations is to occupy a large box which includes large scale structures such as galaxy and galaxy clusters. It is important to model the physics for the intergalactic medium, then in lower scales the galaxies and the interstellar medium. Many physical processes are happening in small scales, for example star and planet formation, but is not possible to resolve them in the cosmological simulations. Therefore, we build realistic sub-grid models in order to mimic the unresolved physics. Taken from: <http://www.usm.uni-muenchen.de/Masterarbeiten.php>

Chapter 2

Star Formation models

2.1 Star Formation model in gadget

The cosmological code GADGET uses the sub-grid, multiphase model for star formation as proposed by [Springel and Hernquist, 2003]. According to this model, the gas in the interstellar medium (ISM) consists of hot and cold gas, which interacts with processes such as radiative cooling, supernova (SN) feedback in the form of thermal heating and cloud evaporation, metal enrichment and star formation. From simulations is shown that this model predicts a self-regulated, quiescent mode of star formation which stabilizes the star formation in the gaseous part of the disk of the galaxies. The only free parameter of this model, as will be shown later, is the overall timescale of star formation, which is tuned using the observational Schmidt-Kennicutt relation, given by [Kennicutt Jr, 1998, Schmidt, 1959]. The model has an extension that includes the generation of galactic winds, however we do not use this option in this work.

2.1.1 The sub-grid model

This hybrid model is an attempt to describe the ISM by using the global dynamics and spatially averaged properties of the medium and not to resolve the multiphase structure of the ISM in small structures. They consider that one resolution element of the code - a SPH particle in the current case - consists of hot and cold gas. The SPH fluid element represents a region of the ISM and it is considered that there are cold clouds in pressure equilibrium with the ambient hot gas. In the following, ρ_h is the density of the hot gas, ρ_c is the density of the cold gas, the total gas density is written as $\rho = \rho_h + \rho_c$ and ρ_* is the density of the stars that are formed. The thermal energy per unit volume is written as $\epsilon = \rho_h u_h + \rho_c u_c$, with u_h, u_c is the specific hot and cold energy respectively.

The star formation occurs in the cores of molecular clouds - that are not actually resolved in the simulation - and for this model the star formation is the process that converts a part of the cold gas of the ISM into stars at a characteristic timescale t_* . The time derivative of the density of the stars is written as

$$\frac{d\rho_*}{dt} = \frac{\rho_c}{t_*} - \beta \frac{\rho_c}{t_*} = (1 - \beta) \frac{\rho_c}{t_*}. \quad (2.1)$$

The parameter β is the fraction of the massive stars ($> 8M_\odot$) that explode as supernovae and is set to $\beta = 0.1$. This comes from a Salpeter Initial Mass Function (IMF) [Salpeter, 1955] with slope of -1.35. This fraction is subtracted from the gas that forms stars because the timescale of supernovae explosions, which is the typical lifetime of a massive star, is negligible comparing the timescale of the star formation in the quiescent mode.

The supernova feedback has two different effects on the ISM, i.e., heating of the ISM and cold cloud evaporation. The blast wave of the supernova heats the surrounding gas through the shocks that are created but also can destroy the cold and dense clouds that are located near the explosion mainly by thermal conduction. As far as the heating is concerned, one supernova releases 10^{51} erg, which corresponds to $\epsilon_{\text{SN}} = 4 \cdot 10^{48} \text{ erg} \cdot M_\odot^{-1}$ for the adopted IMF. Therefore, the heating rate of the ISM from the SN is written as

$$\frac{d\rho_h u_h}{dt} = \epsilon_{\text{SN}} \frac{d\rho_*}{dt} = \beta u_{\text{SN}} \frac{\rho_c}{t_*} \quad (2.2)$$

where $u_{\text{SN}} = (1 - \beta)\beta^{-1}\epsilon_{\text{SN}}$. Apart from the heating of the hot phase of ISM, the supernova explosion destroys the cold clouds that are located near to them and thus material from the cold phase is transferred in the hot phase. This process is expressed by

$$\left. \frac{d\rho_c}{dt} \right|_{\text{EV}} = A\beta \frac{\rho_c}{t_*} \quad (2.3)$$

A is the efficiency of the evaporation process and depends on the density as $A \propto \rho^{-4/5}$ [McKee and Ostriker, 1977].

The last process that describes the mass flow between the hot and the cold phase is the radiative cooling. Assuming a thermal instability operating, a part of the hot ambient medium cools and gives rise to the cold clouds. This process is described by the following equation

$$\left. \frac{d\rho_c}{dt} \right|_{\text{TI}} = - \left. \frac{d\rho_h}{dt} \right|_{\text{TI}} = \frac{1}{u_h - u_c} \Lambda_{\text{net}}(\rho_h, u_h). \quad (2.4)$$

The cooling function that GADGET uses is described by [Katz et al., 1995] and contains radiative processes appropriate for primordial plasma of hydrogen and helium.

In this formulation, the internal structure of the cold clouds is neglected and it is assumed that the gas cannot cool below $10^3 - 10^4$ K. Thus, the temperature of the cold clouds is set to be constant at $T = 10^3$ K and the temperature and internal energy of the total gas is essentially the temperature and internal energy of the hot ambient medium. Using equation (2.1) to equation (2.4), the evolution of the masses of the hot and cold gas is written as follows

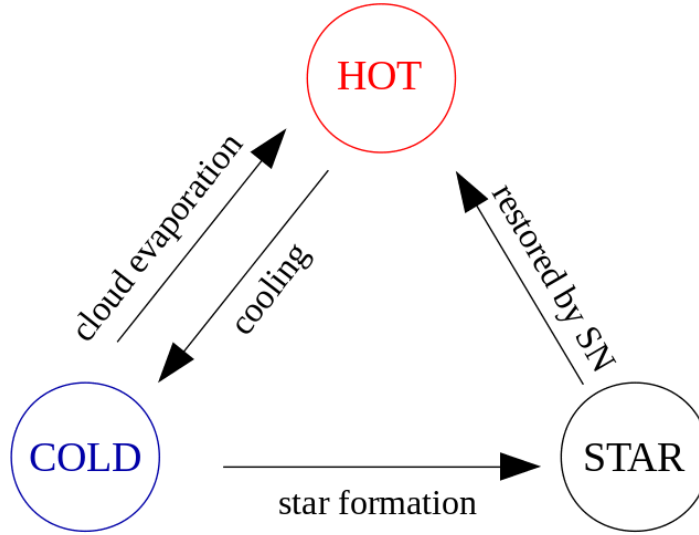


Figure 2.1: Mass flow and description of the processes taking place between the different phases of the gas.

$$\frac{d\rho_c}{dt} = -\frac{\rho_c}{t_*} - A\beta\frac{\rho_c}{t_*} + \frac{1-f}{u_h - u_c}\Lambda_{\text{net}}(\rho_h, u_h) \quad (2.5)$$

$$\frac{d\rho_h}{dt} = \beta\frac{\rho_c}{t_*} + A\beta\frac{\rho_c}{t_*} - \frac{1-f}{u_h - u_c}\Lambda_{\text{net}}(\rho_h, u_h) \quad (2.6)$$

The factor f denotes the operation of the thermal instability and can take two values, 1 and 0. If $f = 0$ then the thermal instability is operating and if $f = 1$ then normal cooling is taking place. For the onset of thermal instability and thus star formation, a density criterion should be fulfilled, namely $\rho > \rho_{\text{thr}}$. This means that the star formation occurs only when cold clouds are formed and the density exceeds the density threshold ρ_{thr} . In the equation (2.5) and the equation (2.6) the first term on the right side accounts for the star formation, the second for the cloud evaporation and the last one for the growth of cold clouds through radiative cooling. The energy balance of the ISM including the aforementioned processes is shown in the following equation

$$\frac{d(\rho_h u_h + \rho_c u_c)}{dt} = -\Lambda_{\text{net}}(\rho_h u_h) + \beta\frac{\rho_c}{t_*}u_{\text{SN}} - (1-\beta)\frac{\rho_c}{t_*}u_c. \quad (2.7)$$

In the equation (2.7) the left-hand side describes the energy rate per unit volume and in the right-hand side the first term is the radiative cooling of the hot ambient medium, the second term is the heating from supernovae explosions and the third term is the energy loss by star formation. Considering that the multiphase structure of the ISM, the equation (2.7) can be split into two components, i.e., the hot and cold components

$$\frac{d(\rho_h u_h)}{dt} = -\frac{\rho_c}{t_*} u_c - A\beta \frac{\rho_c}{t_*} u_c + \frac{(1-f)u_c}{u_h - u_c} \Lambda_{\text{net}} \quad (2.8)$$

$$\frac{d(\rho_c u_c)}{dt} = \beta \frac{\rho_c}{t_*} (u_{\text{SN}} + u_c) + A\beta \frac{\rho_c}{t_*} u_c + \frac{u_h - f u_c}{u_h - u_c} \Lambda_{\text{net}}. \quad (2.9)$$

In both equations the first term of the right-hand side corresponds to the star formation and feedback, the second term to the cold cloud evaporation and the last term corresponds to the effect of the thermal instability.

As was mentioned above, the temperature of the cold clouds is constant and thus u_c is constant as well. In the code the evolution of the hot phase is tracked, therefore, equation (2.7), using equation (2.6) is written as

$$\rho_h \frac{du_h}{dt} = \frac{\rho_c}{t_*} (u_{\text{SN}} + u_c - u_h) - A\beta \frac{\rho_c}{t_*} (u_h - u_c) - f \Lambda_{\text{net}}. \quad (2.10)$$

Considering active star formation, i.e., thermal instability operating ($f = 0$), the equation (2.10) has an equilibrium solution. To be more specific, for $f = 0$ the solution of the differential equation (2.10) is

$$u_h(t) = \exp\left(-\frac{\beta}{t_*} \frac{\rho_c}{\rho_h} (A+1) \cdot t\right) + \frac{u_{\text{SN}}}{A+1} + u_c. \quad (2.11)$$

For timescales $\tau_h = \frac{t_* \rho_h}{\beta(1+A)\rho_c} \gg t$ the above solution reaches an equilibrium solution

$$u_h = \frac{u_{\text{SN}}}{1+A} + u_c. \quad (2.12)$$

Assuming that the star formation is quicker than the heating and cooling, the hot phase will remain in temperature given by equation (2.12). Keeping this into consideration, a self-regulated cycle of star formation is set. Cloud evaporation and star formation reduces the density of the cold phase, which lowers the star formation rate. At the same time, the high density of the hot phase increases the cooling rate which translates into further growth of the cold clouds and increase of the star formation rate. Within this equilibrium phase, the multiphase structure of the ISM is treated as an effective medium with a constant effective pressure

$$P_{\text{eff}} = (\gamma - 1)(\rho_h u_h + \rho_c u_c). \quad (2.13)$$

The effective pressure is constant, hence from equation (2.7) we have

$$\frac{\rho_c}{t_*} = \frac{\Lambda_{\text{net}}(\rho_h, u_h)}{\beta u_{\text{SN}} - (1-\beta)u_c}. \quad (2.14)$$

Using $\Lambda_{\text{net}}(\rho_h, u_h) = (\rho_h/\rho)^2 \Lambda_{\text{net}}(\rho, u_h)$, the ratio of the density of the cold gas over the density of the hot gas is

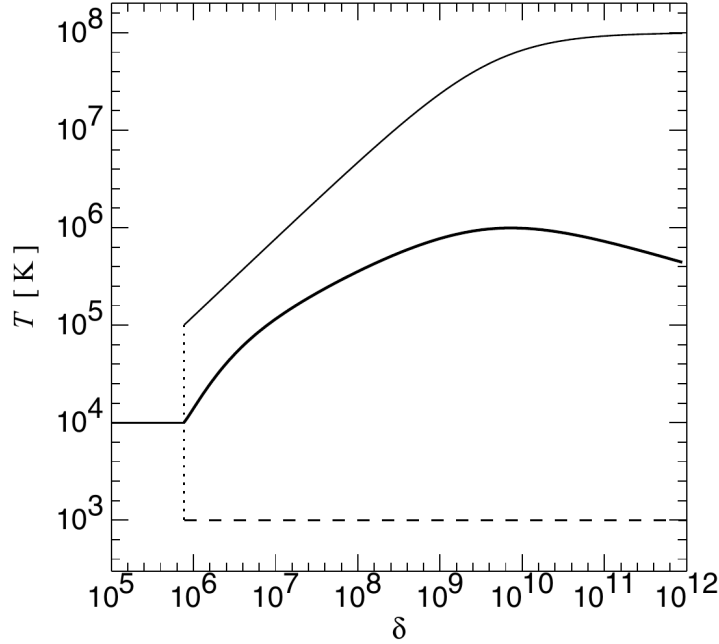


Figure 2.2: Temperature of the gas plotted against the baryonic overdensity. The temperature has 3 components, i.e., the upper thin line corresponds to the temperature of the hot phase of the gas, the middle to the effective gas and the lower dashed line to the cold clouds. From [Springel and Hernquist, 2003].

$$\frac{\rho_c}{\rho_h} = \frac{\rho_h}{\rho} y \quad (2.15)$$

with y

$$y = \frac{t_* \Lambda_{\text{net}}(\rho, u_h)}{\rho[\beta u_{\text{SN}} - (1 - \beta)u_c]}. \quad (2.16)$$

Assuming that the parameters t_* and A depend only on density, the fraction $x = \rho_c/\rho$ of the cold gas depends only on the gas density and is expressed in terms of y as

$$x = 1 + \frac{1}{2y} - \sqrt{\frac{1}{y} + \frac{1}{4y^2}}. \quad (2.17)$$

The dependence of the fraction of the cold clouds on the density is shown in figure 2.3. Using the quantity x the effective pressure is now written as

$$P_{\text{eff}} = (\gamma - 1)\rho[(1 - x)u_h + xu_c]. \quad (2.18)$$

The effective temperature of the medium that corresponds to the pressure of equation (2.18) is shown in figure 2.2 as a function of density. In the same figure is plotted the constant temperature of the cold clouds (dashed lines) and the temperature of the hot phase (upper solid line) of the ISM.

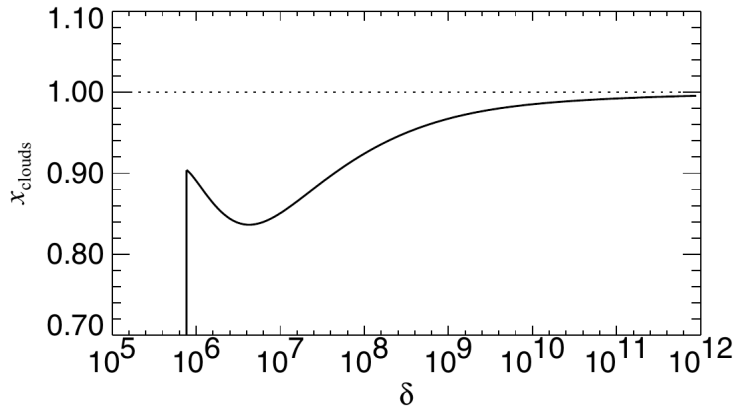


Figure 2.3: Fraction of cold clouds as a function of the baryonic overdensity. From [Springel and Hernquist, 2003].

2.1.2 Selection of parameters

As mentioned above, the parameters A and t_* depend on the density. According to the theoretical approach of [McKee and Ostriker, 1977] the SN evaporation parameter A can be parametrized as

$$A(\rho) = A_0 \left(\frac{\rho}{\rho_{\text{thr}}} \right)^{-4/5}. \quad (2.19)$$

As far as the timescale for star formation is concerned, we correlate it with the local dynamical time of the gas, so

$$t_*(\rho) = t_0^* \left(\frac{\rho}{\rho_{\text{thr}}} \right)^{-1/2}. \quad (2.20)$$

Therefore, the free parameters of the model so far, which moderate the ISM, are the normalization parameter A_0 , the t_0^* and the density threshold ρ_{thr} . In order to constrain the A_0 , one has to think the onset of the thermal instability. From the equilibrium solution equation (2.12) the temperature of the hot phase is approximately 10^5 K. At this temperature the thermal instability operates and the cooling function starts to fall. Thus $T_{\text{SN}}/A_0 = 10^5$ K, which constrains the parameter A_0 to be $A_0 = 1000$, for a typical supernova "temperature" of $T_{\text{SN}} = 2\mu u_{\text{SN}} m_H / 3k = 10^8$ K.

To continue, using equation (2.15) together with equation (2.16) and the fact that $\rho = \rho_h + \rho_c$ we have

$$\begin{aligned}
y &= \frac{t_* \Lambda_{\text{net}}(\rho, u_h)}{\rho[\beta u_{\text{SN}} - (1 - \beta)u_c]} \Rightarrow \\
\frac{\rho_c \rho}{\rho_h^2} &= \frac{t_* \Lambda_{\text{net}}(\rho, u_h)}{\rho[\beta u_{\text{SN}} - (1 - \beta)u_c]} \Rightarrow \\
\frac{\rho_c \rho}{(\rho - \rho_c)^2} &= \frac{t_* \Lambda(\rho, u) \rho^2}{\rho[\beta u_{\text{SN}} - (1 - \beta)u_c]} \Rightarrow \\
\frac{\rho_c}{\rho} \cdot \frac{1}{(1 - \rho/\rho_c)^2} &= \frac{t_* \Lambda(\rho, u) \rho}{\rho[\beta u_{\text{SN}} - (1 - \beta)u_c]}.
\end{aligned}$$

Where the cooling function Λ is defined as $\Lambda(\rho, u) = \Lambda_{\text{net}}(\rho, u)/\rho^2$. Using the definition of the cold fraction $x = \rho_c/\rho$, the expression of the density at the threshold is written as

$$\rho_{\text{thr}} = \frac{x_{\text{thr}}}{(1 - x_{\text{thr}})^2} \frac{\beta u_{\text{SN}} - (1 - \beta)u_c}{t_0^* \Lambda(u_{\text{SN}}/A_0)} \quad (2.21)$$

where x_{thr} is the cold fraction in the threshold and is calculated as $x_{\text{thr}} = 1 + (A_0 + 1)(u_c - u_4)/u_{\text{SN}} \simeq 1 - A_0 u_4/u_{\text{SN}}$. The last expression comes from the condition of the effective pressure being a continuous function of the density at the onset of self-regulated star formation. The gas below the density threshold cools down to 10^4 K and is neutral. Further cooling would require molecular cooling which is neglected in this model. Thus, the condition is translated into $u_{\text{eff}}(\rho_{\text{thr}}) = u_4$, with u_4 being the specific energy that corresponds to a temperature of 10^4 K.

The last parameter that needs to be constrained is the overall timescale for star formation t_0^* which sets the overall gas consumption timescale in the galaxy. This parameter is correlated to the efficiency of the star formation and will be constrained by the observations. It has been observed that the star formation rate per unit area is strongly correlated to the surface density of gas in galactic disks. This is known as the Schmidt-Kennicutt from [Schmidt, 1959, Kennicutt Jr, 1998] and is given by the following equation

$$\Sigma_{\text{SFR}} = (2.5 \pm 0.7) \cdot 10^{-4} \left(\frac{\Sigma_{\text{gas}}}{\text{M}_{\odot} \text{pc}^{-2}} \right)^{1.4 \pm 0.15} \frac{\text{M}_{\odot}}{\text{yr} \cdot \text{kpc}^2}. \quad (2.22)$$

This relation holds for more than 4 orders of magnitudes in disk-averaged gas densities in galaxies and shows a clear threshold in the star formation. As shown in the solid line of the figure 2.4 the star formation rate per disk area is going quickly to zero for disk densities lower than $\sim 9 \text{ M}_{\odot} \text{pc}^{-2}$. It is important that simulations of galaxies will reproduce this correlation, as is a test to prove the correct behaviour of the star formation. In figure 2.4 the observational Schmidt-Kennicutt relation (dashed inclined line, equation (2.22)) is plotted and different predictions of the model (dotted lines) by changing the parameter of the overall star formation t_0^* . It is obvious that the model under discussion is very sensitive in the change of the parameter t_0^* . The best fit corresponds to $t_0^* = 2.1 \text{ Gyr}$, displayed by the solid inclined line in figure 2.4.

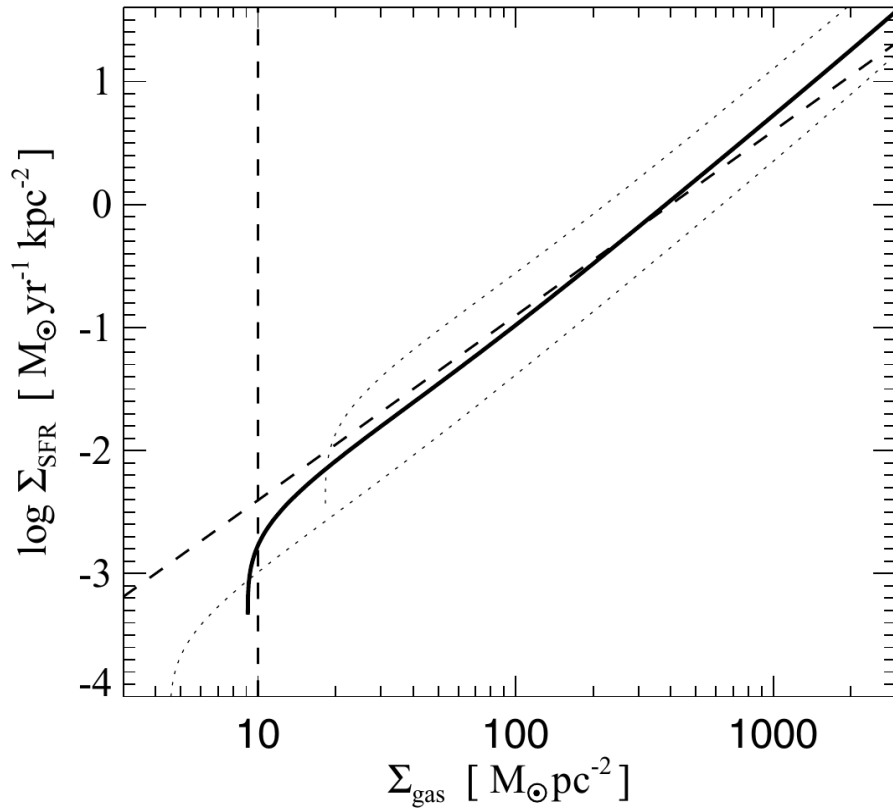


Figure 2.4: The star formation rate per unit area as a function of the gas density of the galaxy. The dashed inclined line shows the observational Schmidt-Kennicutt relation while the vertical dashed line indicates the observational cut-off. The upper dotted line is the prediction of the model for $t_0^* = 0.53$ Gyr, the lower for $t_0^* = 8.4$ Gyr and the solid line is the best fit for $t_0^* = 2.1$ Gyr. Plot taken from [Springel and Hernquist, 2003]

2.1.3 Code implementation

According to the equations presented in the previous section, the hot phase of the ISM will evolve towards an equilibrium solution and its temperature is given by equation (2.12). The timescale of this process is smaller than the timescale of the star formation which means that the self regulation regime is reached quickly and we can use the set of equation (2.12)-equation (2.18) to describe the gas of the ISM in the code. The star formation rate is calculated as

$$\dot{M}_* = (1 - \beta) \frac{x \cdot m}{t_*} \quad (2.23)$$

where $x \cdot m$ is the mass of the cold clouds and t_* is calculated from equation (2.20). For each time-step a new star is formed in a stochastic way, i.e., when a random number drawn uniformly from the interval $[0,1]$ is bellow

$$p_* = \frac{m}{m_*} \left[1 - \exp \left(- \frac{(1 - \beta)x\Delta t}{t_*} \right) \right] \quad (2.24)$$

$m_* = m_0/N_g$ is the mass of the star, m_0 is the initial mass of the particle and N_g is the number of generations of stars that each SPH particle can generate. In our case the number of generations is chosen to be $N_g = 1$. This means that each gas particle can generate 1 star particle, which will have the same mass as the gas particle and will be initiated with the same space variables. When the star is spawned will be decoupled from the sub-grid model and will become one collisionless particle. With this simple way of generating stars we avoid to have hybrid gas-stars particles because all the stellar mass is contained by the stellar particle. Also the mass resolution remains constant for all particles.

2.2 An alternative formulation of the model

The aforementioned model predicts a self-regulated star formation model for cosmological simulations of galaxy formation. It is based on rough approximations but is also physically motivated from the basic processes that take place in the ISM. However, it doesn't take into account the non-thermal processes of the ISM, such as cosmic rays and magnetic fields. A straightforward way to include further processes is to transform the density threshold of the model into a pressure threshold or to include the hydrostatic pressure of the ISM in the formula such that affects the threshold of star formation. Therefore, we can add the different components of pressure beyond the thermal pressure and take into consideration further processes that can be dynamically important for the ISM. This is important because the magnetic fields, turbulent motion of gas and the cosmic rays are dynamically important components of the ISM as was already shown in figure 1.1. In this section we will present an alternative way to consider the sub-grid model of star formation following the formulation of [Murante et al., 2010].

2.2.1 Model equations

Following the idea of the multiphase structure of the ISM, the gas can be in the cold or the hot phase. Based on the description presented in [Murante et al., 2010], the two phases are in pressure equilibrium

$$n_h T_h = n_c T_c \quad (2.25)$$

with $n_{h,c}$ being the number density and $T_{h,c}$ the temperature of each phase. The corresponding number densities are computed as

$$n_{h,c} = \rho_{h,c} / (\mu_{h,c} m_p), \quad (2.26)$$

with m_p being the proton mass and $\mu_{h,c}$ the mean molecular weight of the hot and cold phase respectively. We assume that the fraction of neutral hydrogen is $f_{\text{HI}} = 0.76$ and thus the mean molecular weights are $\mu_h = 4/(5f_{\text{HI}} + 3) = 0.6$ for the hot phase and $\mu_c = 4/(3f_{\text{HI}} + 3) = 1.2$ for the cold phase. The temperature of the cold phase is set to $T_c = 10^3$ K and is constant in accordance to the star formation model by [Springel and Hernquist, 2003] (from here on referred as SH03). The physical densities are averaged quantities over the volume and are written as

$$\rho_h = \frac{M_h}{f_h V} \quad (2.27)$$

$$\rho_c = \frac{M_c}{f_c V} \quad (2.28)$$

$f_{h,c}$ is the filling factor for the different gas phases and V the total volume of the resolution element, which is the SPH particle in this work. Using the pressure equilibrium condition from equation (2.25) and equation (2.27)-equation (2.28) we have

$$\begin{aligned} \frac{\rho_h}{\mu_h m_p} T_h &= \frac{\rho_c}{\mu_c m_p} T_c \Rightarrow \\ \frac{M_h T_h}{f_h V \mu_h} &= \frac{M_c T_c}{f_c V \mu_c} \Rightarrow \\ f_h &= M_h \frac{T_h}{T_c} \frac{\mu_c}{\mu_h} f_c. \end{aligned}$$

The filling factors should hold the relation $f_c + f_h = 1$. Moreover, we define the mass fraction of the hot phase as

$$F_h = \frac{M_h}{M_h + M_c}. \quad (2.29)$$

From the equation (2.29) follows: $M_h = F_h / (1 - F_h)$ and it is trivial that $F_c + F_h = 1$. Thus, the filling factor of the hot phase is expressed by

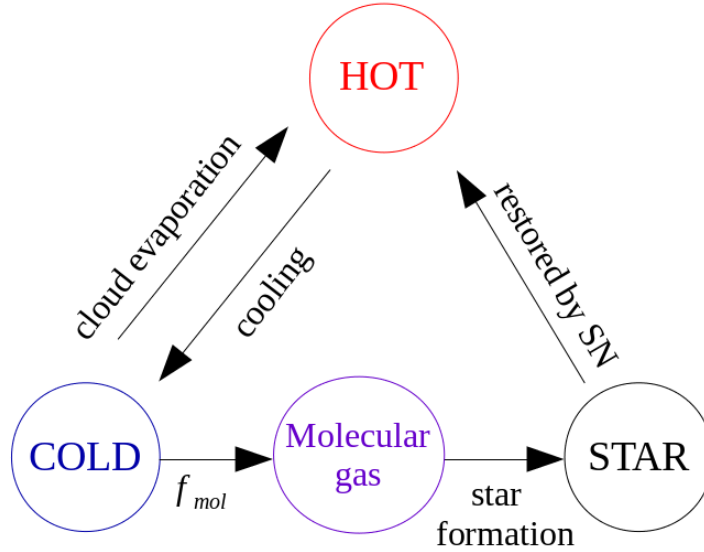


Figure 2.5: Mass flow and physical processes between the different phases of the interstellar medium.

$$f_h = \frac{1}{1 + (F_c/F_h)(\mu_h/\mu_c)(T_c/T_h)}. \quad (2.30)$$

Mass is exchanged by the different components of the gas with processes as in SH03 model. In details, the hot gas cools into cold through radiative cooling and when the pressure is high enough a fraction of the cold gas turns into molecular gas, from which the stars are formed. When enough stars are formed then they become an individual collisionless particle which does not interact with the gas hydrodynamically. Some of the stars are very massive and thus explode as supernova. Part of the energy released in the supernova explosions heats up the gas and restores the hot phase of the medium. Moreover, the supernova explosion has an important effect in its surrounding medium as it destroys the cold clouds that are located near to the explosion. These processes are shown in figure 2.5. The crucial point in this description is the connection of the molecular fraction of the gas to the pressure. It has been observationally proven that a tight correlation exists between the external pressure of the ambient medium of the galaxy to the H_2 gas by [Blitz and Rosolowsky, 2006], namely

$$f_{\text{mol}} = \frac{1}{1 + P_0/P} \quad (2.31)$$

with $P_0/k_B = 35000 \text{ Kcm}^{-3}$ and k_B the Boltzmann constant. In [Blitz and Rosolowsky, 2006] they use the pressure calculated from global gas and star properties and it corresponds in the hydrostatic pressure. For this reason the thermal gas pressure and magnetic pressure should be taken into account. As has already been mentioned, the stars are formed from the molecular fraction of the cold gas. This is happening in a characteristic timescale,

which it is chosen to be the dynamical time of the cold gas

$$t_{\text{dyn}} = \sqrt{\frac{3\pi}{32G\rho_c}} = 5.15 \cdot 10^7 (\mu_c n_c)^{-1/2} \text{ yr} \quad (2.32)$$

with n_c the number density of the cold gas in cgs. Including a star formation efficiency parameter of $f_* = 0.02$ the star formation rate will be

$$\dot{M}_{\text{sfr}} = f_* \frac{f_{\text{mol}} M_c}{t_{\text{dyn}}}. \quad (2.33)$$

A part of the stars that are formed are massive and restore the hot phase in the form of heating from supernova feedback, hence

$$\dot{M}_{\text{SN}} = f_{\text{SN}} \dot{M}_{\text{sfr}} \quad (2.34)$$

with the parameter f_{SN} set to be $f_{\text{SN}} = 0.2$ according to a Salpeter stellar initial mass function (IMF). To continue, the hot gas cools through radiative cooling. In this description we neglect metal production, thus this process is defined as

$$\dot{M}_{\text{cool}} = \frac{M_h}{t_{\text{cool}}} \quad (2.35)$$

where the cooling timescale t_{cool} to be derived from the cooling function implemented in GADGET code that uses the tabulated cooling rates from [Katz et al., 1995]. In contrast to the SH03 model, the evaporation of the cold clouds is not due to thermal conduction but rather due to simple destruction of the molecular cloud from the supernova feedback. According to [Monaco, 2004] for a supernova event, 10% of the cold clouds are destroyed. Therefore, the evaporation processes is defined as

$$\dot{M}_{\text{ev}} = f_{\text{ev}} \dot{M}_{\text{sfr}} \quad (2.36)$$

with $f_{\text{ev}} = 0.1$.

Taking into consideration the figure 2.5 and equation (2.33) - equation (2.36) the differential equations that describe the mass flows in our model are

$$\dot{M}_* = \dot{M}_{\text{sfr}} - \dot{M}_{\text{SN}} \quad (2.37)$$

$$\dot{M}_c = \dot{M}_{\text{cool}} - \dot{M}_{\text{sfr}} - \dot{M}_{\text{ev}} \quad (2.38)$$

$$\dot{M}_h = -\dot{M}_{\text{cool}} + \dot{M}_{\text{SN}} + \dot{M}_{\text{ev}}. \quad (2.39)$$

Using the expressions for each term, the last set of equations is re-written as

$$\dot{M}_* = (1 - f_{\text{SN}}) \dot{M}_{\text{sfr}} \quad (2.40)$$

$$\dot{M}_c = \frac{M_h}{t_{\text{cool}}} - (1 + f_{\text{ev}}) \dot{M}_{\text{sfr}} \quad (2.41)$$

$$\dot{M}_h = -\frac{M_h}{t_{\text{cool}}} + (f_{\text{SN}} + f_{\text{ev}}) \dot{M}_{\text{sfr}}. \quad (2.42)$$

In contrast to [Murante et al., 2010] who solved the set of differential equations for each timestep we want to obtain an equilibrium solution for the above system of equations. In fact, the solution of the differential equation equation (2.42) is

$$M_h = C \cdot e^{-t/t_{\text{cool}}} + (f_{\text{SN}} + f_{\text{ev}}) \frac{t}{t_{\text{dyn}}} f_* f_{\text{mol}} M_c \quad (2.43)$$

with C being a normalization constant. In this solution, opposite to the equilibrium solution of [Springel and Hernquist, 2003], the mass of the hot phase depends on the mass of the cold phase that is not constant, but is the solution of the differential equation equation (2.41). Since the mass of every component of the particle depends on the evolution of a different component we should investigate if there is an equilibrium solution of the system of equations. First we examine the case of equilibrium solution between the hot and cold gas. To be more specific, to find an equilibrium solution similar to the approach of [Springel and Hernquist, 2003]. To do so, the determinant of the system of the equations should be zero for non trivial solution. To simplify the equations we write them as

$$\dot{x} = -\alpha x + \beta y \quad (2.44)$$

$$\dot{y} = \alpha x - \gamma y \quad (2.45)$$

where $x = M_h$, $y = M_y$ and \dot{x}, \dot{y} their time derivatives respectively. The constants $\alpha = 1/t_{\text{cool}}$, $\beta = (f_{\text{SN}} + f_{\text{ev}}) f_* f_{\text{mol}} / t_{\text{dyn}}$ and $\gamma = (1 + f_{\text{ev}}) f_* f_{\text{mol}} / t_{\text{dyn}}$. The determinant of this system is

$$\det \begin{vmatrix} -\alpha & \beta \\ \alpha & -\gamma \end{vmatrix} \quad (2.46)$$

The determinant is zero only for $\gamma = \beta$ which is obviously not the case. If the system had solution then together with the condition $M_{\text{gas}} = M_h + M_c$ we could determine the M_h, M_c as a function of known quantities. The next step is to think if we could find a solution of the system of the 3 equations that describe the mass flow between different components of the ISM (equation (2.40)-equation (2.42)). In a simplified form are written as

$$\dot{x} = -\alpha x + \beta y \quad (2.47)$$

$$\dot{y} = \alpha x - \gamma y \quad (2.48)$$

$$\dot{z} = \delta y \quad (2.49)$$

with $\dot{z} = M_*$ and $\delta = f_* f_{\text{mol}} / t_{\text{dyn}}$. The determinant of this system is calculated as

$$\det \begin{vmatrix} -\alpha & \beta & 0 \\ \alpha & -\gamma & 0 \\ 0 & \delta & 0 \end{vmatrix} \quad (2.50)$$

The determinant is zero and thus the system of differential equations has a non trivial solution which is calculated by finding the eigenvectors of the system. However, we still need 2 more constrains of the masses M_*, M_h and M_c . In this formulation we don't have

these constraints and consequently is not possible to implement a solution in an equilibrium form, in which for each time step the masses of the cold and hot gas were calculated in the framework of a self-regulated equilibrium state. We therefore conclude that these equations should be solved for each timestep and obtain the desired quantities each timestep accounting for the evolution of different components of the SPH particle. This is done by [Murante et al., 2010] and the subresolution model that they implemented in GADGET is called MUPPI. For each particle they impose a density and temperature threshold in order to enter the multiphase model. The density of the particle should be greater than a density threshold $n > n_{\text{thr}} = 0.01 \text{ cm}^{-3}$ and temperature below $T < T_{\text{thr}} = 5 \cdot 10^4 \text{ K}$. The density threshold is relatively low such that most of the particles enter the multiphase regime. Even though stars are not formed in temperatures in the order of the temperature threshold, the threshold is imposed to prevent particles with high density and high temperature to enter the star forming regime. When a particle enters this regime all its mass is assigned to be in the hot phase. Then the hot phase cools and a fraction of cold clouds arise. If the pressure is high enough then molecular clouds are formed which initiate the star formation. From the stars that are formed, a couple of them are exploded as supernova and restore the hot phase of the gas and destroy a part of the cold clouds. For this model the same timescale regulates both the star formation and the time that the particle stays in the multiphase regime. The last timescale is set to be $2 \cdot t_{\text{dyn}}$ which corresponds to the characteristic timescale that the molecular cloud which produce stars is destroyed. The particle can also exit the multiphase regime when its density is lower than $n_{\text{out}} < 2n_{\text{thr}}/3$. When the particle exits this regime the supernova energy is distributed among its neighbours. The model reproduces the Schmidt-Kennicutt relation and the basic properties of the ISM in disk galaxies. An interesting extension would be to perform magneto-hydrodynamic (MHD) simulations with this model and examine the differences with the pure hydrodynamic case. Moreover, instead of using the observational relation by [Blitz and Rosolowsky, 2006] for the molecular fraction, it would be interesting to follow the creation of molecular clouds in a more detailed and physically motivated way. However this would require higher resolution simulations since now we do not resolve molecular clouds. Last but not least, the timescale for star formation could be also related to other time-scales, such as the turbulent crossing time of a molecular cloud. This is useful if the star formation is regulated by turbulent motions. The contribution of turbulent motions in the cold gas is neglected in the MUPPI but the simple model that accounts only for the thermal energy of the cold gas is still an adequate approximation.

2.3 Pressure based star formation model

In the previous section we concluded that the alternative formulation of the star formation model as presented by [Murante et al., 2010] cannot be implemented in the form of an equilibrium solution. The idea however remains the same, we want couple the magnetic field in the sub-grib model for star formation. An efficient way to do that is to include the observational relation between the molecular fraction of the gas with the hydrostatic pressure of the galaxy from [Blitz and Rosolowsky, 2006], as it has been already done by [Murante et al., 2010]. In the following we will explain how this idea alters and extends the model of [Springel and Hernquist, 2003].

2.3.1 Equations of the multiphase model

In this model we are following the idea of multiphase structure of the interstellar medium. One gas particle consists of hot and cold gas and when the pressure is high enough a part of the cold gas turns into molecular gas from which the stars are formed. The processes that we include in this multiphase model are similar to the aforementioned models and are described by the mass flow diagram in figure 2.5. The stars are formed in a characteristic timescale that we choose to be the free fall timescale of the cold gas. The star formation is described by the following equation

$$\frac{d\rho_*}{dt} = (1 - \beta)f_*f_{\text{mol}}\frac{\rho_c}{t_{\text{dyn}}} \quad (2.51)$$

with β being the fraction of stars that instantly die as supernova and do not contribute to the star formation. The parameter β depends on the initial mass function (IMF) and we choose $\beta = 0.1$ for a Salpeter IMF [Salpeter, 1955] as in [Springel and Hernquist, 2003]. The star formation is proportional to the mass of the molecular clouds and it has an efficiency of f_* . This is associated to the stars that are formed given the gas reservoir of the galaxy which are correlated through the observational Schmidt-Kennicutt relation (equation (2.22), [Schmidt, 1959, Kennicutt Jr, 1998]). The overall time scale of the star formation we assume that happens in the dynamical time of the cold gas

$$t_{\text{dyn}} = \sqrt{\frac{3\pi}{32G\rho_c}}. \quad (2.52)$$

The molecular fraction of the gas is calculated given the observational relation found in the study of [Blitz and Rosolowsky, 2006]. The molecular fraction is proportional to the hydrostatic pressure of the galaxy and is given by

$$f_{\text{mol}} = \frac{1}{1 + P_0/P} \quad (2.53)$$

with $P_0/k_B = 35000 \text{ Kcm}^{-3}$ which expresses the external pressure of the ISM when the half of the gas is in molecular form. The external pressure is calculated from the midplane

pressure of an infinite disk that consists of gas and stars under the assumption that the gas scale height is much lower than the stellar scale height. The pressure according to [Blitz and Rosolowsky, 2006] is given from the following expression

$$P_{\text{ext}} = (2G)^{0.5} \Sigma_g u_g \left[\rho_*^{0.5} + \left(\frac{\pi}{4} \rho_g \right) \right]. \quad (2.54)$$

In the last equation Σ_g is the surface density of the gas, u_g is the vertical velocity dispersion of the gas, ρ_* is the midplane density of the stellar population and ρ_g the midplane density of the gas. This pressure corresponds to the hydrostatic pressure of the galaxy and includes the thermal pressure but also non thermal components. For the simulations we approximate this pressure with the SPH pressure of the particle plus the magnetic pressure.

From the stars that are formed many of them explode as supernova. This heats the surrounding medium in the form of thermal feedback. Thus the hot gas gains energy with the rate

$$\frac{d}{dt}(\rho_h u_h)|_{\text{SN}} = \epsilon_{\text{SN}} f_* f_{\text{mol}} \frac{d\rho_*}{dt} = \beta u_{\text{SN}} f_* f_{\text{mol}} \frac{d\rho_c}{t_{\text{dyn}}} \quad (2.55)$$

with $\epsilon_{\text{SN}} = 4 \cdot 10^{48} \text{ erg} \cdot \text{M}_{\odot}^{-1}$ for the IMF adopted in this description [Salpeter, 1955]. Apart from the heating the supernova destroys the star forming clouds around the explosion. Thus, the cold phase loses mass as

$$\frac{d\rho_c}{dt}|_{\text{EV}} = A \beta f_* f_{\text{mol}} \frac{\rho_c}{t_{\text{dyn}}} \quad (2.56)$$

with A the evaporation parameter that scales with density as $A \sim \rho^{-4/5}$. The growth of the cold clouds is coming from the radiative cooling of the hot phase. We follow the formulation of [Springel and Hernquist, 2003] that assumes the thermal instability operating as was also explained in the first section of this chapter. The mass flow from one phase to the other due to radiative cooling is described as

$$\frac{d\rho_c}{dt}|_{\text{TI}} = -\frac{d\rho_h}{dt}|_{\text{TI}} = \frac{1}{u_h - u_c} \Lambda_{\text{net}}(\rho_h, u_h) \quad (2.57)$$

and the cooling function $\Lambda(\rho_h, u_h)$ is computed from radiative processes taking place in a primordial plasma of Hydrogen and Helium, as presented by [Katz et al., 1995]. The gas cannot cool below $\simeq 10^4$ K because lower temperatures would require proper treatment of molecular cooling. Thus we set the temperature of cold clouds to remain constant at $T_c = 10^3$ K. Taking into consideration all the processes being described, the density of the hot and cold phases are changing as

$$\frac{d\rho_c}{dt} = -f_* f_{\text{mol}} \frac{\rho_c}{t_{\text{dyn}}} - A \beta f_* f_{\text{mol}} \frac{\rho_c}{t_{\text{dyn}}} + \frac{1-f}{u_h - u_c} \Lambda_{\text{net}}(\rho_h, u_h) \quad (2.58)$$

$$\frac{d\rho_h}{dt} = \beta f_* f_{\text{mol}} \frac{\rho_c}{t_{\text{dyn}}} + A \beta f_* f_{\text{mol}} \frac{\rho_c}{t_{\text{dyn}}} - \frac{1-f}{u_h - u_c} \Lambda_{\text{net}}(\rho_h, u_h). \quad (2.59)$$

In both equations the first term in the right-hand side represents the gain/lose from the star formation, the second term accounts for the cold cloud evaporation and the last one the effect of the thermal instability. The parameter f represents the onset of the thermal instability. For $f = 0$ the thermal instability is operating and stars are forming. In the opposite case, when $f = 1$ ordinary cooling takes place. To physically differentiate the 2 cases we keep the density threshold as in [Springel and Hernquist, 2003]. Thus, star formation is happening for regions that $\rho > \rho_{\text{thr}}$. The energy of the gas is changes according to all the aforementioned processes and is described from the equation

$$\frac{d(\rho_h u_h + \rho_c u_c)}{dt} = -\Lambda_{\text{net}}(\rho_h, u_h) + \beta f_* f_{\text{mol}} \frac{\rho_c}{t_{\text{dyn}}} u_{\text{SN}} - (1 - \beta) f_* f_{\text{mol}} \frac{\rho_c}{t_{\text{dyn}}} u_c. \quad (2.60)$$

If we want to consider separately the 2 gas components of the ISM then their energy balance is written as

$$\frac{d(\rho_h u_h)}{dt} = -f_* f_{\text{mol}} \frac{\rho_c}{t_{\text{dyn}}} u_c - A\beta f_* f_{\text{mol}} \frac{\rho_c}{t_{\text{dyn}}} u_c + \frac{(1 - f)u_c}{u_h - u_c} \Lambda_{\text{net}} \quad (2.61)$$

$$\frac{d(\rho_c u_c)}{dt} = \beta f_* f_{\text{mol}} \frac{\rho_c}{t_{\text{dyn}}} (u_{\text{SN}} + u_c) + A\beta f_* f_{\text{mol}} \frac{\rho_c}{t_{\text{dyn}}} u_c + \frac{u_h - f u_c}{u_h - u_c} \Lambda_{\text{net}}. \quad (2.62)$$

In equation (2.61) and equation (2.62) with the same way the first term of the right side shows the effect of the star formation, the second term the cloud evaporation and the third term the thermal instability. As was mentioned before, the temperature of the cold clouds will remain constant to $T_c = 10^3$ K. Consequently, we assume that u_c is constant in the above equations and we can follow the evolution of the specific energy of the hot phase. From equation (2.61), using equation (2.59), the hot phase will evolve according to the equation

$$\frac{du_h}{dt} = - \left(\beta \frac{f_* f_{\text{mol}}}{t_{\text{dyn}}} \frac{\rho_c}{\rho_h} + \frac{A\beta}{t_{\text{dyn}}} \frac{\rho_c}{\rho_h} \right) u_h + f_* f_{\text{mol}} \frac{\beta}{t_{\text{dyn}}} \frac{\rho_c}{\rho_h} (u_{\text{SN}} + u_c) + f_* f_{\text{mol}} \frac{A\beta}{t_{\text{dyn}}} \frac{\rho_c}{\rho_h} u_c. \quad (2.63)$$

Surprisingly the last equation results in the same equilibrium solution as in the case of [Springel and Hernquist, 2003]. Therefore, the temperature of the hot phase will evolve towards an equilibrium state, described by

$$u_h = \frac{u_{\text{SN}}}{A + 1} + u_c. \quad (2.64)$$

Deviations from this temperature decay in a characteristic timescale

$$\tau_h = \frac{t_{\text{dyn}} \rho_h}{\beta(A + 1) f_* f_{\text{mol}} \rho_c}. \quad (2.65)$$

It is interesting to notice that this timescale depends not only on the cold fraction x but also on the molecular fraction that corresponds to each particle. Therefore, when the magnetic fields are amplified enough to provide high magnetic pressure, the molecular fraction rises

and differentiates the timescale from the timescale in a pure hydrodynamical case. As shown in figure 2.5 the mass flows from one phase to another. The growth of cold clouds is balanced from the star formation and supernova feedback towards an equilibrium and self-regulated star formation. The gas is then behaving as an effective medium with pressure

$$P_{\text{eff}} = (\gamma - 1)(\rho_h u_h + \rho_c u_c). \quad (2.66)$$

We assume that this pressure is constant. Thus, from equation (2.60) follows

$$\frac{\rho_c}{t_{\text{dyn}}} = \frac{\Lambda_{\text{net}}(\rho_h, u_h)}{f_* f_{\text{mol}}(\beta u_{\text{SN}} - (1 - \beta)u_c)}. \quad (2.67)$$

Following the definitions by [Springel and Hernquist, 2003] we can derive the cold fraction of the gas as a function of the gas density. The cooling function of the hot phase is $\Lambda_{\text{net}}(\rho_h, u_h) = (\rho_h/\rho)^2 \Lambda_{\text{net}}(\rho, u_h)$. Using the definition

$$y(x) = \frac{t_{\text{dyn}}(x) \Lambda_{\text{net}}(\rho_h, u_h)}{f_* f_{\text{mol}}(\beta u_{\text{SN}} - (1 - \beta)u_c)} \quad (2.68)$$

the ratio of the densities of the hot and cold phase is written as

$$\frac{\rho_c}{\rho_h} = \frac{\rho_h}{\rho} y(x). \quad (2.69)$$

The cold fraction is defined as

$$x = \frac{\rho_c}{\rho}. \quad (2.70)$$

The general equation of the cold fraction as a function of the parameter y holds here as well since is derived from the condition $\rho = \rho_h + \rho_c$ and equation (2.69).

$$x = 1 + \frac{1}{2y(x)} - \sqrt{\frac{1}{y(x)} + \frac{1}{4y(x)^2}}. \quad (2.71)$$

The difference in our case is that the cold fraction does not depend only on y but on the cold fraction itself since the parameter y is a non linear function of x . The dependence on the cold fraction comes from the fact that we chose the dynamical time of the cold gas and non an arbitrary timescale as a characteristic timescale of the star formation. The dynamical time depends on the cold fraction x as

$$t_{\text{dyn}} = x^{-1/2} \sqrt{\frac{3\pi}{32G\rho}}. \quad (2.72)$$

Given the non linearity of the dependencies, we can not solve for x but rather numerically find its value. The cold fraction is the root of the function

$$f(x) = 1 + \frac{\sqrt{x}}{2\delta} - \sqrt{\frac{x}{\delta} + \frac{x}{2\delta^2}} - x \quad (2.73)$$

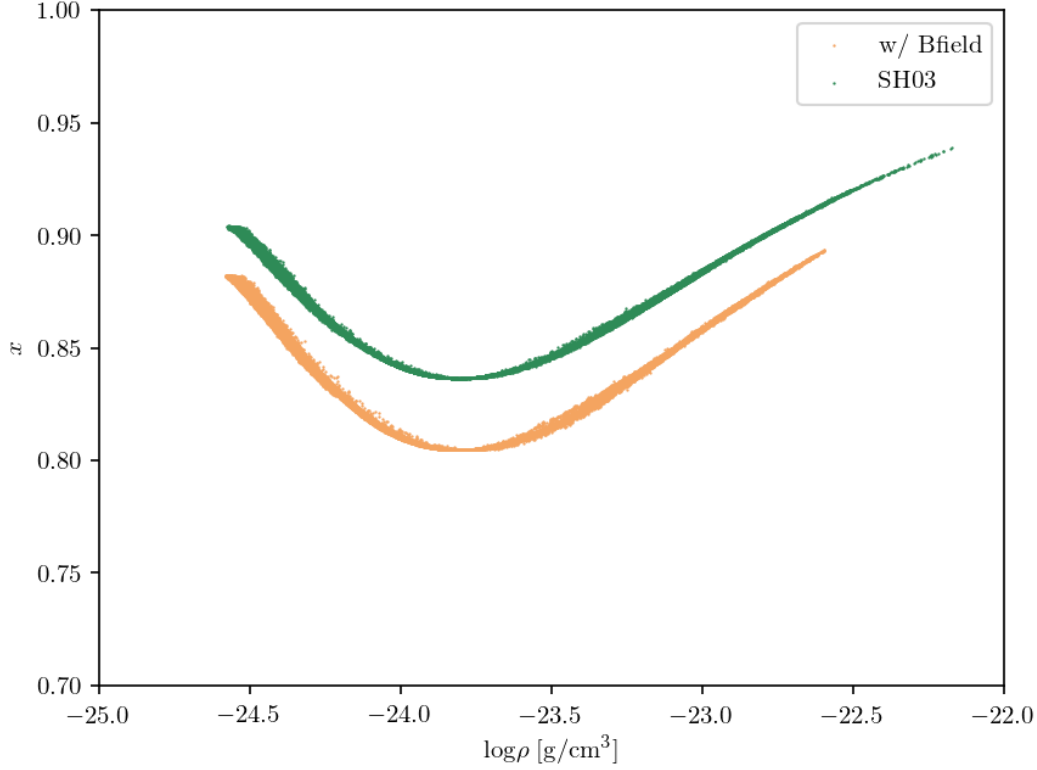


Figure 2.6: Cold fraction as a function of density. In orange points is the result of the new -pressure based- star formation model and in green the result from [Springel and Hernquist, 2003] are shown for comparison.

with δ

$$\delta = \sqrt{\frac{3\pi}{32G\rho}} \cdot \frac{\Lambda_{\text{net}}(\rho_h, u_h)}{f_* f_{\text{mol}} \rho (\beta u_{\text{SN}} - (1 - \beta) u_c)}. \quad (2.74)$$

After testing that the equation (2.73) has a solution we numerically solve it with a simple bisection method. The dependence of the x on the density of the gas is shown in figure 2.6. For comparison we also plot at the same figure the cold fraction as calculated by [Springel and Hernquist, 2003]. The obvious difference is that in our case the cold gas fraction reaches lower values and also does not convert to 1 for high densities. This is coming from the dependence of the dynamical time on the cold fraction that inserts a complicated form of correlation between x and ρ . Thus for high densities we don't allow all the gas to be in the cold phase and form more and more stars but we have included other regulation factors such as the external pressure of the ISM through the molecular fraction f_{mol} . The gas particle enters the multiphase model once its density is higher than a density threshold. Below this density we set the $x = 0$. This is calculated from the model equations and will be discussed in the next section.

2.3.2 Selection of parameters

The evaporation factor A scales with the local density of the ISM which is theoretically motivated by [McKee and Ostriker, 1977]. We scale it with the density threshold as

$$A(\rho) = A_0 \left(\frac{\rho}{\rho_{\text{thr}}} \right)^{-4/5} \quad (2.75)$$

with the parameter being set to $A_0 = 1000$ as explained in section 2.1.2. The density threshold is calculated using equation (2.68). A straightforward way to compute the density threshold is to use the fact that $\Lambda(\rho, u) = \Lambda_{\text{net}}(\rho, u)/\rho^2$ and $\rho = \rho_h + \rho_c$ and then solve for ρ . However the result is an un-physically high density threshold that does not allow the majority of the particles to enter the multiphase model. We should also notice that the cooling function Λ needs a density as an input in order to calculate its value and this is not the density threshold that we are calculating here. The case is the same if we write the cooling function as $\Lambda_{\text{net}}(\rho, u_h)/\rho = u_h/t_{\text{cool}}$ since the cooling time requires the density for its calculation as well. In order to solve this problem we assume an arbitrary baryon over-density calculated as $\rho_{\text{ov}} = 10^5 \frac{3H^2}{8\pi G}$ and calculate the dynamical time and the cooling function given this density. Therefore the density threshold is calculated as

$$\rho_{\text{thr}} = \frac{x_{\text{thr}}}{(1 - x_{\text{thr}})^2} \frac{f_{\text{mol}}(\beta u_{\text{SN}} - (1 - \beta)u_c)}{f_* t_{\text{dyn}}(\rho_{\text{ov}}) \Lambda(\rho_{\text{ov}}, u_{\text{SN}}/A_0)}. \quad (2.76)$$

The cooling function is calculated at the threshold where $u_h = u_{\text{SN}}/A_0 + u_c \simeq u_{\text{SN}}/A_0$ and the cold fraction at the threshold $x = x_{\text{thr}}$, which is given by $x_{\text{thr}} = 1 + (A_0 + 1)(u_c - u_4)/u_{\text{SN}} \simeq 1 - A_0 u_4/u_{\text{SN}}$. The latter quantity is calculated by setting the condition $u_{\text{eff}}(\rho_{\text{thr}}) = u_4$, where u_4 is the specific energy that corresponds to temperature of $T_4 = 10^4$ K. This implies that the pressure is a continuous function of density and should stay constant before and after the onset of the star formation which happens at $\rho = \rho_{\text{thr}}$. A more careful consideration would require the treatment of magnetic fields. To be more specific, instead of taking into account only the effective specific energy of the gas we should include the magnetic energy or alternatively to consider the sum of the magnetic pressure plus the gas pressure being continuous function of density. The magnetic pressure and energy scales with B^2 which scales with the density as $\rho^{2/3}$. This would include more complication in the calculation of the cold fraction at the threshold and is not crucial for the simple approach that we are adopting here. In equation (2.76) we notice that the density threshold depends on the molecular fraction of the gas, which changes from particle to particle. There are two options of setting the molecular fraction at the threshold. The first is to consider the pressure of the gas particle (thermal pressure plus the magnetic pressure) in the calculation of the molecular fraction. This means that the density threshold changes from gas particle to gas particle. However, we have already set the condition of continuous pressure on the onset of star formation to be P_4 , i.e., the pressure that corresponds to temperature of 10^4 K. It is then a natural consequence to use this pressure in order to calculate the

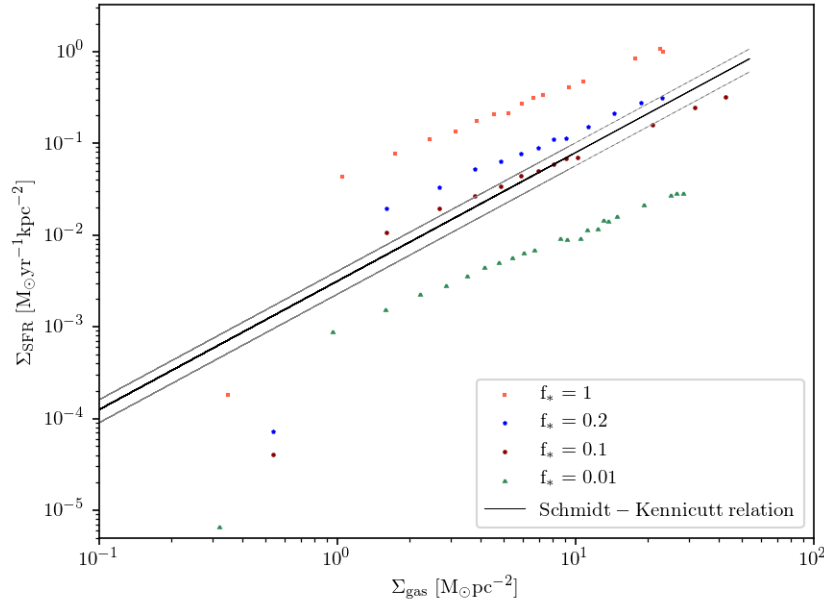


Figure 2.7: Star formation rate per surface as a function of the surface density of the gas in a galaxy for different star formation efficiency parameters. The black solid line is the observational Schmidt Kennicutt relation and the grey lines its errors. (The quantities are azimuthally averaged).

molecular fraction at the threshold, which will be

$$f_{\text{mol}}(P_4) = \frac{1}{1 + P_0/P_4} \quad (2.77)$$

The density threshold is now calculated as

$$\rho_{\text{thr}} = \frac{x_{\text{thr}}}{(1 - x_{\text{thr}})^2} \frac{f_{\text{mol}}(P_4)(\beta u_{\text{SN}} - (1 - \beta)u_c)}{f_* t_{\text{dyn}}(\rho_{\text{ov}})\Lambda(\rho_{\text{ov}}, u_{\text{SN}}/A_0)} \quad (2.78)$$

Another parameter that we should specify, which is a free parameter of the model, is the efficiency of the star formation process. This is equivalent with the idea to use the dynamical time as a timescale of the star formation or a timescale proportional to the dynamical timescale $\sim \alpha \cdot t_{\text{dyn}}$. The efficiency of the star formation is related with the gas component of the galaxy and especially the cold gas. These two quantities are correlated, as observations show, according to the Schmidt-Kennicutt relation (equation (2.22)), which is a tight relation between the star formation of the galaxy and the surface density of the gas of the galaxy. In order to constrain the efficiency parameter f_* we run test simulations of an isolated Milky Way type galaxy, with different predictions as shown in figure 2.7. In order to reproduce the Schmidt Kennicutt relation the value of the efficiency parameter should be $f_* = 0.1$. This corresponds to a star formation timescale of $10 \cdot t_{\text{dyn}}$.

Moreover, as far as the molecular fraction is concerned, we set the parameter P_0 to be $P_0/k = 35000 \text{ cm}^{-3}\text{K}$ according to the observations of [Blitz and Rosolowsky, 2006]. However, in their observations they notice two different groups of galaxies and for each one of them the parameter P_0 changes significantly. There are three galaxies that on average they find $P_0/k = 7700 \text{ cm}^{-3}\text{K}$ and for the rest of the galaxies they find $P_0/k = 43000 \text{ cm}^{-3}\text{K}$. They attribute this difference on the content of neutral hydrogen that each galaxy has. The mean value of the projected surface density of the neutral hydrogen, as calculated from observations, may be low due to intense tidal or ram pressure stripping. We have to account for all galaxies so we try to change this parameter and see its effect. To do that we run three different simulations with parameters $P_0/k = 20000 \text{ cm}^{-3}\text{K}$, $P_0/k = 35000 \text{ cm}^{-3}\text{K}$ and $P_0/k = 43000 \text{ cm}^{-3}\text{K}$ and then we check how alters the relation between the star formation and gas through the Schmidt-Kennicutt relation. The results are displayed in figure 2.8. Even if the change of the value for the P_0 is relatively wide, there is not a significant change in the star formation and only an insignificant deviation from the Schmidt-Kennicutt relation. Therefore we will chose $P_0/k = 35000 \text{ cm}^{-3}\text{K}$ as is the mean value among all the galaxies that where examined in [Blitz and Rosolowsky, 2006].

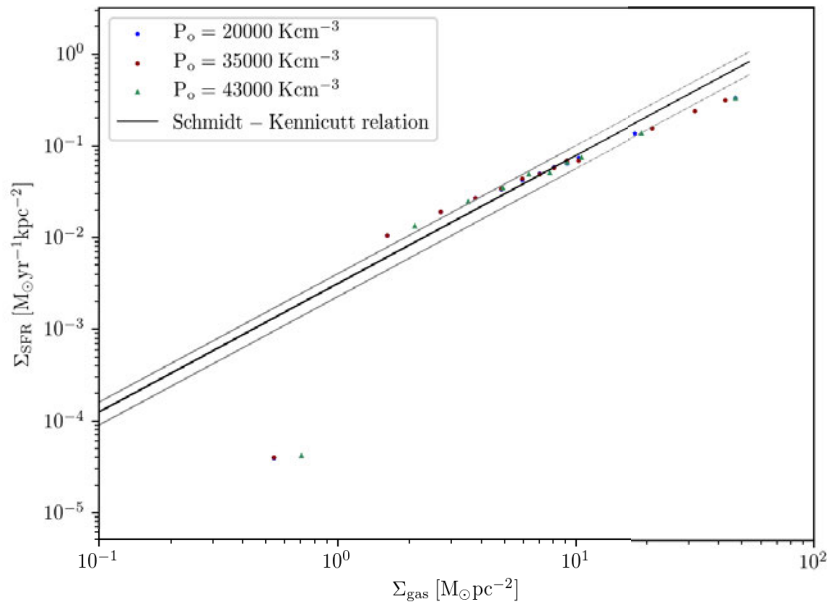


Figure 2.8: Star formation rate per surface as a function of the surface density of the gas in a galaxy for different values of the parameter P_0 . The black solid line is the observational Schmidt Kennicutt relation and the grey lines its errors.

The last parameter that we examine is the assumption about the temperature of cold clouds. This was assumed to be constant at $T_c = 1000 \text{ K}$ but this is not even close to the temperatures that stars are formed in reality. Therefore, we examine the case of lowering the temperature of the cold gas and we run a test simulation for $T_c = 300 \text{ K}$,

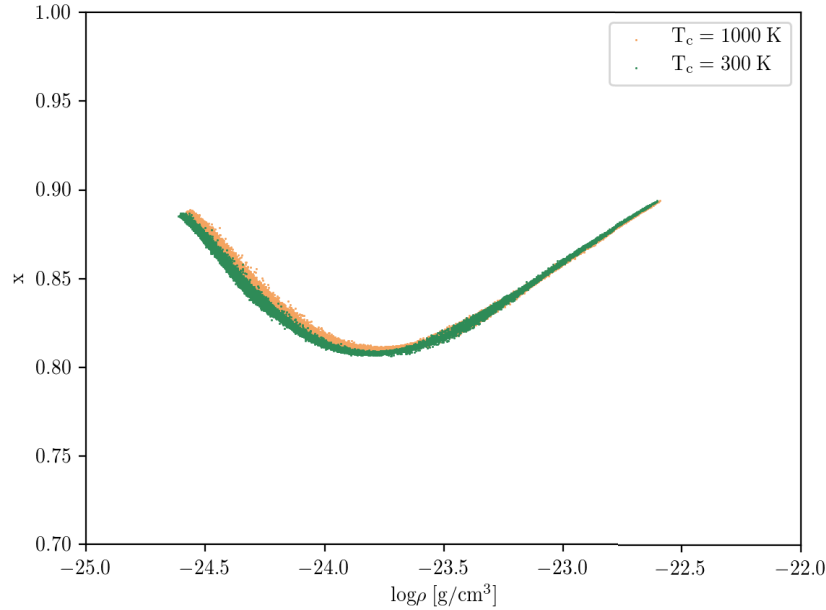


Figure 2.9: Cold fraction as a function of the gas density. In orange is the result of the new -pressure based- star formation model and in green the case for lower temperature of the cold clouds.

Table 2.1: Table of model parameters

parameter	f_*	P_0/k	β	A_0	T_c	T_{SN}
value	0.1	$35000 \text{ cm}^{-3}\text{K}$	0.1	1000	1000 K	10^8 K

which is motivated from [Murante et al., 2014]. In figure 2.9 is displayed the cold fraction as a function of the density of the gas. The lower temperature barely affects the cold fraction as is shown in it figure 2.9 and the overall star formation behaviour as is shown in comparison to the Schmidt Kennicutt relation in figure 2.10. The density threshold changes slightly because of its dependence on u_c . However we should keep in mind that the gas at temperatures lower than $10^3 - 10^4 \text{ K}$ need molecular cooling for a proper treatment. Since this is not included in our simulations, we will keep the temperature of the cold clouds constant to 10^3 K .

In table 2.1 a summary of the parameters of our model is shown.

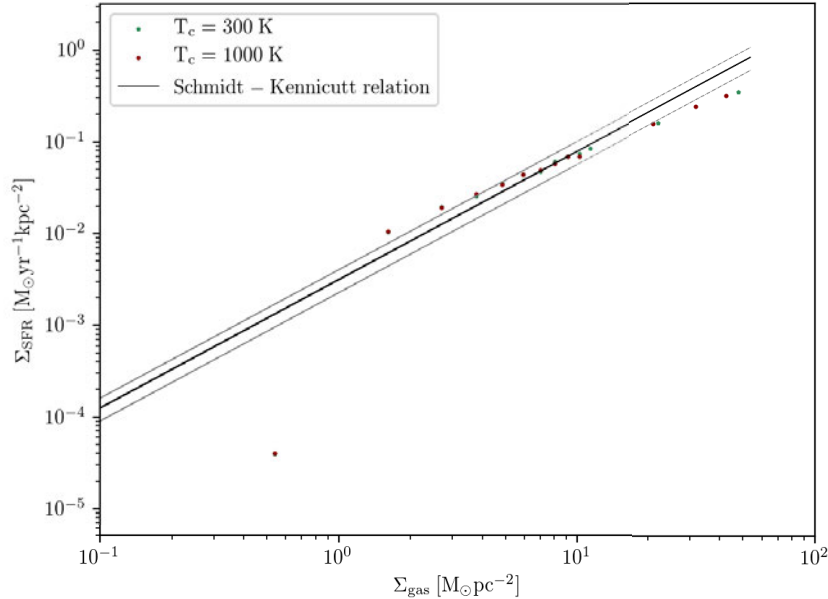


Figure 2.10: Star formation rate per surface as a function of the surface density of the gas in a galaxy for different temperature of cold clouds. The black solid line is the observational Schmidt Kennicutt relation and the grey lines its errors.

2.4 Magnetic seeding model

The main aim of this work is to study the interplay between star formation and magnetic fields in galaxy simulations. The first part is to include the effect of the magnetic field in the star formation recipe of the code that was done in section 2.3. The second part would be to study how the star formation alters the magnetic field in a galaxy. This mostly happens through the supernova feedback. For this reason we will use the magnetic seeding model by [Beck et al., 2013]. According to this model, we do not assume primordial magnetic field in the galaxy, but we rather couple its seeding with the supernova explosions. In the supernova remnants, a dipole-shaped magnetic field is injected in a rate 10^{-9} GGyr $^{-1}$. The magnetic field is then amplified and transported through turbulent diffusion, shocks and gas motions.

The origin of magnetic field is still highly debated in the scientific community. The most widely accepted idea is that primordial magnetic field was created during structure formation and then was amplified and transported with different MHD processes. Battery effects can create tiny seed magnetic fields during the formation of the first stars and were locally enhanced by gravitational compression. Then through the evolution and death of stars magnetic fields enrich the interstellar medium. Within the galaxy, the fact that seed fields are connected with the supernova explosions and their existence has already been studied by [Bisnovaty-Kogan et al., 1973, Chyży, 2008, Kronberg et al., 1999]. In

[Beck et al., 2013] they introduce a model for the seeding of the magnetic fields by SN explosions. The model is coupled in the star formation model and here we will show a basic description of the model and how this is coupled to the new star formation model that we introduced in the previous section.

2.4.1 Supernova seeding model equations

In order to include the effect of the magnetic field seeding, an extra term is included in the induction equation.

$$\frac{\partial \mathbf{B}}{\partial t} = \nabla \times (\mathbf{v} \times \mathbf{B}) + \eta \nabla^2 \mathbf{B} + \left. \frac{\partial \mathbf{B}}{\partial t} \right|_{\text{seed}} \quad (2.79)$$

with the seeding term

$$\left. \frac{\partial \mathbf{B}}{\partial t} \right|_{\text{seed}} = \sqrt{N_{\text{SN}}^{\text{eff}}} \frac{B_{\text{inj}}}{\Delta t} \mathbf{e}_B \quad (2.80)$$

where \mathbf{e}_B is a unit vector in the direction of the seeding, B_{inj} is the amplitude of the field that is injected and $N_{\text{SN}}^{\text{eff}}$ is a normalization constant that is connected with the number of supernova explosions. The last parameter is not a free parameter of the model but is calculated directly from the star formation model of the code. For the new star formation model, the mass of stars that are formed in each timestep Δt is calculated as

$$m_* = f_* f_{\text{mol}} m_c \frac{\Delta t}{t_{\text{dyn}}} \quad (2.81)$$

where m_c is the mass of the cold clouds, f_* is the star formation efficiency, f_{mol} the molecular fraction and t_{dyn} the dynamical time of the cold gas that is given by

$$t_{\text{dyn}} = x^{-1/2} \sqrt{\frac{3\pi}{32G\rho}} \quad (2.82)$$

and x is the cold fraction of the gas. The effective number of supernova explosions is given by

$$N_{\text{SN}}^{\text{eff}} = \alpha m_* \quad (2.83)$$

with α being a parameter that specifies the number of supernova explosions per solar mass. For our case we adopt the Salpeter IMF [Salpeter, 1955] with slope -1.35 and the parameter α is $\alpha = 0.008 M_{\odot}^{-1}$. The total injected magnetic field for all SN explosions is given by

$$B_{\text{inj}}^{\text{all}} = \sqrt{N_{\text{SN}}^{\text{eff}}} B_{\text{SN}} \left(\frac{r_{\text{SN}}}{r_{\text{SB}}} \right)^2 \left(\frac{r_{\text{SB}}}{r_{\text{inj}}} \right)^3 \quad (2.84)$$

where B_{SN} is the mean strength of magnetic fields in supernova explosions, r_{SB} is the superbubble of the explosion assuming spherical geometry for the remnant, r_{SN} is a typical radius of the supernova remnant and r_{inj} is determined by the smoothing length of the

simulation and shows the region where the superbubbles are placed. Thus, the magnetic field seeding rate for this model is given by

$$\dot{B}_{\text{seed}} \simeq B_{\text{SN}} \left(\frac{r_{\text{SN}}}{r_{\text{SB}}} \right)^2 \left(\frac{r_{\text{SB}}}{r_{\text{inj}}} \right)^3 \frac{\sqrt{N_{\text{SN}} \Delta t}}{\Delta t} \quad (2.85)$$

The supernova radius is assumed to be $r_{\text{SN}} = 5\text{pc}$, a typical value for the magnetic field strength is $B_{\text{SN}} = 10^{-4}\text{G}$ which is then distributed in a bubble of radius $r_{\text{SB}} = 25\text{pc}$. The magnetic field configuration that is added in the induction equation should be divergence free. Therefore a straightforward way is to assume a dipole structure of the magnetic field seed, so

$$\frac{\partial \mathbf{B}}{\partial t} \Big|_{\text{seed}} = \frac{1}{|\mathbf{r}|^3} \left[3 \left(\frac{\partial \mathbf{m}}{\partial t} \cdot \mathbf{e}_r \right) \mathbf{e}_r - \frac{\partial \mathbf{m}}{\partial t} \right] \quad (2.86)$$

with \mathbf{m} the dipole magnetic moment, \mathbf{e}_r is a unit vector in the \mathbf{r} direction. The time derivative of each dipole moment is written as

$$\frac{\partial \mathbf{m}}{\partial t} = \sigma \frac{B_{\text{inj}}^{\text{all}}}{\Delta t} \mathbf{e}_B \quad (2.87)$$

where \mathbf{e}_B is the direction of the seed magnetic field which is chosen to be in the direction of the acceleration of the particle, hence $\mathbf{e}_B = \mathbf{a}/|\mathbf{a}|$. The normalization constant σ is given by

$$\sigma = r_{\text{inj}}^3 \sqrt{\frac{1}{2} f^3 (1 + f^3)} \quad (2.88)$$

with $f = r_{\text{soft}}/r_{\text{inj}}$ is the ration between the softening and injection length. The parameter σ is used to normalize the energy that is injected and also to soften the magnetic dipoles in the center and be truncated in the scale of the injection length.

Chapter 3

Simulations

In this chapter we will present the simulations that were performed in order to study the new star formation model and the interplay of magnetic fields and star formation processes. Before moving in the galaxy simulations we perform a couple of shock tube tests in order to ensure that the magnetohydrodynamics (MHD) is working properly in the code.

3.1 MHD shock tube tests

The MHD section of GADGET was implemented by [Dolag and Stasyszyn, 2009]. Before starting the full MHD simulation of galaxies we perform a few MHD shock tube test selected from [Ryu et al., 1995]. These are the well known and well tested Ryu Jones (RJ) shock tube tests. Here we chose the RJ1A, RJ2A and RJ5A which is also known as Brio Wu test ([Brio and Wu, 1988]). For each of the tests we compare with the corresponding results of the ATHENA code [Stone et al., 2008]. The summary of the parameter of each test are shown in table 3.1.

For the initial conditions set up we use glass-like [White et al., 1996] density distributions in a 3D set up. To achieve that, the particles are randomly distributed in a volume and then are left to relax until they reach an equilibrium state which is quasi force free and has homogeneous density. From these glass density distributions we set up the initial conditions for the three shock tube tests which are based in 5^3 particles for low-density regions and 10^3 particles for high-density regions. These unit volumes are combined together in order to set up a large box in x direction, enough for the shock propagation. For these tests we assume same particle mass, ideal gas with $\gamma = 5/3$ and an equivalent of 64 neighbors for the calculation of the SPH smoothing length.

We start with the Ryu Jones 1A shock tube test or RJ1A which involves 2 fluids with same density, two dimensional magnetic field and velocity in x-direction. In figure 3.1 the results from the first MHD shock tube test are shown. We notice a strong shock that is manifested in the v_x as shown in the middle panel of the upper row in figure 3.1. This strong shock is responsible for the notice in the energy, pressure and v_y . The plot show two fast shocks, one slow rarefaction (left-facing), one slow shock (right-facing) and a constant discontinuity.

Table 3.1: Initial conditions for the left and right side of the shock tubes for the MHD tests.

Left Side				
Test	ρ	v	B	P
RJ1A	1.00	[10.0,0.0,0.0]	[5.0,5.0,0.0]/ $\sqrt{4\pi}$	20.00
RJ2A	1.08	[1.2,0.01,0.5]	[2.0,3.6,2.0]/ $\sqrt{4\pi}$	0.95
RJ5A	1.00	[0.0,0.0,0.0]	[0.75,1.0,0.0]/ $\sqrt{4\pi}$	1.00
Right Side				
	ρ	v	B	P
RJ1A	1.000	[-10.0,0.0,0.0]	[5.0,5.0,0.0]/ $\sqrt{4\pi}$	1.00
RJ2A	1.000	[0.0,0.0,0.0]	[2.0,4.0,2.0]/ $\sqrt{4\pi}$	1.00
RJ5A	0.125	[0.0,0.0,0.0]	[0.75,-1.0,0.0]/ $\sqrt{4\pi}$	0.10

The second shock tube test is the Ryu Jones 2A test problem which solution is presented in figure 3.2. This test involves a three-dimensional magnetic field structure and three-dimensional velocity for the left fluid. In this case two fast shocks and two slow shocks are propagating away from the contact discontinuity. The features of this MHD shock are well captured and we do not notice over-smoothing of sharp characteristics. The last but most important test for the MHD is the Ryu Jones 5A (RJ5A) or the Brio Wu test. This is an important test since it produces a compound structure, i.e., a rarefaction and shock propagating together and therefore we can test the code at different regimes. These shocks reverse the direction of B_y which leads to a flow that passes from super-Alfvénic to sub-Alfvénic flow. The code reproduces accurately the expected features of the test and any smoothing is a result of the regulation scheme of the magnetic field.

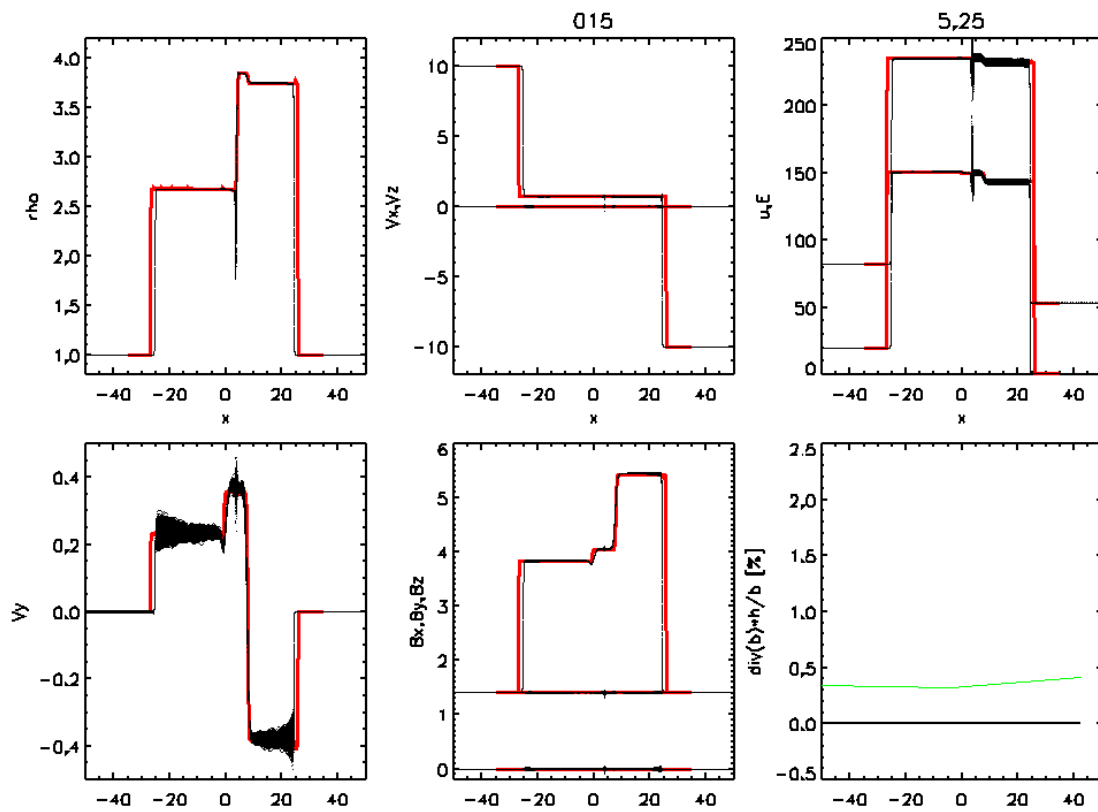


Figure 3.1: RJ1A test, $t = 5.25$. In all plots the red line shows the result from ATHENA code while the black lines are the results from the tests using GADGET code. From left to right in the upper row the first panel shows the density, the middle shows the $v_{x,z}$ and the right panel the total energy and thermal energy. In the low row the first panel shows the v_y , the middle shows all the components of the magnetic field and the last one shows the relative divergence error. In the x axis is always the x-direction of the tube.

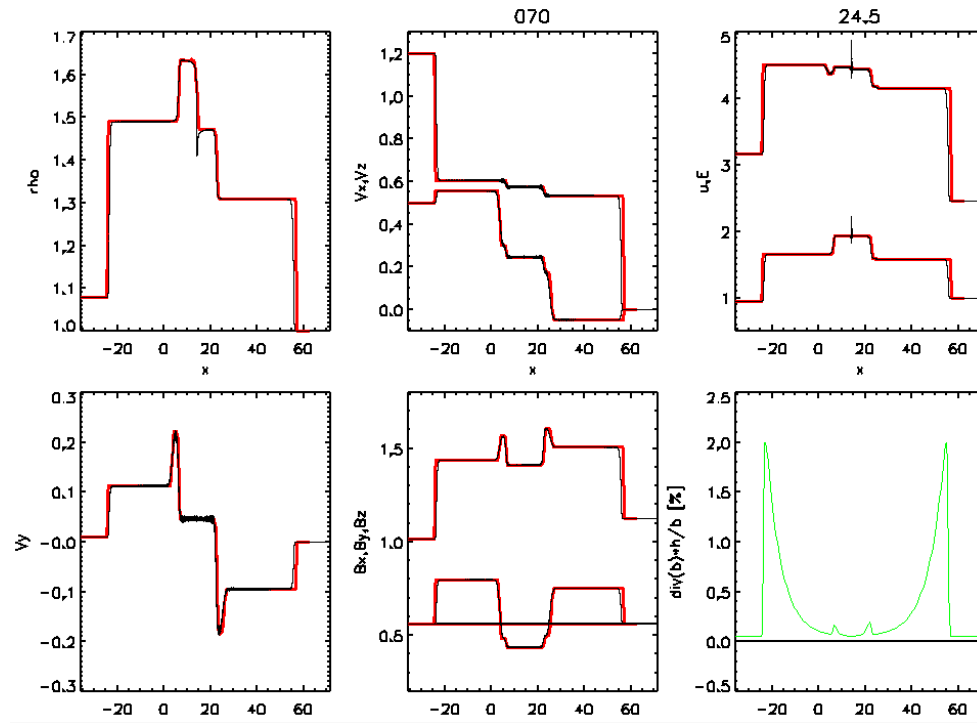


Figure 3.2: Test RJ2A, $t = 24.5$. Same plots as in figure 3.1.

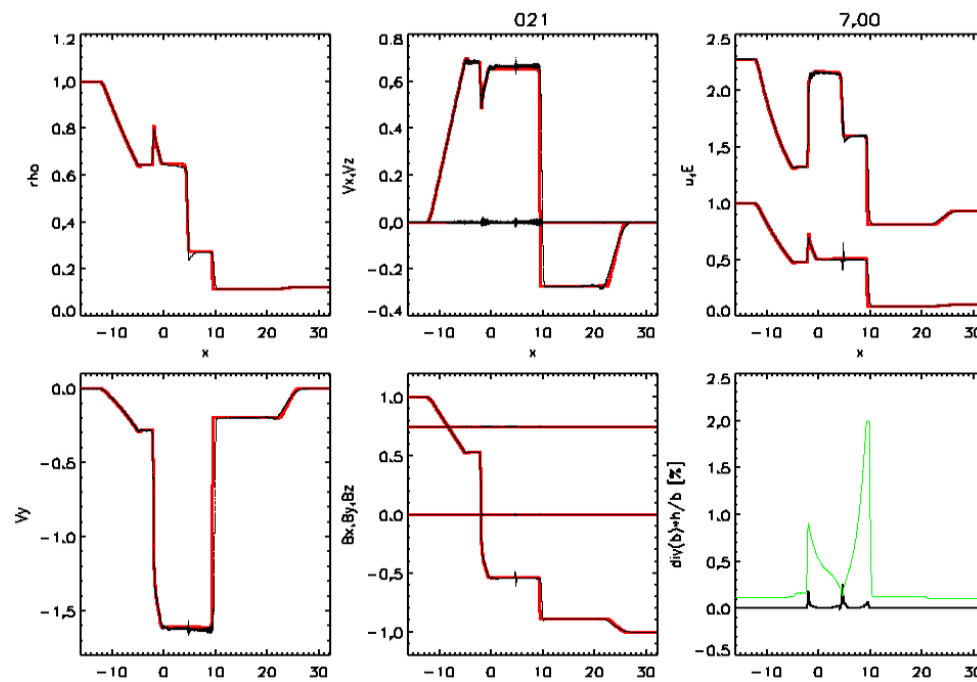


Figure 3.3: Test RJ5A, $t = 7$. Same plots as in figure 3.1

3.2 Simulations of isolated disk galaxies

3.2.1 Numerical set up

In order to test how the new star formation model is working within the code we run simulations of an isolated disk galaxy of total mass $10^{12} M_{\odot}$. We generate the initial conditions for the galaxy using the galactic models that was first described in [Hernquist, 1993] and further developed in [Springel and White, 1999] and [Springel et al., 2005]. The galactic model consists of gas, a bulge, a stellar disk and dark matter. The dark matter and bulge mass distribution is following a Hernquist profile [Hernquist, 1993], which radial density distribution for the dark matter is given by

$$\rho_{\text{DM}}(r) = \frac{M_{\text{DM}}}{2\pi} \frac{\alpha}{r(r + \alpha)^3} \quad (3.1)$$

with α a parameter that related the concentration c with the scale length r_s . The same profile describes the bulge of the galaxy as well

$$\rho_b(r) = \frac{M_b}{2\pi} \frac{l_b}{r(r + l_b)^3} \quad (3.2)$$

with l_b the scale length of the bulge which is a free parameter. M_b is the mass of the bulge and is calculated as $M_b = m_b M_{200}$, here the parameter m_b is the mass fraction of the bulge and M_{200} is the mass that is enclosed in a radius of $r = 200$ pc. The stellar disk follows an exponential profile which is given from the following equation

$$\Sigma_* = \frac{M_*}{2\pi l_d^2} e^{-r/r_d} \quad (3.3)$$

The gaseous part of the disk follow an exponential profile as well

$$\Sigma_{\text{gas}} = \frac{M_{\text{gas}}}{2\pi l_d^2} e^{-r/r_d} \quad (3.4)$$

In both equations l_d has to be specified and is the scale length of the disk. Both components compose the mass of the disk $M_d = M_* + M_{\text{gas}} = m_d M_{200}$, with m_d the mass fraction of the disk. The rest of the mass is assigned to the dark matter component of the galaxy as $M_{\text{DM}} = M_{200} - (m_b + m_d) M_{200}$. The last parameter that we need to specify is the spin parameter of the galaxy that is correlated with the total angular momentum of the galaxy J as

$$\lambda = \frac{J|E|^{1/2}}{GM^{5/2}} \quad (3.5)$$

with M the total mass of the galaxy. In table 3.2 we summarize the parameters for the initial conditions of the Milky Way type galaxy that we use to test the 2 star formation models. The numbers of different particle components were calculated from the mass

Table 3.2: Parameters for the initial conditions of isolated Milky Way type galaxy

Disk Parameters		
Total mass [$10^{10} M_{\odot}$]	M_{200}	100
Virial radius	r_{200}	145
Halo concentration	c	12
Spin parameter	λ	0.033
Disk spin fraction	j_d	0.067
Disk mass fraction	m_d	0.067
Bulge mass fraction	m_b	0.034
Disk scale length [kpc]	l_d	2.1
Disk height [l_d]	z_0	0.2
Bulge size [l_d]	l_b	0.2

Table 3.3: Number of different particle types

Particle Numbers [10^6]		
Gas in the disk	N_{gd}	1.2
Stellar Disk	N_{sd}	4.8
Stellar Bulge	N_b	2.0
Dark matter	N_{DM}	6.9

fraction parameter that we chose and are shown in section 3.2.1. The mass resolution for the different particles are presented in table 3.4. Last but not least, the gravitational softening is calculated as

$$\epsilon = \epsilon_{\text{old}} \left(\frac{m}{m_{\text{old}}} \right)^{1/3} \quad (3.6)$$

with m the mass resolution of the simulation. As reference *old* we use the parameters from the MAGNETICUM ¹ simulations [Hirschmann et al., 2014]. For the gas particles the gravitational softening is $\epsilon_{\text{gas}} = 0.1$ kpc/h for the stellar particles $\epsilon_{\text{stars}} = 20$ pc/h, and for the dark matter particles $\epsilon_{\text{DM}} = 83$ pc/h.

Table 3.4: Mass resolution

Mass resolution in M_{\odot}		
Gas particles	m_{gas}	4800
Stellar particles	m_{star}	4800
Dark matter particles	m_{DM}	96000

¹<http://www.magneticum.org/simulations.html>

3.2.2 Results: Galaxy with SH03 star formation model

First of all, for comparison, we perform simulations of an isolated Milky Way disk galaxy with the default star formation model in GADGET ([Springel and Hernquist, 2003], SH03 hereafter). We perform simulations with the same setup and different magnetic field models. First, a pure hydrodynamical simulation without magnetic fields (noB), second a fully magnetohydrodynamical (MHD) simulation assuming primordial origin of the magnetic fields (B) and last, a MHD simulation with supernova seeding (snB) of the magnetic field, a feedback model that was described in section 2.4. Thus for the High Mass Galaxy (HMG), which is a Milky Way type galaxy, we follow the name conventions: HMG-noB-SH03, HMG-B-SH03 and HMG-snB-SH03 for each of the aforementioned magnetic field configurations. The ending *SH03* is a reminder for the star formation that we are using, i.e., by [Springel and Hernquist, 2003]. This star formation model is widely used in galaxy and cosmological simulations, for example in [Kotarba et al., 2009] and [Hirschmann et al., 2014]. Here we briefly present the basic results of the simulation.

In figure 3.4 the effective temperature of the gas as a function of the gas density is displayed. The color code corresponds to the star formation rate per particle. From the plot it is obvious that the density threshold is at $\rho_{\text{thr}} = 2.75 \cdot 10^{-25} \text{ g} \cdot \text{cm}^{-3}$. Particles with density lower than the density threshold are not star-forming (purple color) and they follow normal cooling. Contrary, particles with higher density enter the multiphase model and they are star-forming with star formation rate higher for high densities. This phase diagram is from the simulation without magnetic fields, however this plot barely changes for the different simulations of this category. The phase diagrams for the different simulations can be found in the Appendix. The star formation rate as a function of the galaxy radius r is demonstrated in figure 3.5. The star formation is higher in the center of the galaxy since there is more gas and drops in the outer parts of the galaxy. The different models for the magnetic field have a slightly different behavior on the star formation rate profile which is only visible after 1.5 Gyr. The star formation rate as a function of time is shown in figure 3.6, which indicates the same tendency. In the beginning the model is bursty, producing many stars and then gradually drops since it consumes the gas of the galaxy. The only feedback is the supernova explosions which is enough to stabilize the star formation but with low star formation rate. In figure 3.7 the radial profiles of the different pressure components are displayed. We calculate the mean thermal pressure (dark blue) and magnetic pressure (magenta) in radial bins. The thermal pressure falls with radius since there is less gas in the outer parts of the galaxy and there is not enough pressure support. On the other hand, the magnetic field pressure rises in the outer parts of the galaxy. This happens due to high velocities of the gas in the external parts of the galaxy, which amplify the magnetic field through the $\alpha - \Omega$ dynamo. In the case of HMG-B, we set a primordial magnetic field in the x direction as $\mathbf{B} = (B_0, 0, 0)$ with $B_0 = 10^{-9} \text{ G}$. From the magnetic pressure ($\sim B^2$) in figure 3.7 we notice that the magnetic field is indeed amplified. However, a look at the face on projection of the galaxy for both models of the magnetic field as shown in figure 3.8, reveals that the magnetic field is not amplified enough. To be more specific, in figure 3.8a the galactic disk is magnetized with higher magnetic field

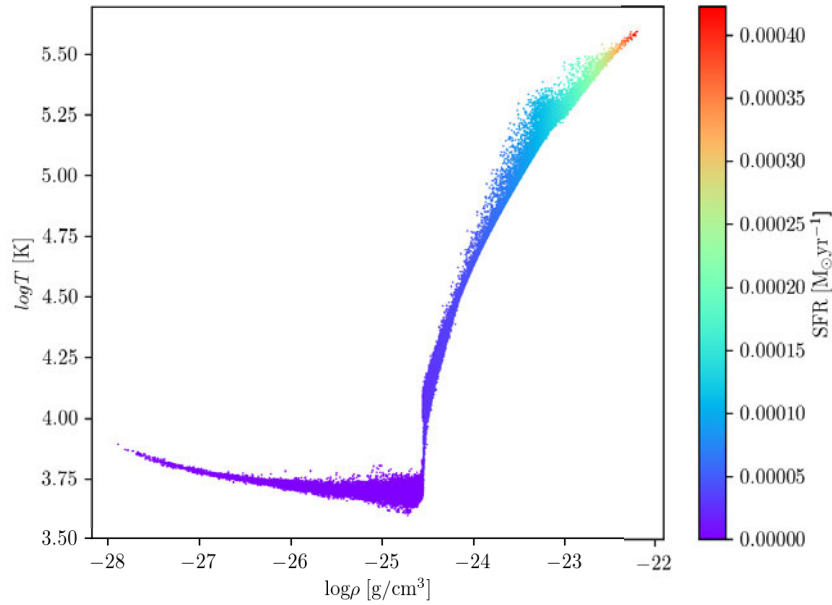


Figure 3.4: Phase diagram at $t = 0.01$ Gyr for the high mass galaxy (HMG-SH) color coded by the star formation rate per particle.

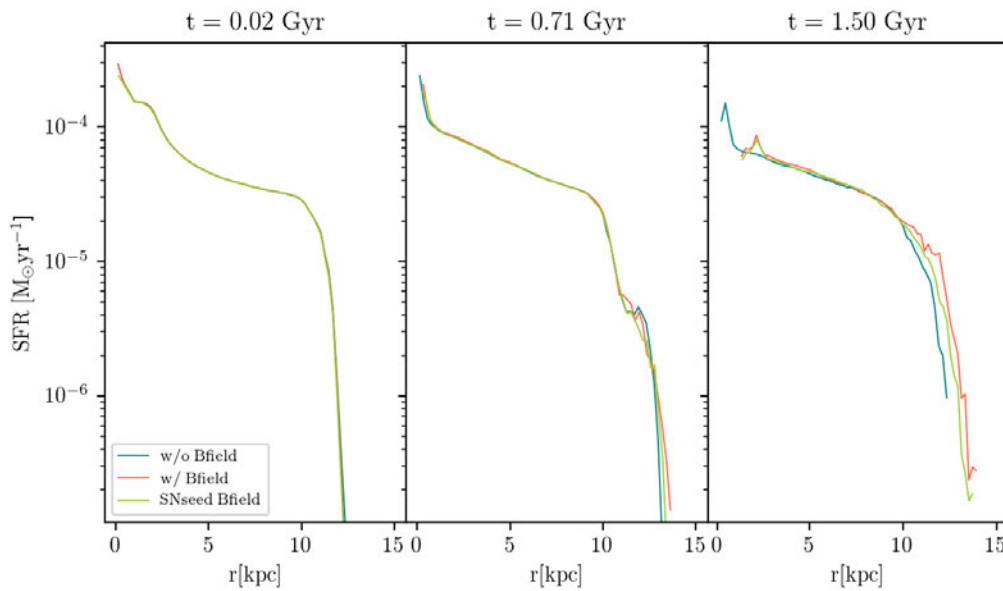


Figure 3.5: Radial profile of star formation rate for the HMG using SH03. As the legend implies, the light blue line corresponds to the simulation without magnetic fields, the orange to the simulation with magnetic fields and finally the green to the simulation with the supernova seeded magnetic fields.

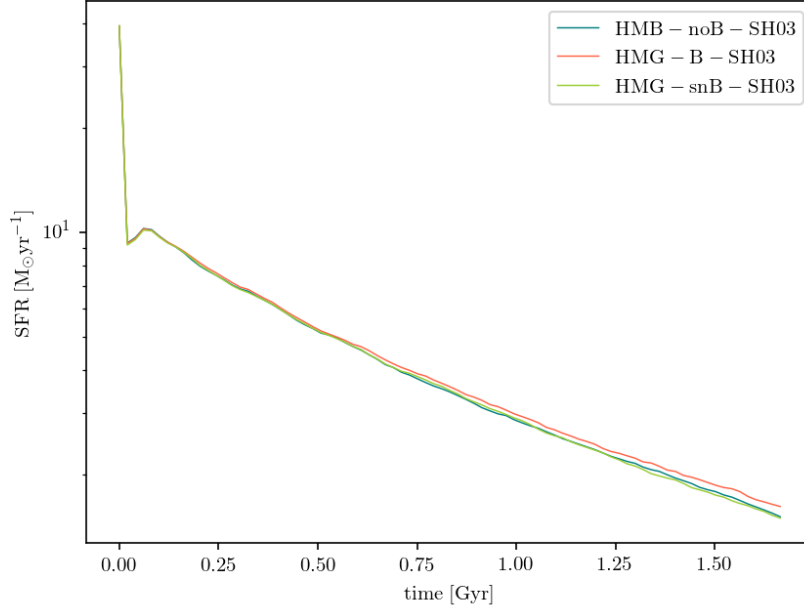


Figure 3.6: Star formation rate as a function of the time. The colors indicate the different set up for the magnetic field. In blue the galaxy without magnetic field, in orange with primordial magnetic field and in green the galaxy with supernova seeded magnetic field.

strength in the central region of the galaxy because of the higher star formation rate and in the outer part of the disk due to the dynamo action. For this model we start with an unmagnetized disk and the seed of the field is $\sim 10^{-9}$ G/Gyr in the supernova remnants. Therefore, the magnetic field is further amplified through the turbulent dynamo which is mainly supported from the supernova feedback. In the simulation with the primordial magnetic field we notice that after 1 Gyr the magnetic field has not reached the typical values of μG in the disk but rather in the outer parts of the galaxy. In figure 3.8a the high amplification on the edge of the galaxy which is coming from the rotation of the galaxy is shown. It is important to notice that in these plots the density of the particles is smoothed according to the kernel that we use for the simulations (Wendland C4). This may make this strange configuration of the high field strength on the edges seem particularly strong, but in reality the density of the galaxy is very low on this region and there are just a few particles with low density that gained the high magnetic field due to rotation. The absence of any astrophysical environment around the galaxy is one of the reasons for this feature as it will become obvious from further simulations. One has only to think that just in the density interpolation in a SPH code. The kernel should be at least symmetrical in the relative distance of 2 particles. This assumption totally breaks for the outer particles of the disk due to the fact that there are a few particles (in the edge of the disk) which do not have any neighbors. Therefore, the magnetic field calculation is not trusted in these parts of the galaxy.

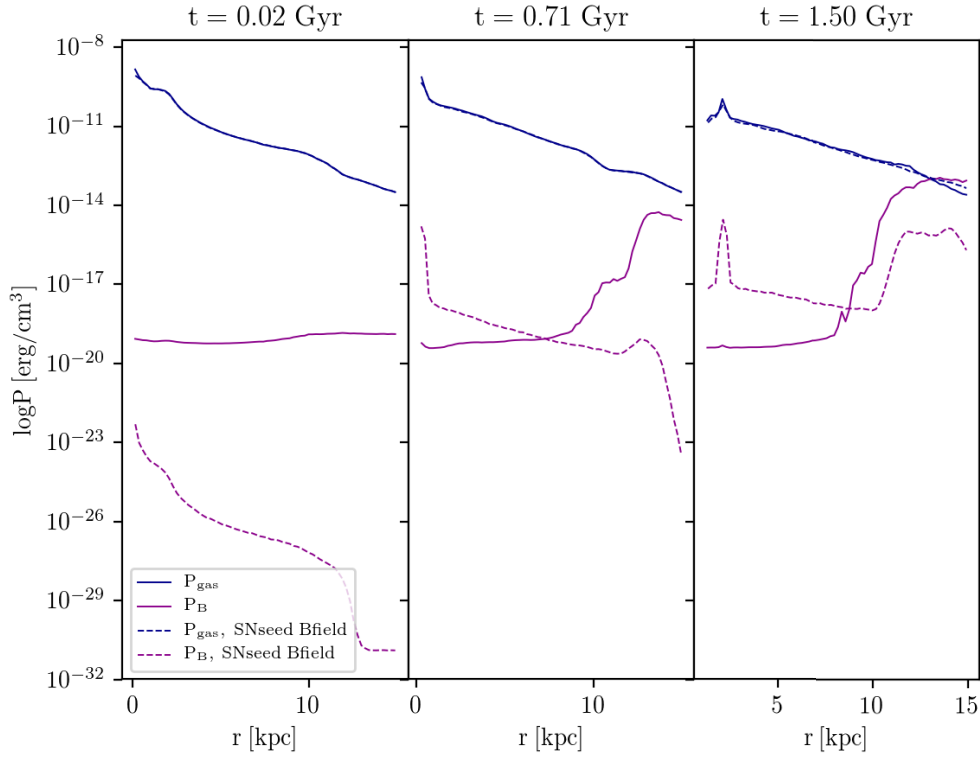
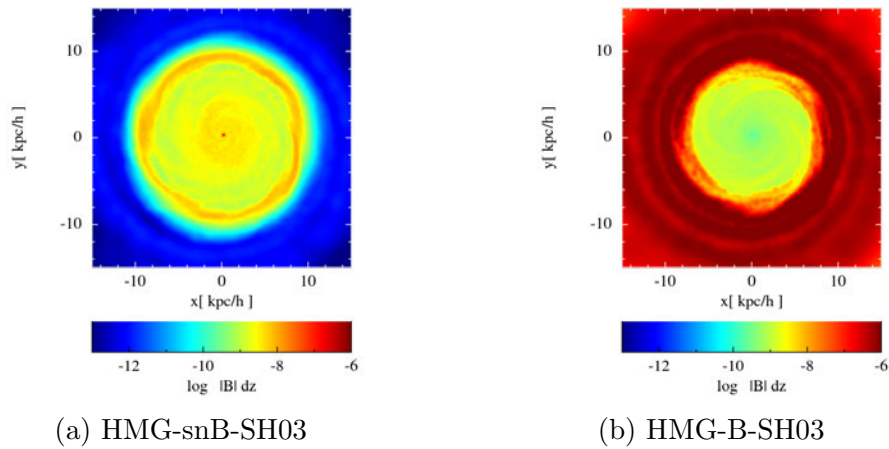


Figure 3.7: Pressure radial profiles at different times for the simulation with primordial magnetic field (solid lines) and with the supernova seeding model (dashed lines). In blue the thermal gas pressure is shown while in magenta is shown the magnetic pressure.



(a) HMG-snB-SH03

(b) HMG-B-SH03

Figure 3.8: High mass galaxy (HMG-SH03) at 1 Gyr with different magnetic field models. The panel (a) shows the face on projection of the galaxy with supernova seeded magnetic field. The panel (b) shows the face on projection of the galaxy with primordial magnetic field. The color bar shows the integrated magnetic field strength over the z (vertical) direction.

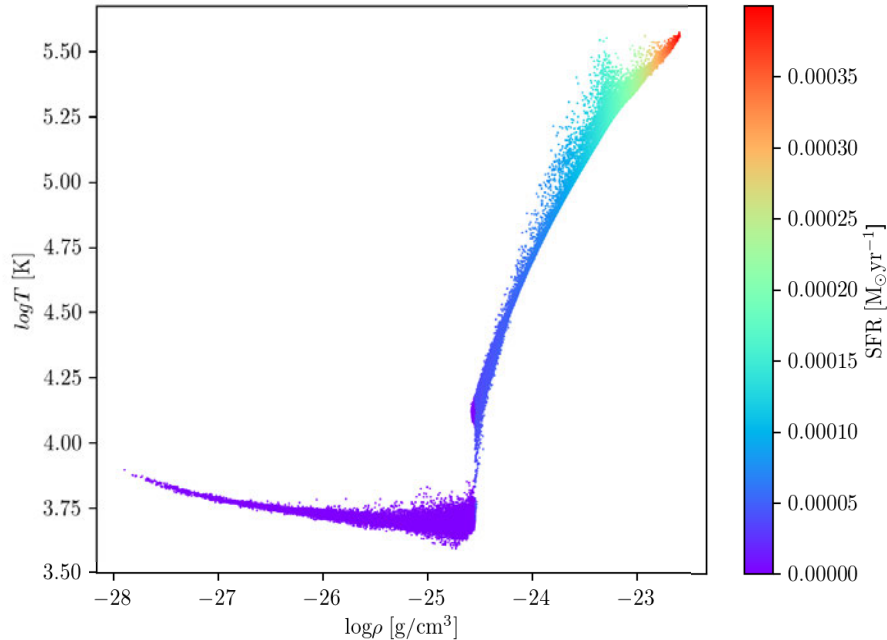


Figure 3.9: Phase diagram of the high mass galaxy (HMG-B) with magnetic fields and the new star formation model at $t = 0.01$ Gyr. The color code shows the star formation rate that corresponds to each particle.

3.2.3 Results: Galaxy with the new, pressure based, star formation model

In order to test the new star formation model (section 2.3), we use the same galaxy setup for the initial conditions, as in section 3.2.2. We test different magnetic field configurations, i.e. no magnetic field (noB), primordial magnetic field (B) and supernova seeded magnetic field (snB). Thus for the high mass galaxy (HMG), which is a milky way type galaxy we follow the name conventions: HMG-noB, HMG-B and HMG-snB for each of the aforementioned magnetic field configurations.

Since the equilibrium solution that described the evolution of the hot phase remains the same, we do not expect a significant difference in the phase diagram that results from a simulation with the new star formation model. Indeed, in figure 3.9 the effective temperature as a function of the gas density is shown. The color code indicates the star formation rate per particle. The density threshold calculation has changed but its value barely changed. In the beginning of the galaxy evolution, when the magnetic field is low or absent the molecular fraction is not very significant in the regulation of the star formation, since the thermal gas pressure does not appear to change significantly during time as is shown in figure 3.10. However, the molecular fraction makes the stars form from the molecular gas of the interstellar medium and not only from just the cold gas. The importance of this

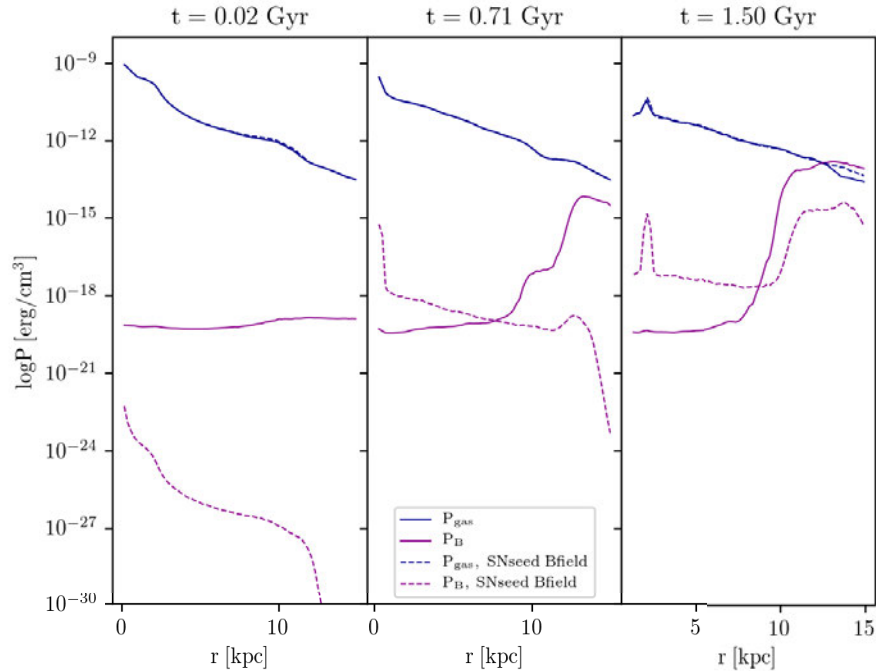


Figure 3.10: Thermal and magnetic pressure as a function of the galactic radius. The thermal (blue) and magnetic (magenta) are shown for the 2 different magnetic field models, i.e. the solid lines are from the high mass galaxy with primordial magnetic field and the dashed lines are from the high mass galaxy simulation with supernova seeded magnetic field.

change will be obvious when the magnetic fields are amplified enough in order to provide a magnetic pressure comparable or higher than the thermal pressure. When this happens it is essential to include the magnetic pressure in the star formation prescription. For this set up, as is shown in figure 3.10 the magnetic fields are amplified sufficiently only on the outer part of the galaxy in the case of the HMG-B, in which we initiate the magnetic field as $\mathbf{B} = (B_0, 0, 0)$ with $B_0 = 10^{-9}$ G. Face on cross sections of the magnetic field structure from the two simulations, HMG-B and HMG-snB, are shown in figure 3.11. In the left panel, the simulation with the supernova seeded magnetic field is shown. By the time of 1 Gyr many stars have died as supernova which act as the magnetic field seed to the galactic disk. As the star formation rate is higher in the center of the galaxy, the magnetic field strength is higher in the central region of the galaxy. Also, the magnetic field is easier amplified in the outer regions of the galaxy due to the $\alpha - \Omega$ dynamo, which is more efficient in regions with high rotation, i.e. the outer part of the galaxy. In the case of the primordial magnetic field, right panel of figure 3.11, we notice the same configuration of the magnetic field as in the case of SH03. As was already explained, this is mainly a numerical effect because of the boundary conditions of the galactic disk.

In figure 3.12 the star formation rate as a function of the galactic radius is shown. It is worth noticing that from the beginning (0.02 Gyr) the star formation is higher in the cases

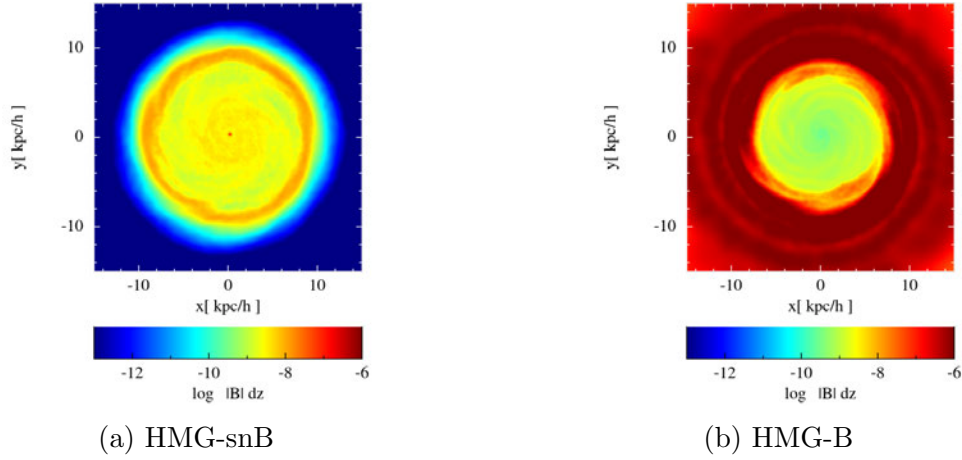


Figure 3.11: High mass galaxy, with the new star formation model, at 1 Gyr with different magnetic field models. The panel (a) shows the face on projection of the galaxy with supernova seeded magnetic field. The panel (b) shows the face on projection of the galaxy with primordial magnetic field. The color bar shows the integrated magnetic field strength (in gauss) over the z (vertical) direction.

with MHD calculations (HMG-snB and HMG-B) comparing with the simulation without magnetic fields (HMG-noB). Moreover, comparing to figure 3.5, the new star formation model appears more bursty throughout the galaxy at earlier times in the case of the MHD simulations. This is also obvious from figure 3.13, in which the projected galaxy is shown at 1 Gyr with color coded by the star formation rate. Between the MHD simulation and the non-MHD simulation we notice that in the latter case the disk appears smoother and with lower star formation rate. In general, the new star formation model creates a structured disk with spiral arms and active star formation that follows the spiral structure of the disk. In figure 3.14 the surface density of different components of the gas in the interstellar medium is shown for the simulations with primordial magnetic field (solid lines) and for the simulation with the magnetic seeding model (dashed lines). The cold gas is calculated for every particle as the root of equation (2.73) and the molecular fraction is dependent only on the total pressure of the gas at every position and is calculated from equation (2.53). The gas density is high in the center of the galaxy and decays in the outer parts of the galaxy. Despite the change in the magnetic pressure as shown in figure 3.10, the molecular fraction does not change behaviour significantly since the thermal pressure is dominant and is stably decaying with the galactic radius. The aforementioned behavior is also reflected in the radial profile of the star formation rate as presented in figure 3.12. The total star formation rate as a function of time is presented in figure 3.15. In the beginning of the galactic evolution the star formation is very high because of the initial condition set up. The galaxy is initiated with a lot of gas and already formed stars. There is a great amount of cold gas in the initial conditions with density higher than the density threshold that gives the first peak in the star formation rate. The feedback from this excessive process is responsible for the dip right after. Then, after the second broader peak, the self-regulated star formation regime is operating. The rate of star formation drops gradually and after

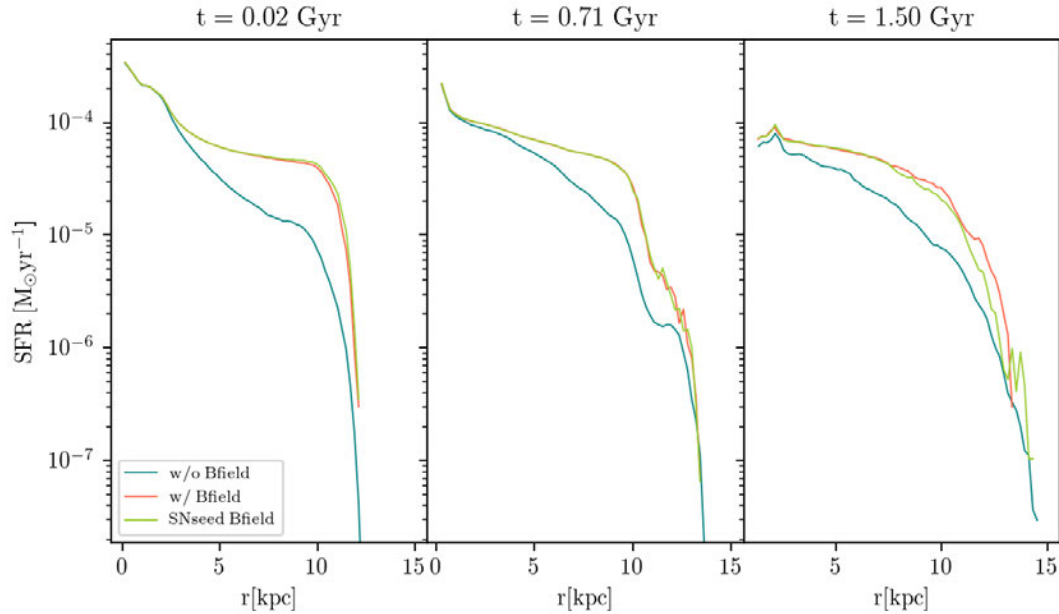


Figure 3.12: Radial profile of the star formation rate of the high mass galaxy (HMG). The different colors correspond to different magnetic field models, with no magnetic field (light blue), primordial magnetic field (orange) and supernova seeded magnetic field (green).

approximately 2 Gyr is much lower than $1 \text{ M}_{\odot} \text{ yr}^{-1}$. This happens since at that timescale the star formation has consumed the gas reservoir of the galaxy and does not receive any inflowing gas from the galactic environment neither undergoes interactions with other galaxies.

Another interesting fact of this star formation model is that galaxies with different masses still follow the Schmidt-Kennicutt relation without the further tuning of parameters. This is obvious from figure 3.16, in which the result from different galaxy masses is shown compared to the observational relation. The observational Schmidt-Kennicutt relation [Schmidt, 1959, Kennicutt Jr, 1998] is a global property of galaxies that is widely observed and shows the efficiency of the star formation given the gas content of a galaxy. As was shown in section 2.3 the efficiency of the star formation or the timescale for the star formation are critical parameters that affect the consistency with the Schmidt-Kennicutt relation. Indication for change in this relation across redshift would imply the change in the star formation efficiency. In that case we should not try to fit the Schmidt-Kennicutt relation but rather reproduce its changes over time [Sharda et al., 2018] in the prescription of the sub-grid model.

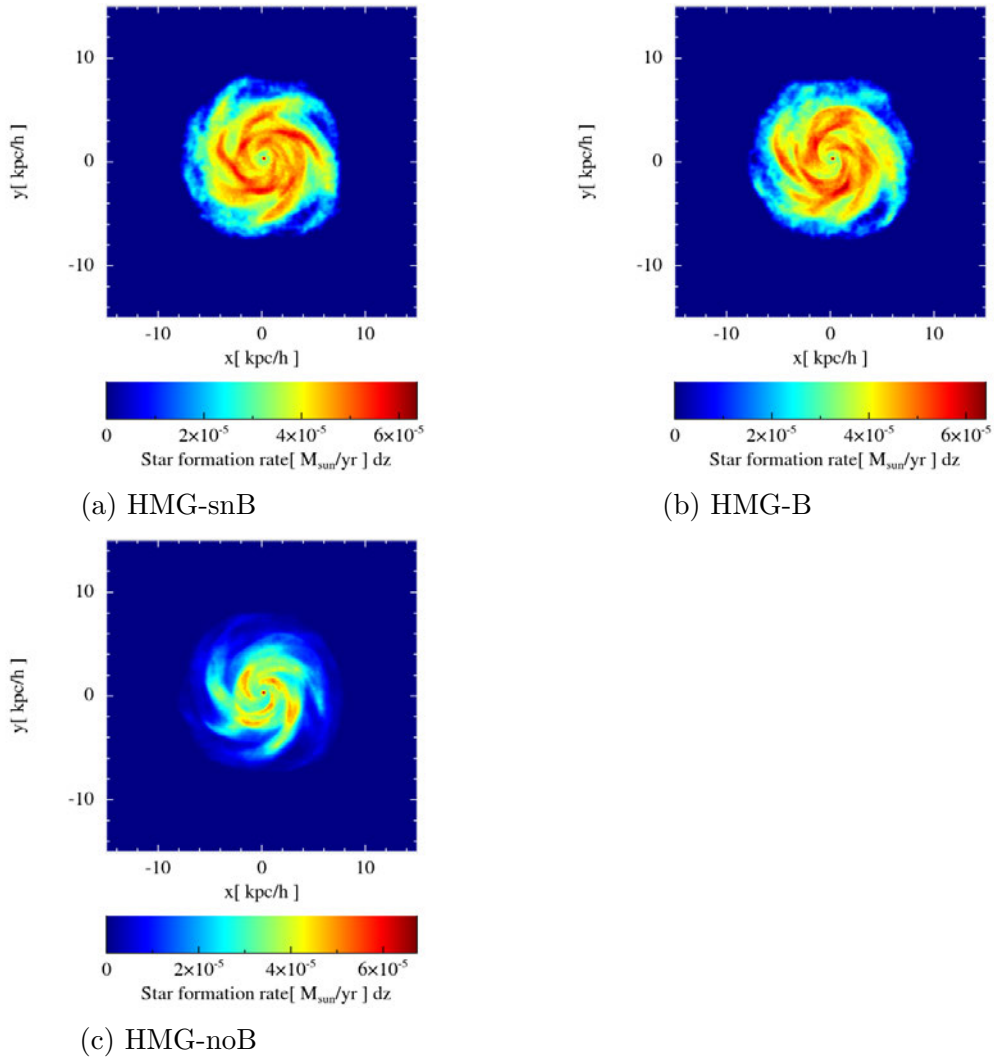


Figure 3.13: High mass galaxy, with the new star formation model, at 1 Gyr with different magnetic field models. The panel (a) shows the face on projection of the galaxy with supernova seeded magnetic field. The panel (b) shows the face on projection of the galaxy with primordial magnetic field and the panel (c) without magnetic field. The color bar shows the star formation rate integrated over the z (vertical) direction.

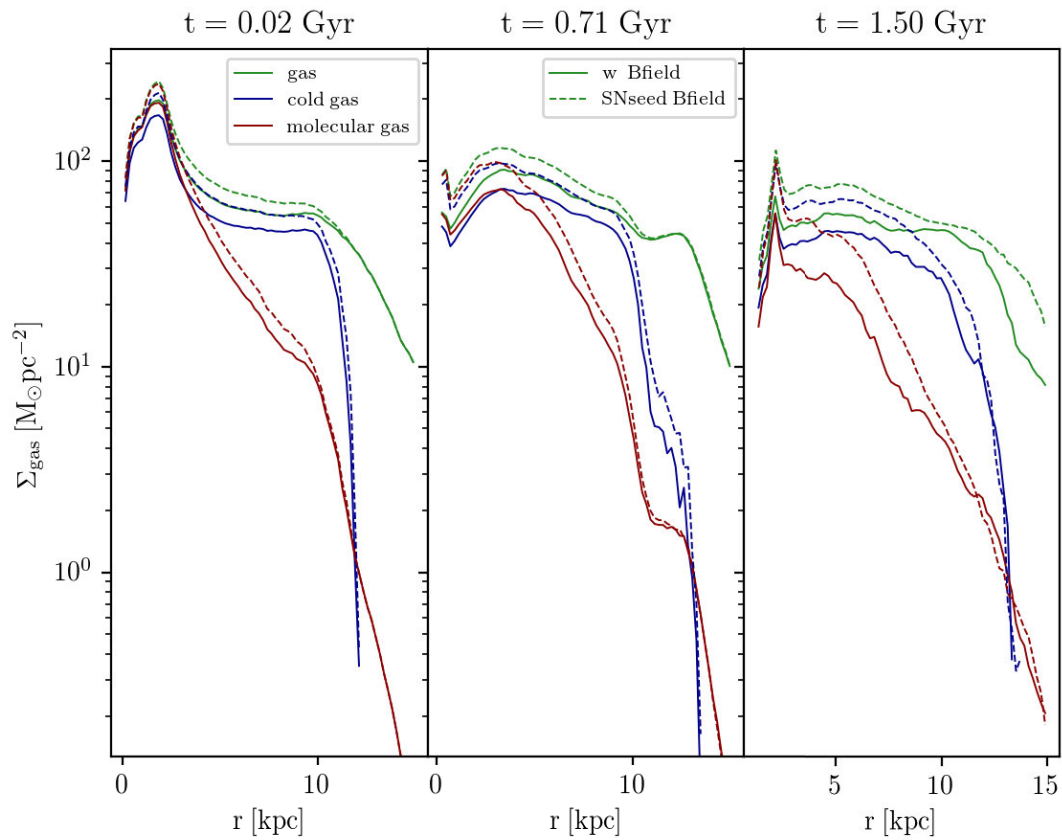


Figure 3.14: Surface density radial profiles of different components of the interstellar medium. The different colors show different components of the ISM with green to be the total gas, blue the cold gas, and red the molecular gas. The solid lines represent calculations from the HMG-B simulation while the dashed lines for the HMG-snB.

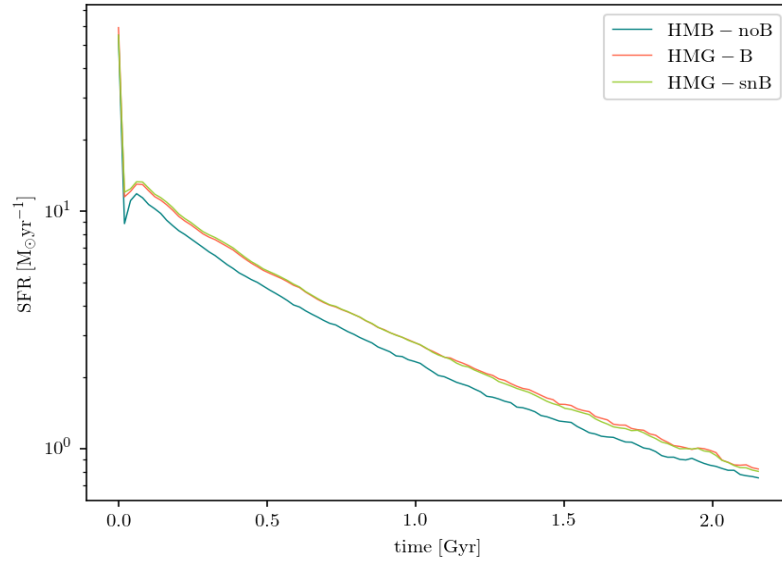


Figure 3.15: Star formation rate as a function of time for the set of simulations with the new star formation model. The simulations are performed for the high mass galaxy without magnetic fields (HMG-noB, light blue line), with primordial magnetic field (HMG-B, orange line), and with the supernova seeding model (HMG-snB, light green).

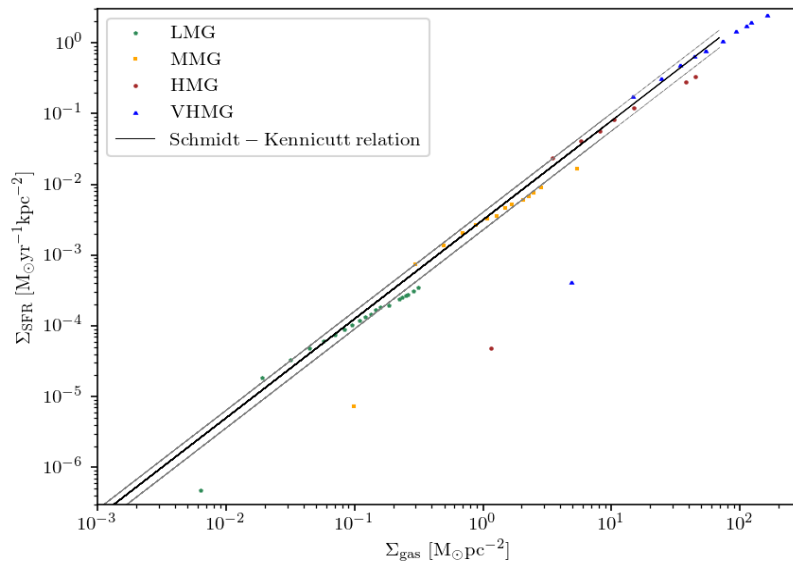


Figure 3.16: Schmidt Kennicutt relation for galaxy simulations with different masses. In solid line the observational Schmidt Kennicutt relation its shown and the grey lines are the errors (equation (2.22)). The different galaxies have total mass : LMG - $M = 10^{10} M_{\odot}$, MMG - $M = 10^{11} M_{\odot}$, HMG - $M = 10^{12} M_{\odot}$ and VHMG - $M = 10^{13} M_{\odot}$.

3.3 Simulations of an idealized disk galaxy with a gas halo

In order to study a more realistic galaxy scenario we should include a realistic environment around it. Apart from the dark matter halo that is already present in the previous set of simulations, we add a hot gas halo as the circum-galactic medium of the galaxy. For these systems we use the initial conditions as described in [Steinwandel *et al.* 2018 (in prep.)].

3.3.1 Numerical set up

For the set up of the galactic system we use the same disk galaxy as in the previous set of the simulations, following [Hernquist, 1993]. The dark matter halo of the galaxy follows a Hernquist density profile while the stellar and gaseous disk follow an exponential profile. The gas halo is initiated with a spherical symmetric density distribution and is especially chosen to be a β profile [Cavaliere and Fusco-Femiano, 1978], which is given by

$$\rho_{\text{gas}} = \rho_0 \left(1 + \frac{r^2}{r_c^2}\right)^{-3\beta/2} \quad (3.7)$$

The parameter β is chosen to be $\beta = 2/3$, the central gas density $\rho_0 = 5 \cdot 10^{-26} \text{ g} \cdot \text{cm}^{-3}$, a value that is motivated from cosmological simulations [Dolag *et al.*, 2015] but also from observations [Miller and Bregman, 2013]. Last, the core radius is set to $r_c = 0.22 \text{ kpc}$ in accordance with observations [Miller and Bregman, 2013] and simulations [Moster *et al.*, 2010]. Assuming hydrostatic equilibrium for the gas halo, the temperature profile, according to [Steinwandel *et al.* 2018 (in prep.)] is given from

$$T(r) = G \frac{\mu m_p}{k} \left(1 + \frac{r^2}{r_c^2}\right) [M_{\text{DM}} F_0(r) + 4\pi r_c^3 \rho_0 F_1(r)] \quad (3.8)$$

with μ the mean molecular weight, m_p the proton mass and k the Boltzmann constant. The functions $F_{0,1}(r)$ are given from

$$F_0(r) = \frac{r_c}{\alpha^2 + r_c^2} \left[\frac{\pi}{2} (\alpha^2 - r_c^2) + r_c \frac{\alpha^2 + r_c^2}{\alpha + r} - (\alpha^2 - r_c^2) \arctan\left(\frac{r}{r_c}\right) - r_c \alpha \ln\left(\frac{(\alpha + r)^2}{r^2 + r_c^2}\right) \right] \quad (3.9)$$

and

$$F_1(r) = \frac{\pi^2}{8r_c} - \frac{\arctan^2(r/r_c)}{2r_c} - \frac{\arctan(r/r_c)}{r} \quad (3.10)$$

In the table 3.5 parameters of the gas halo model are summarized, which remain constant for all the simulations with the gas halo. Having the gas halo and the galactic disk, we need to combine them in order to build the galactic system that we will simulate. To do so, a part of the central region of the gas halo is removed and the galactic disk is placed in the same position. This is done to prevent the overlap of the gas particles of the disk and

Table 3.5: Parameters for the gas halo

Parameters			
central density	ρ_0	$5 \cdot 10^{-26}$	$\text{g} \cdot \text{cm}^{-3}$
core radius	r_c	0.22	kpc
exponent	β	2/3	

Table 3.6: Parameters for the systems with disk galaxy and gas halo

Disk Parameters		LMG	MMG	HMG
Total mass [$10^{10} M_\odot$]	M_{200}	1	10	100
Virial radius	r_{200}	31	67	145
Halo concentration	c	8	10	12
Spin parameter	λ	0.033	0.033	0.033
Disk spin fraction	j_d	0.041	0.041	0.041
Disk mass fraction	m_d	0.041	0.041	0.041
Bulge mass fraction	m_b	0.013	0.013	0.013
Disk scale length [kpc]	l_d	2.1	1.5	0.8
Disk height [l_d]	z_0	0.2	0.2	0.2
Bulge size [l_d]	l_b	0.2	0.2	0.2
Gas halo mass [$10^{10} M_\odot$]	$M_{\text{gas halo}}$	0.05	0.5	5.0
Temperature [K]	T_{vir}	10^4	10^5	10^6

the halo since they have different properties. Therefore, a disk galaxy with circumgalactic medium is created, which is a realistic environment in order to test the new star formation model and the effect of the magnetic fields.

With this set up we run galactic systems with different masses and different magnetic field models. Here we chose the mass of the galactic disk to vary from $10^{10} M_\odot$ (low mass galaxy, LMG), to $10^{11} M_\odot$ (medium mass galaxy, MMG) and $10^{12} M_\odot$ (high mass galaxy, HMG). Again, we add an ending for each name according to the magnetic field model that we used, i.e., B for primordial magnetic field, snB for supernova seeded magnetic field and noB for no magnetic field. The parameters for these systems are shown in table 3.6. In the following we will focus on the analysis of the Milky Way type galaxy (HMG), while results from the different systems can be found in Appendix.

3.3.2 Results

Here we will present the results of the Milky way type galaxy with 2 magnetic field models, i.e., with primordial magnetic field of strength $B = 10^{-9}$ G in the \mathbf{x} direction (halo-HMG-B)² and magnetic field seeded from supernova explosions (halo-HMG-snB). The advantage

²Here we add the prefix *halo* to remind the presence of the circum-galactic medium and to differentiate from the previous set of simulations.

of having a gas halo surrounding the galactic disk is the opportunity to study the properties of the evolution of the and especially in our case the interplay of magnetic fields and star formation in a realistic astrophysical environment without any perturbations.

Before looking the structure of the galaxy and its properties it is interesting to comment on the temperature-density phase diagram for the new star formation model in two different times. In figure 3.17 the effective temperature of the gas as a function of the gas density is shown at $t = 0.01$ Gyr color coded by the star formation rate per particle, while in figure 3.18 the same plot is shown at $t = 1$ Gyr. In figure 3.17 there are two different component that correspond to the particles of the gas halo (upper group of particles) and the galactic disk (lower group of particles). Since we are still using a density threshold to distinguish star forming and non star forming particles the 2 branches of particles are differentiated by color code, which shows the star formation rate per particle. Particles plotted in purple have densities lower than the density threshold, while the rest of the particles follow the new multiphase model. From figure 3.17 the interaction of the galactic disk with the hot halo is also obvious. A part of the hot gas halo cools and falls towards the galactic disk, an effect that is more obvious and strong after 1 Gyr of the evolution of the system as shown in figure 3.18. In the last plot star forming particles are flowing towards the hot halo, indicating the bubbling behavior of the gas of the galaxy while interacting with the gas of the halo. There are some particles that have high temperatures but are not star-forming. These are probably particles that were heated by following the evolution of the multiphase model but gained low densities and therefore exited the multiphase model. It is important to keep in mind that the temperature shown in these plots is the effective temperature of the total gas (temperature that corresponds to equation (2.66)) which converges to the temperature of the hot phase in the star formation branch since the cold clouds are kept to a constant temperature of $T_c = 10^3$ K which is usually much lower than the temperature of the hot gas.

General properties of the galaxy

In order to study the structure of the galaxy and where the star formation is taking place we present the galactic disk in face on projection for the two different magnetic field models, i.e. halo-HMG-B and halo-HMG-snB in three different points in time, i.e. after 1 Gyr, 2 Gyr and 3 Gyr of evolution. The star formation follows the spiral structure of the galactic disk with higher star formation rate in the center and in some parts of the spiral arms. Comparing figure 3.19a and figure 3.19b, which show the galaxies halo-HMG-snB and halo-HMG-B respectively, the morphological differences are negligible. These are becoming more obvious in the later evolution as shown in figure 3.20b and figure 3.20a. Comparing these figures with the same figures of the isolated galaxy (figure 3.13) it is clear that the presence of the circum-galactic medium allows the edges of the galaxy to be smoother and suppress numerical effects that can arise from the absence of SPH particles around the galaxy. Moreover, following the evolution of the disk we notice instabilities that arise on its edges. This happens because the galaxy rotates much faster comparing wit the hot gas halo. After 3 Gyr of evolution the spiral structure is not so strong. At this point the galaxy has lost a part of its gas mass in the form of an outflow that we will further explain later.

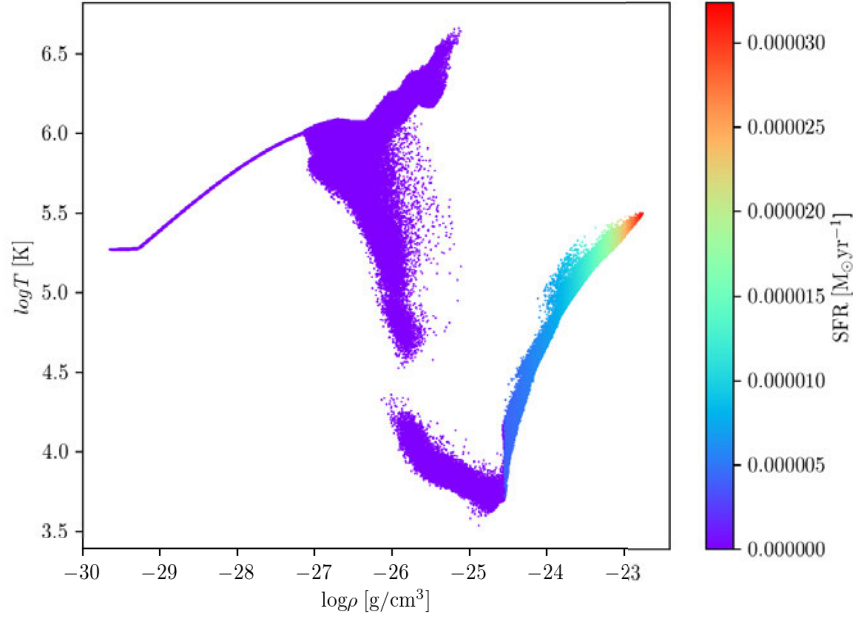


Figure 3.17: Temperature-density diagram for the halo-HMG-B system at $t = 0.01$ Gyr. The upper group of particles corresponds to the particles of the gas halo while the down part corresponds to the gas particles of the galaxy

In figure 3.22 the radial profiles of the galaxies halo-HMG-B and halo-HMG-snB are shown. Here the slight different behavior of the star formation across the galaxy for the 2 different magnetic field models is better visible, with the SN seeding model having more fluctuations. In figure 3.23 the mean thermal and magnetic pressure, calculated in radial bins of the galactic radii, are shown at $\sim 0.5, 1.5, 2.5$ Gyr. The thermal gas pressure decreases with the galactic radius since the gas density is decreasing as well. The magnetic pressure in the case of primordial magnetic field (halo-HMB-B, solid magenta line) starts from a relatively constant value with local amplifications probably due to the small scale turbulent dynamo which is produced from supernova feedback and gas motions. At later times the magnetic pressure increases since the magnetic field is amplified. In the simulation with the supernova seeding (halo-HMG-snB) the magnetic pressure (dashed magenta line) is higher in the center of the galaxy because of the higher star formation, which implies higher a supernova rate and therefore more magnetic field seeding. After 1 Gyr that the magnetic fields are further amplified, the magnetic pressure is higher through the whole galactic disk. An interesting feature appears in the gas pressure, both thermal and magnetic, at ~ 2.4 Gyr. This peak in approximately radii of 4 – 5 kpc is consistently reflected in the star formation rate in figure 3.22 and the gas density in figure 3.24. It seems that this peak is correlated with a magnetic driven outflow that we observe in the galaxy and we will further discuss later.

The star formation rate as a function of time is shown in figure 3.26. As was already

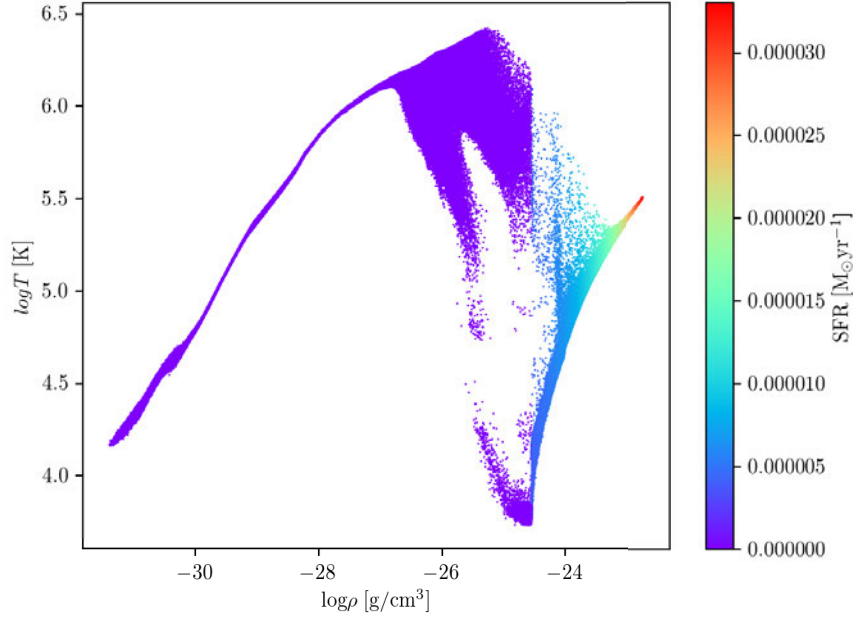


Figure 3.18: Temperature-density diagram for the halo-HMG-B system at $t = 1$ Gyr. The colorbar shows the star formation rate per particle.

discussed in the section 3.2.3 in the case of an isolated galaxy, the onset of star formation outputs a high star formation rate and the self-regulated model is set after the second, lower, peak of the star formation rate. Here the effect of the hot gas halo on the support for the star formation is obvious as it provides support for the star formation process. The cooling inflowing gas from the halo to the galaxy provides more fuel for the star formation and settles the star formation rate to be around $\sim 1 M_{\odot} \text{yr}^{-1}$ which is in accordance with the observed values for the Milky Way [Robitaille and Whitney, 2010]. The break that we notice for the halo-HMG-B simulation is due to the magnetic outflow that happens at this point. This phenomenon drives out of the galaxy a small amount of gas which results in the drop of the star formation rate.

To further continue the discussion of the simulations with the new star formation model we will study how the magnetic fields are evolving in the system. In figure 3.28 the galaxy in face on and edge on slices for the 2 simulations, namely halo-HMG-snB and halo-HMG-B at 1 Gyr are presented. The same plots at 2 Gyr are shown in figure 3.29 and at 3Gyr at figure 3.30. A nice structure of the magnetic field strength is shown in the galactic disk which is amplified in observable strengths. The observable mean values for magnetic field strengths reach the order of $\sim \mu G$ (i.e., [Chyży et al., 2007]). This is the case for these simulations as well, since the mean magnetic field reaches $\sim \mu G$ values, as shown in the growth rate of the mean magnetic field in figure 3.25, which agrees with the simulations using SH03 as presented by [Steinwandel *et al.* 2018 (in prep.)]. Our

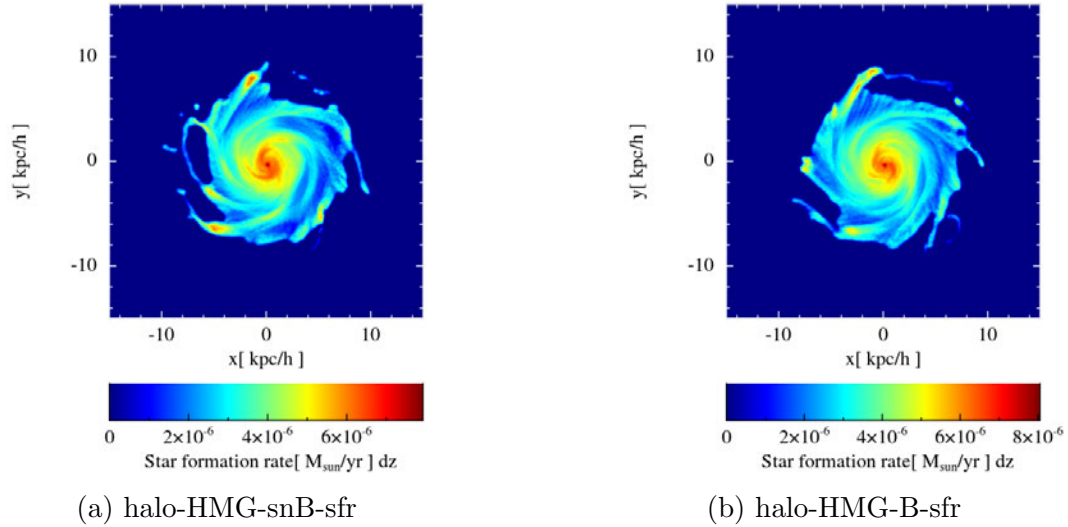


Figure 3.19: High mass galaxy with gas halo (halo-HMG) projection at $t = 1$ Gyr for the simulation with the supernova seeded magnetic field. The color code in the plots is the star formation rate integrated along the z direction.

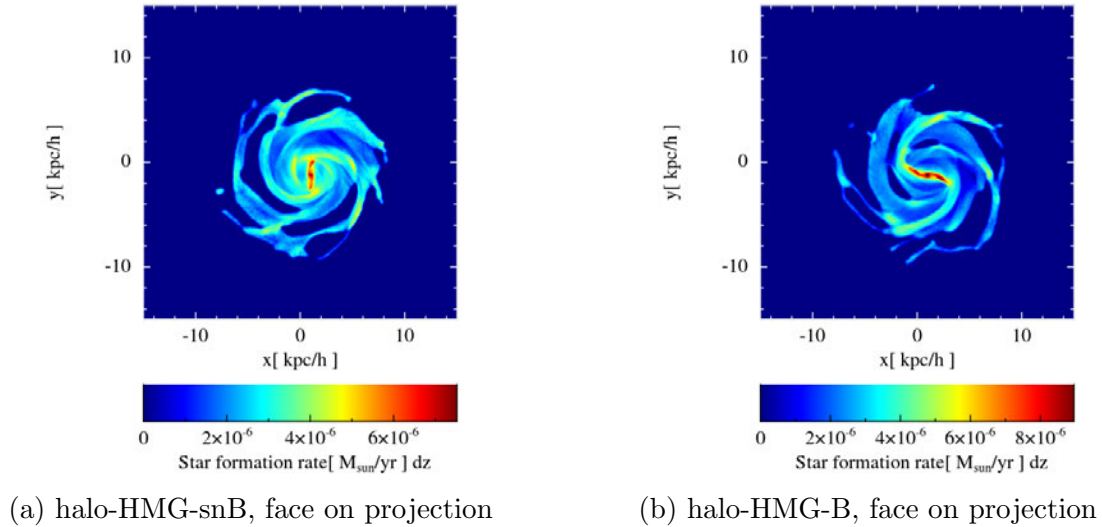


Figure 3.20: High mass galaxy with gas halo (halo-HMG) projection at $t = 2$ Gyr. The left panel shows a projection of the galactic disk for the simulation with the supernova seeded magnetic field. The right panel show the projected disk of the simulation with the primordial magnetic field. The color code in all plots is the star formation rate integrated along the z direction.

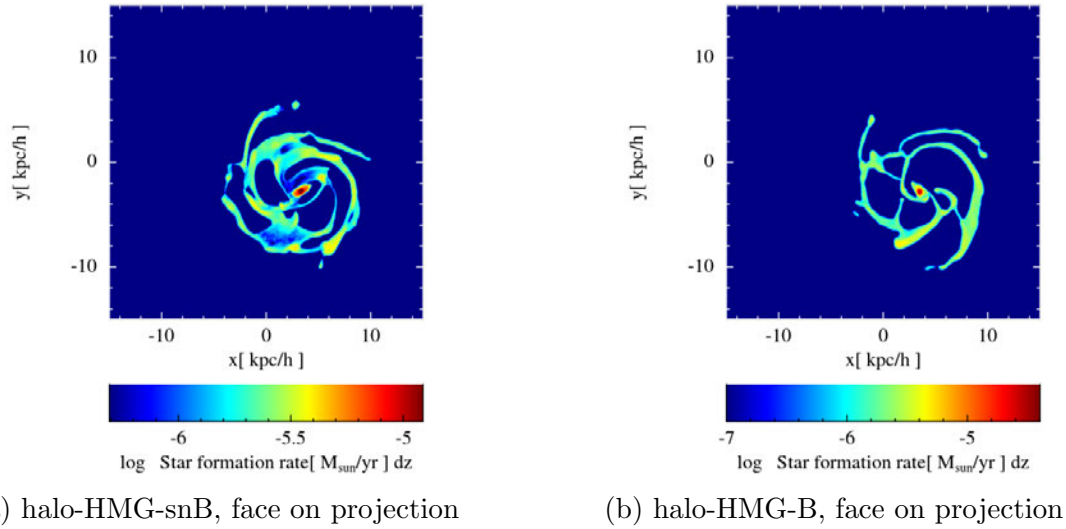


Figure 3.21: High mass galaxy with gas halo (halo-HMG) projection at $t = 3$ Gyr. The left panel shows a projection of the galactic disk for the simulation with the supernova seeded magnetic field. The right panel show the projected disk of the simulation with the primordial magnetic field. The color code in all plots is the star formation rate integrated along the z direction.

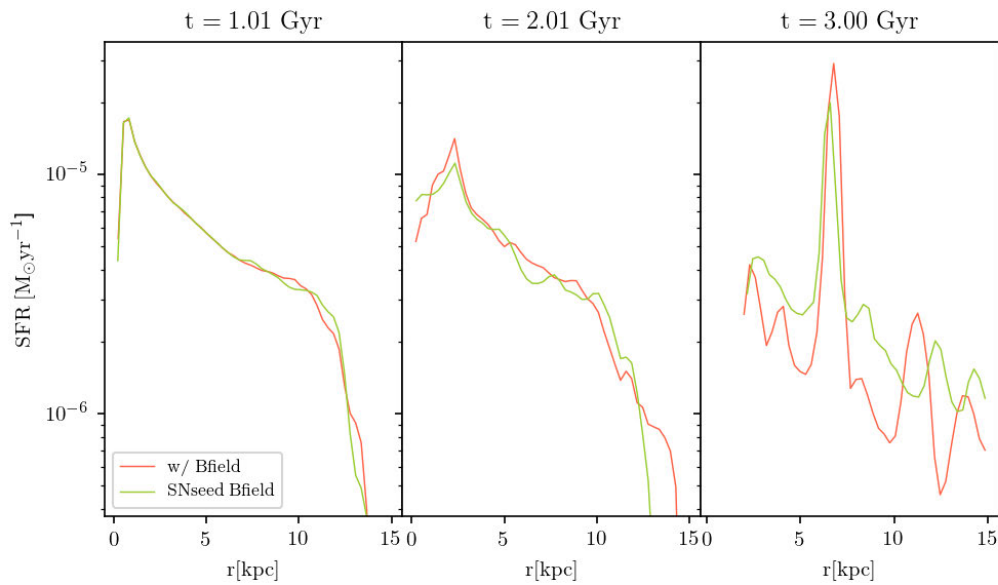


Figure 3.22: Star formation rate calculated in radial bins of the galactic radius. In orange is plotted the result from the halo-HMG-B and with light green from the halo-HMG-snB.

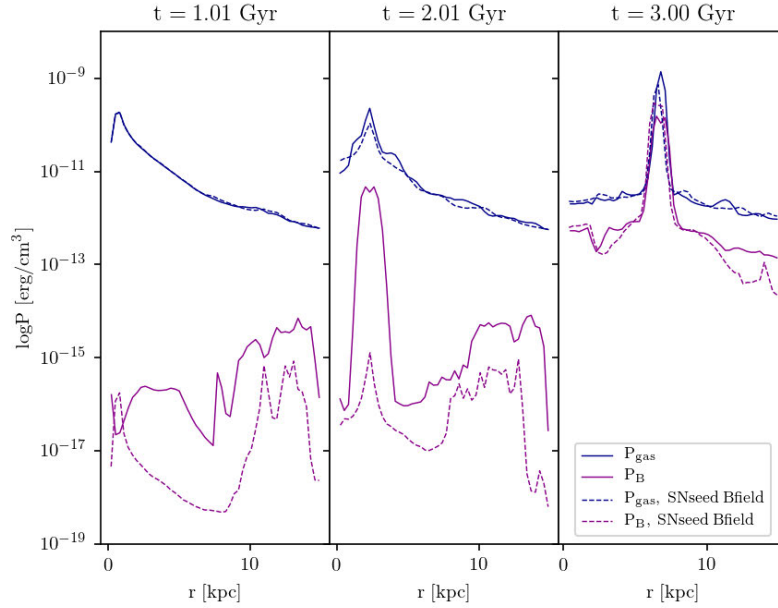


Figure 3.23: Mean pressure calculated in radial bins of the galactic radius in 3 different points in time. The dark blue lines show the thermal gas pressure while the magenta lines show the magnetic pressure. The solid lines are calculations from the halo-HMG-B simulation and the dashes lines are results from the simulation halo-HMG-snB.

results for this set of simulations are very different from the results of the isolated disk as shown in figure 3.11b. Here is once again obvious the importance of the circum-galactic medium. In the case of the isolated galaxy, we have already discussed the non-physical high magnetic field in the outer parts of the galaxy due to the boundary conditions. When we add the gas halo, the galactic disk has realistic boundary conditions and the amplification of the magnetic field occurs normally. For both models, with primordial magnetic field and with the supernova seeded magnetic field (figure 3.28, figure 3.29) we notice an obvious magnetic structure with higher magnetic field in the center of the galaxy and in the outer parts of the disk. For the simulation halo-HMG-B the magnetic field is probably amplified in the center due to the small scale turbulent dynamo. However, to test this claim about the turbulent nature of the magnetic field amplification we produce the power spectra for the simulation with the primordial magnetic and the supernova seeded magnetic field. The power spectra were produced with the tool SPHMAPPY ([Röttgers and Arth, 2018]) which bins the SPH data on a grid using the desired kernel, which is the Wendland C4 in our simulations. In figure 3.27a the power spectrum for the halo-HMG-snB simulation is shown in different points in time, while figure 3.27b shows the power spectrum for the halo-HMG-B simulation. From theory we expect a power spectrum with slope of $3/2$ in early times [Kazantsev et al., 1985] and slope of $-3/2$ in the later evolution of the galaxy [Iroshnikov, 1963]. We would not make a strong claim that the magnetic fields are amplified efficiently through small scale turbulent dynamo for the case of primordial magnetic field

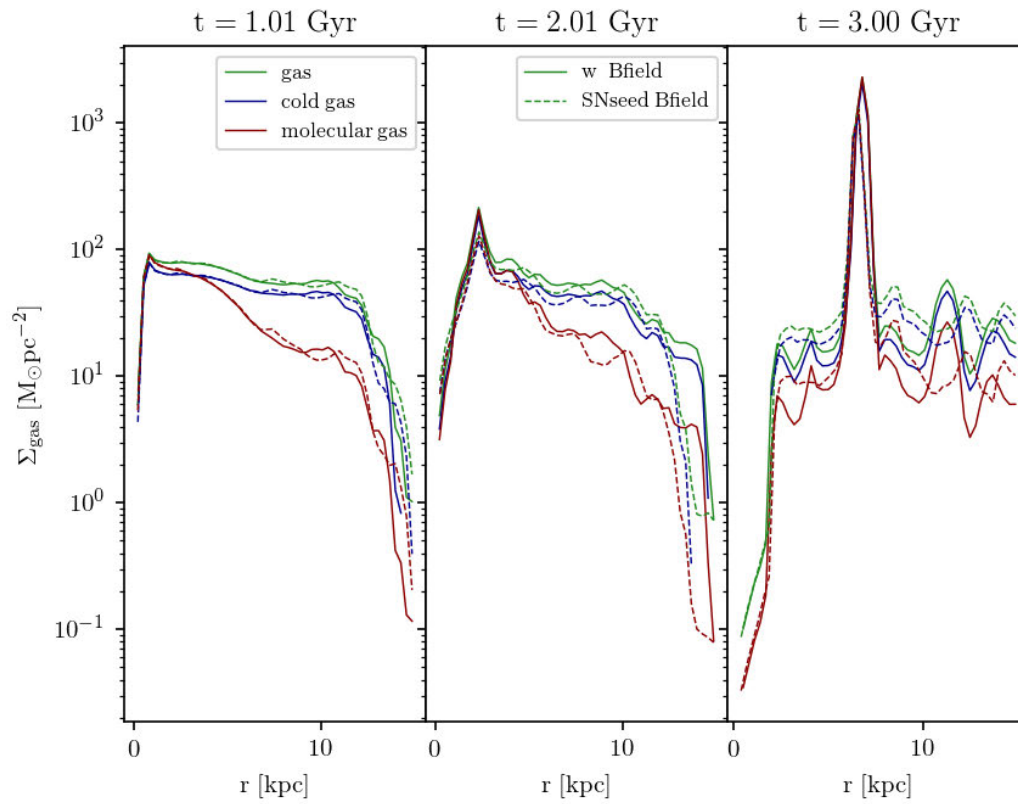


Figure 3.24: Radial profiles of the surface density for different components of the ISM. The mean surface density of the total gas (green), the cold gas (blue) and the molecular fraction (red) are shown as a function of the galactic radius. The solid lines correspond to the halo-HMG-B simulation and the dashed lines to the halo-HMB-snB simulation.

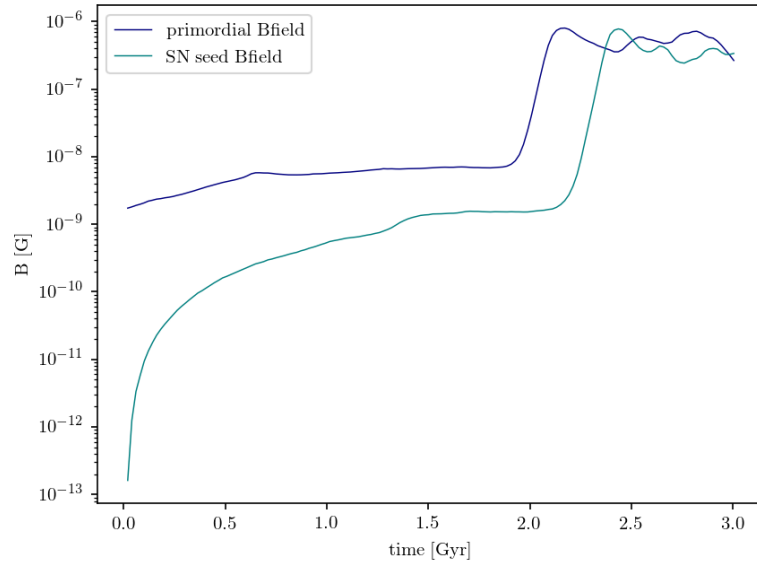


Figure 3.25: Mean magnetic field evolution with time. In dark blue is the result from the halo-HMG-B simulation while in light blue is the result from the halo-HMG-snB simulation.

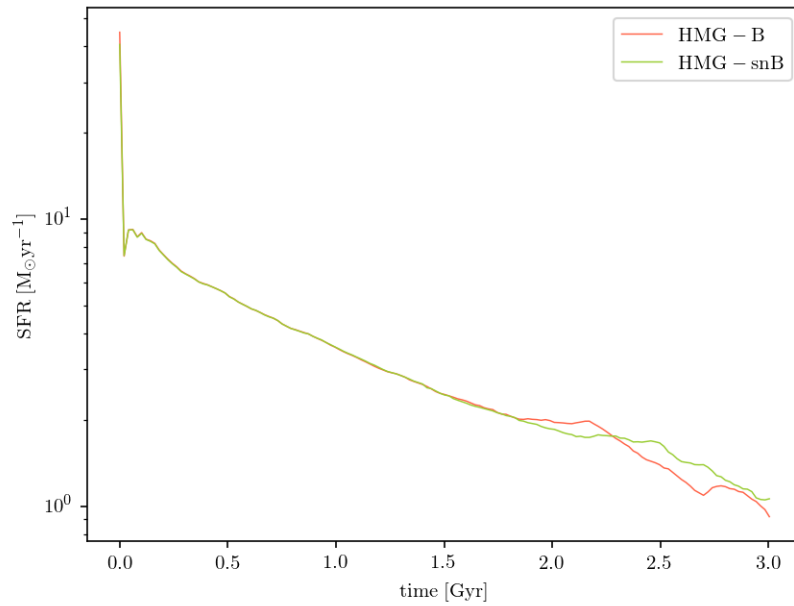


Figure 3.26: Star formation rate as a function of time. The star formation rate from the simulation with the primordial magnetic field is shown in light green, while the star formation rate of the simulation with the supernova seeding is shown in light orange.

since from figure 3.27b is not very clear. Furthermore, we have to keep in mind than in the case of primordial magnetic fields, our simulations did not show significant amplification of the magnetic field strength, especially before 2 Gyr (figure 3.25). In the case of the supernova seeded magnetic field, there is an evidence of small scale turbulence as it seems from the power spectrum of figure 3.27a. Overall the magnetic field shows better behavior in the case of supernova seeded field. In the edge of the galactic disk, many instabilities appear due to shear with the hot gas halo, which have different densities and velocities. This enhances the turbulence in this region and therefore the amplification of the magnetic field in the outer parts of the galaxy can be attributed to this feature in addition to the large scale $\alpha - \Omega$ dynamo due to the high rotational velocities in this part of the galaxy. The same processes apply for the simulation of halo-HMG-snB. The difference in the latter case is that we start with an un-magnetized disk and the first magnetic fields are connected to the star formation activity. The high star formation rate in the center of the galaxy results in a higher supernova rate which consequently seeds more magnetic dipoles in the disk. In general the magnetic field strength is shown to be more structured comparing to [Steinwandel *et al.* 2018 (in prep.)]. This is probably happening due to the different star formation models that are used. Steinwandel *et al.* 2018 (in prep.) use SH03 in contrast to the simulations presented here that are performed with the new pressure based star formation model. Even from the surface density of the gas is shown (figure 3.24) that the galactic disk does not have a smooth density distribution but rather a density distribution with small fluctuations. As shown from figure 3.25 the magnetic field is always higher in the case of the primordial magnetic field but the amplification mechanism seems more efficient in the case of the supernova seeded field. After 3 Gyr the magnetic fields show an outflow above and below the galaxy as is displayed in figure 3.30. The magnetic field structure is still obvious at the halo-HMG-snB simulation which in contrast to the halo-HMG-B case. The outflow that is observed starts earlier in the simulation with the primordial magnetic field (halo-HMG-B) and has grown in larger distances around the galaxy.

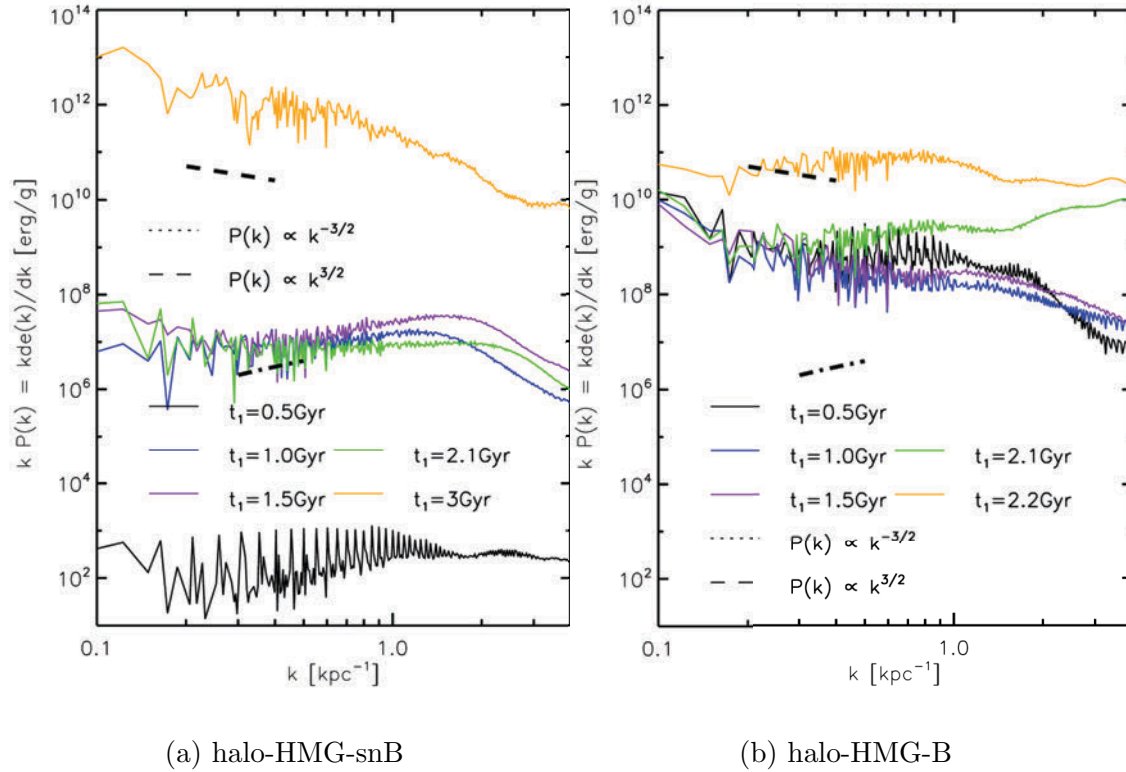
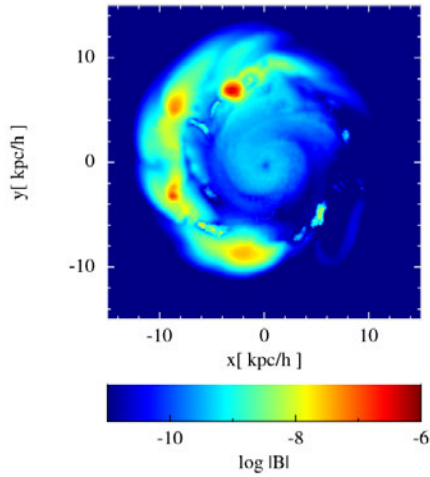
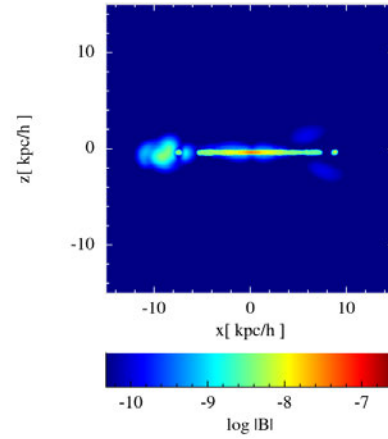


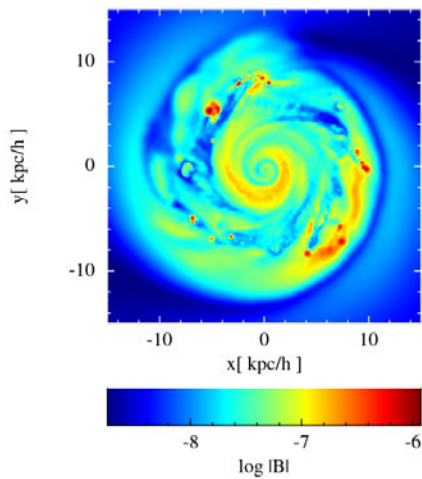
Figure 3.27: Magnetic power spectra for the simulations halo-HMG-snB (left) and halo-HMG-B (right) for different points in time as it is indicated in the legends. For early times the turbulent dynamo theory predicts $P(k) \propto k^{3/2}$ [Kazantsev et al., 1985] and at later times the small scale dynamo stops and the power spectra follows $P(k) \propto k^{-3/2}$ [Iroshnikov, 1963]. For the case of halo-HMG-snB the power spectrum seems to follow the expected slopes and we could claim that there is an evidence for the operation of turbulent dynamo in the disk. However this is not the case for the simulation. It is not clear if the power spectrum follows the Kazantsev slope in early times. This is in accordance to the rest of our results since in the case of halo-HMG-B we do not notice an efficient amplification of the magnetic field strength before 2 Gyr (figure 3.25).



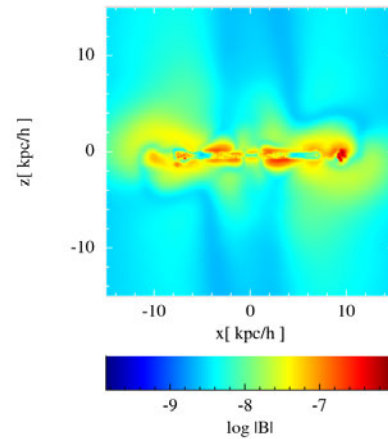
(a) halo-HMG-snB, face on slice



(b) halo-HMG-snB, edge on slice

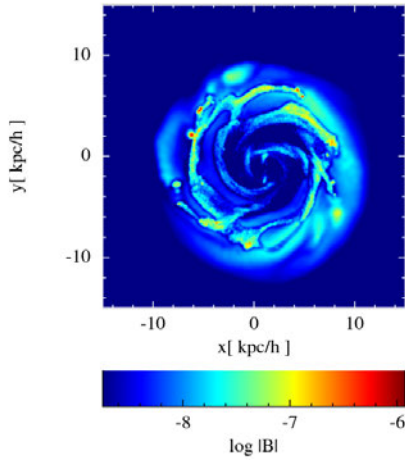


(c) halo-HMG-B, face on slice

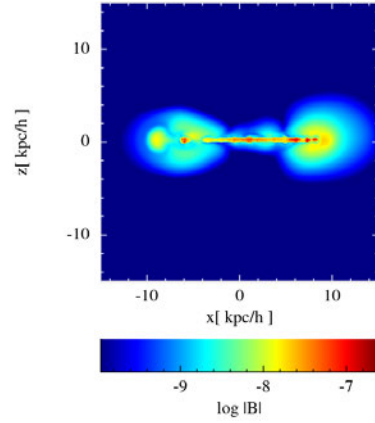


(d) halo-HMG-B, edge on slice

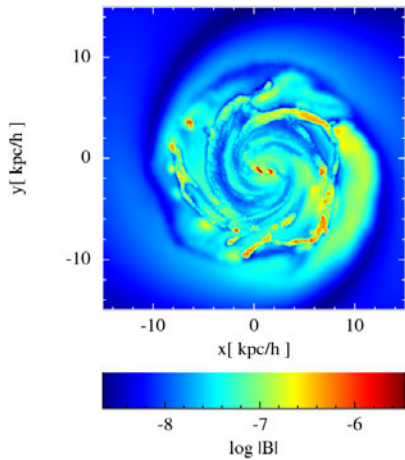
Figure 3.28: High mass galaxy with gas halo (halo-HMG) at $t = 1$ Gyr. The upper 2 panels show a slice of the simulation with the supernova seeded magnetic field. The lower 2 panels show a slice of the simulation with the primordial magnetic field. The color code shows the magnetic field strength in G and is unique for each of the subplots.



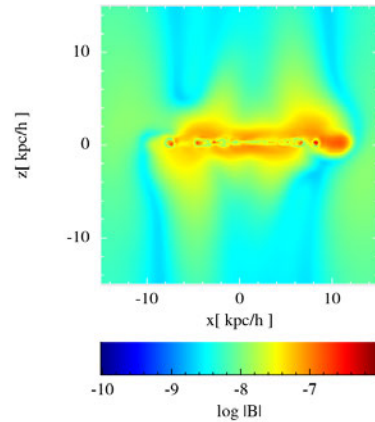
(a) halo-HMG-snB, face on slice



(b) halo-HMG-snB, edge on slice

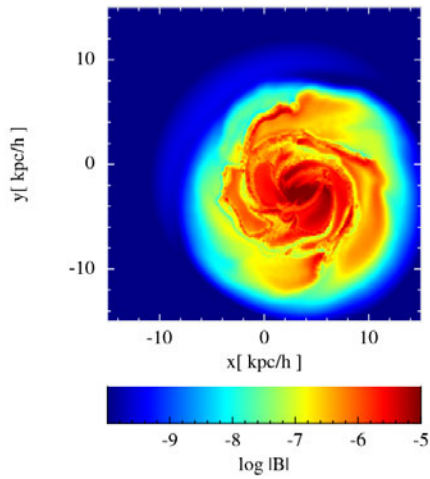


(c) halo-HMG-B, face on slice

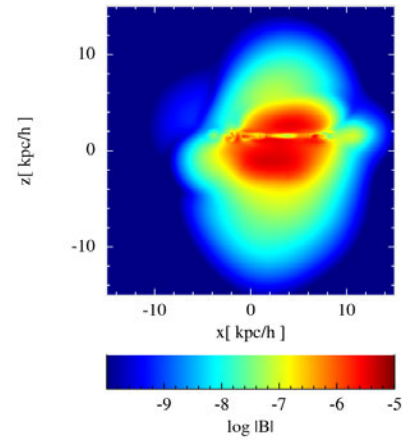


(d) halo-HMG-B, edge on slice

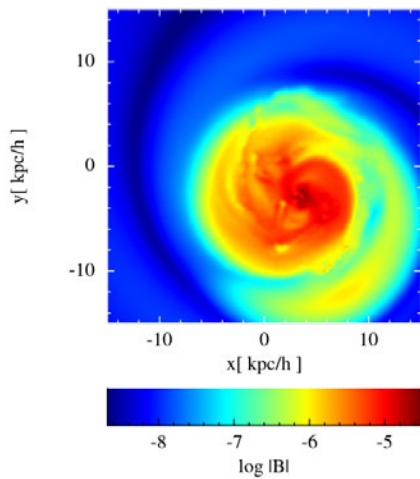
Figure 3.29: High mass galaxy with gas halo (halo-HMG) at $t = 2$ Gyr. The upper 2 panels show a slice of the simulation with the supernova magnetic seeded magnetic field. The lower 2 panels show a slice of the simulation with the primordial magnetic field. The color code shows the magnetic field strength in G and is unique for each of the subplots.



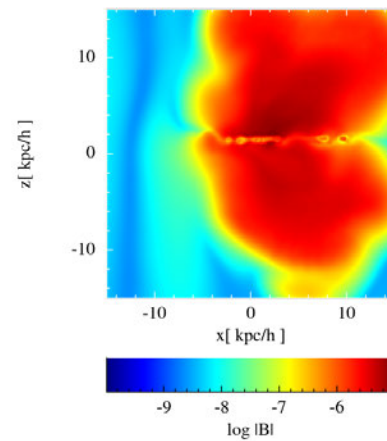
(a) halo-HMG-snB, face on slice



(b) halo-HMG-snB, edge on slice



(c) halo-HMG-B, face on slice



(d) halo-HMG-B, edge on slice

Figure 3.30: High mass galaxy with gas halo (halo-HMG) at $t = 3$ Gyr. The upper 2 panels show a slice of the simulation with the supernova magnetic seeded magnetic field. The lower 2 panels show a slice of the simulation with the primordial magnetic field. The color code shows the magnetic field strength in G and is unique for each of the subplots.

Magnetic Driven Outflows

Having a careful look at the magnetic field strength over time we notice a sudden growth of the mean magnetic field strength at around ~ 2 Gyr. Moreover, a peak in the pressure, surface density and star formation rate is observed at that time as it was mentioned in the discussion so far. In figure 3.31 a sequence of edge on cross section slices of the galaxy are displayed in order to show the generation of the outflow. In contrast to Steinwandel *et al.* 2018 (in prep.), we find different geometry of the outflows. The high magnetic field strength in the central region of the galaxy in conjunction with rotation is the underlying reason of these outflows. The magnetic field lines that are dense and highly rotated in the center of the galaxy, are creating a ring shaped configuration of the magnetic field strength in the center of the galaxy and since this cannot infinitely continue, this energy is released in the form of low density outflows above and below the galactic disk as shown in figure 3.31 and in figure 3.32. This outflow is driven by the high magnetic pressure in the center of the galaxy as is also shown in the pressure profiles of the figure 3.34. The middle panel of the last plot shows the magnetic pressure (purple line) and the thermal gas pressure (dark blue) at the time that the outflow starts to rise. The reason that the dashed lines that correspond to the halo-HMG-snB simulation do not show this trend is just because the outflow happens in later times. The high pressure results in high density regions ~ 3 kpc from the galactic center as shown in figure 3.36 which is probably an outcome of a shocked region. Therefore the density also rises and due to high pressure we observe high molecular surface density which is directly reflected to higher star formation rate in this region as shown in figure 3.35. It is worth noticing that the very central region of the galaxy, i.e., < 1 kpc has much lower density at the time of the outflow. From figure 3.33 we can notice that at the time that the magnetic outflow seems to rise (according to figure 3.31) the gas is not yet ejected from the galactic disk. This happens just after 2.24 Gyr when the magnetic bubble fully rises above and below the galactic disk together with low density gas. In figure 3.37 the temperature-density phase diagram is presented for the system halo-HMG-B at 2.34 Gyr, just after the wind up of the outflow. The outflow is seen as a few particles are going out of the disk towards the gas halo, which contributes to the magnetic and metal enrichment of the gas halo. These particles are acting as carriers for the magnetic field and allow the outflow to evolve. This feature does not happen in the case of the isolated galaxy since there is no medium around the disk. In that case just a few particles could be ejected from the galaxy with high magnetic fields and be totally disconnected from the galaxy.

The geometrical difference between our simulations and those of Steinwandel *et al.* 2018 (in prep.) is that the outflow in our case is not accelerated to high velocities and thus remains closer to the galaxy ($\max v_z \sim 500$ km/s). For the case of the simulation with the supernova seeded magnetic fields (halo-HMG-snB) the results are similar and the maps of the magnetic field are given in the Appendix. Our results are in accordance with [Pakmor and Springel, 2013] who found low density but highly magnetized rising bubbles around the galaxy at ~ 2 Gyr with similar geometry. These outflows are observed in a lot of simulations but in other cases they are claimed to have a different origin, as for instance in [Marinacci et al., 2011], where the outflows are driven by supernova powered bubbles.

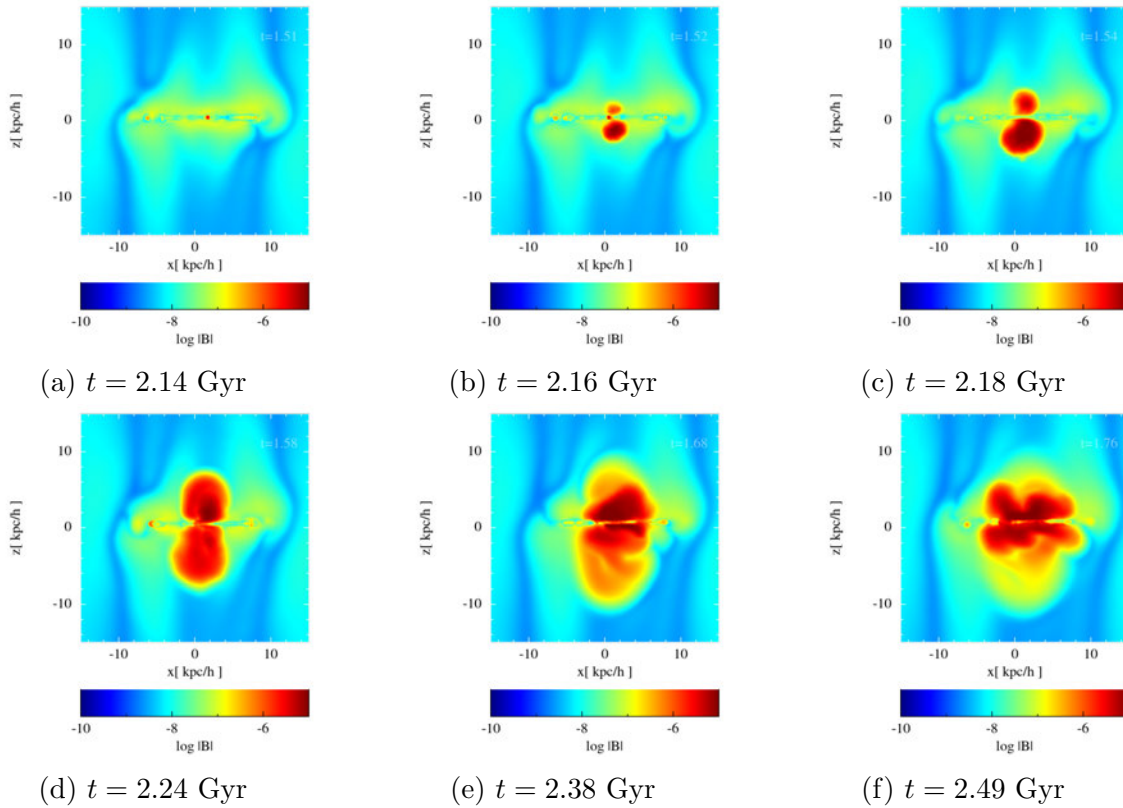


Figure 3.31: Edge on cross section slices of the simulation halo-HMG-B that show the start and evolution of the magnetic driven outflow. The color bar (same scale in every plot) show the magnetic field strength in Gauss.

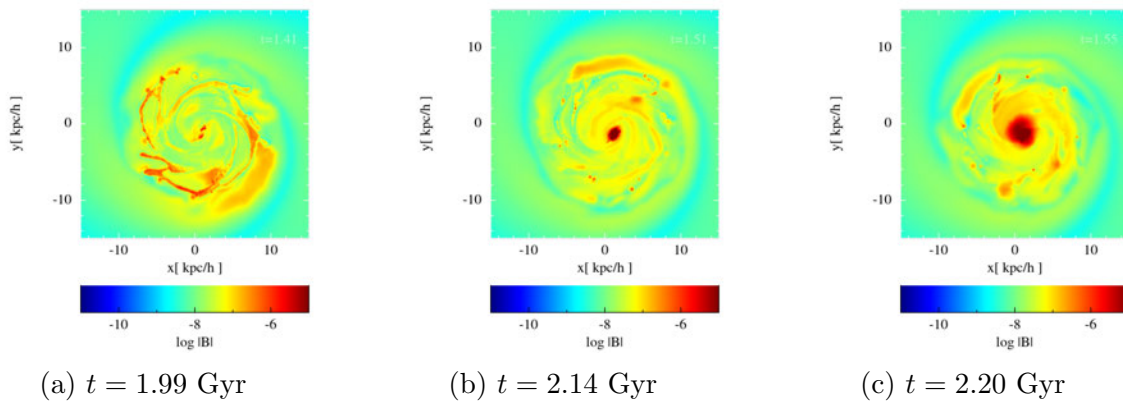


Figure 3.32: Face on cross section slices of the simulation halo-HMG-B before and at the start of the magnetic driven outflow. The color bar (same scale in every plot) shows the magnetic field strength in Gauss.

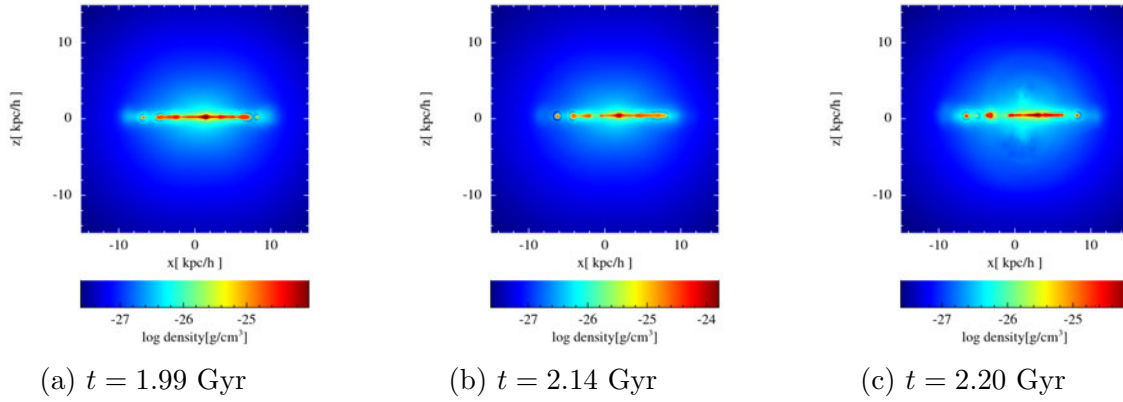


Figure 3.33: Face on cross section slice of the simulation halo-HMG-B before and at the start of the magnetic driven outflow. The color bar (same scale in every plot) shows the gas density.

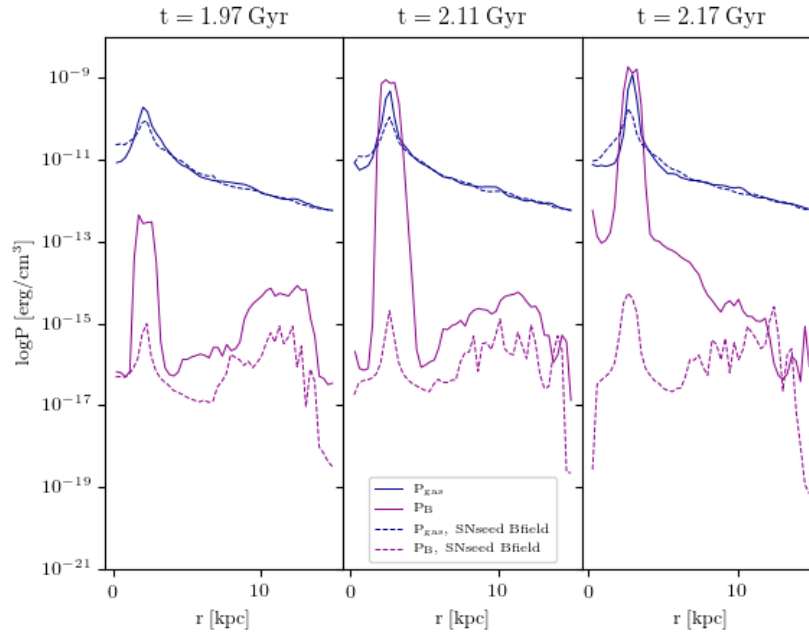


Figure 3.34: Radial profile of the thermal (dark blue) and magnetic (magenta) pressure of the gas before the outflow, at the start of the outflow and after a few years of evolution. With solid lines are shown the results from the halo-HMG-B simulation while the dashed lines show the results from the simulation halo-HMG-snB.

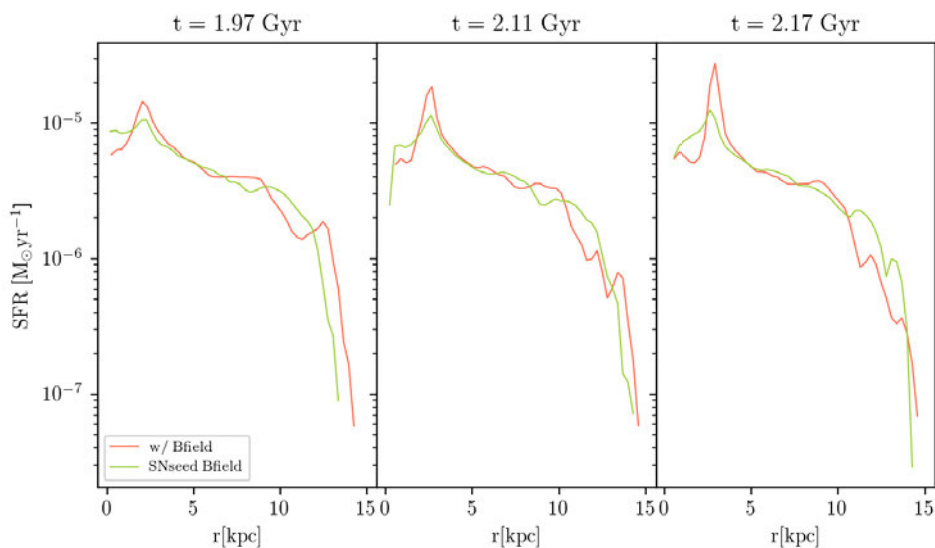


Figure 3.35: Mean star formation rate calculated in radial bins of the galactic radius before, at the start and a few years after the outflow. The simulation with the primordial magnetic field (halo-HMG-B) is shown in light green and the simulation with the supernova seeded field (halo-HMG-snB) is shown in orange.

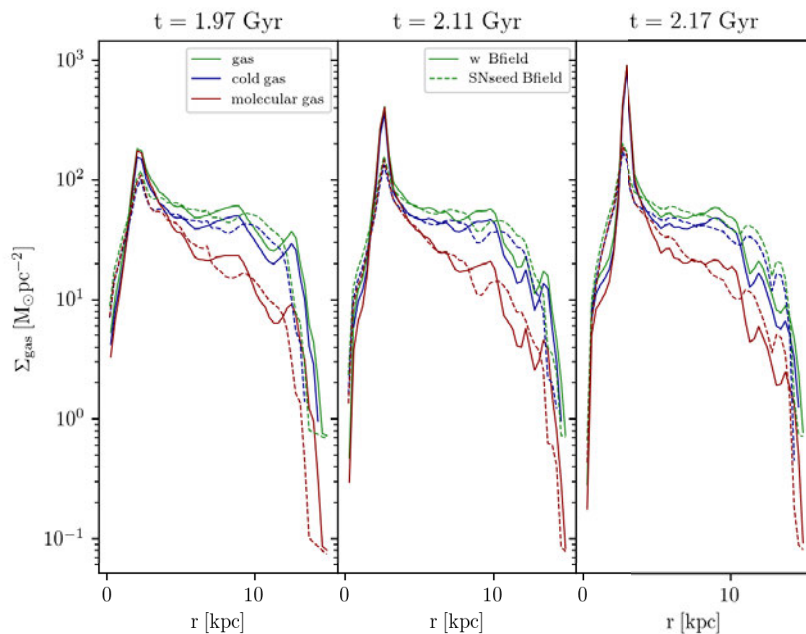


Figure 3.36: Radial profile of the surface density of different components of the gas before the outflow, at the start of the outflow and after a few years of evolution. In green is displayed the total gas of the galaxy, with dark blue the cold fraction of the gas and with dark red the molecular fraction. With solid lines are shown the results from the halo-HMG-B simulation while the dashed lines show the results from the simulation halo-HMG-snB.

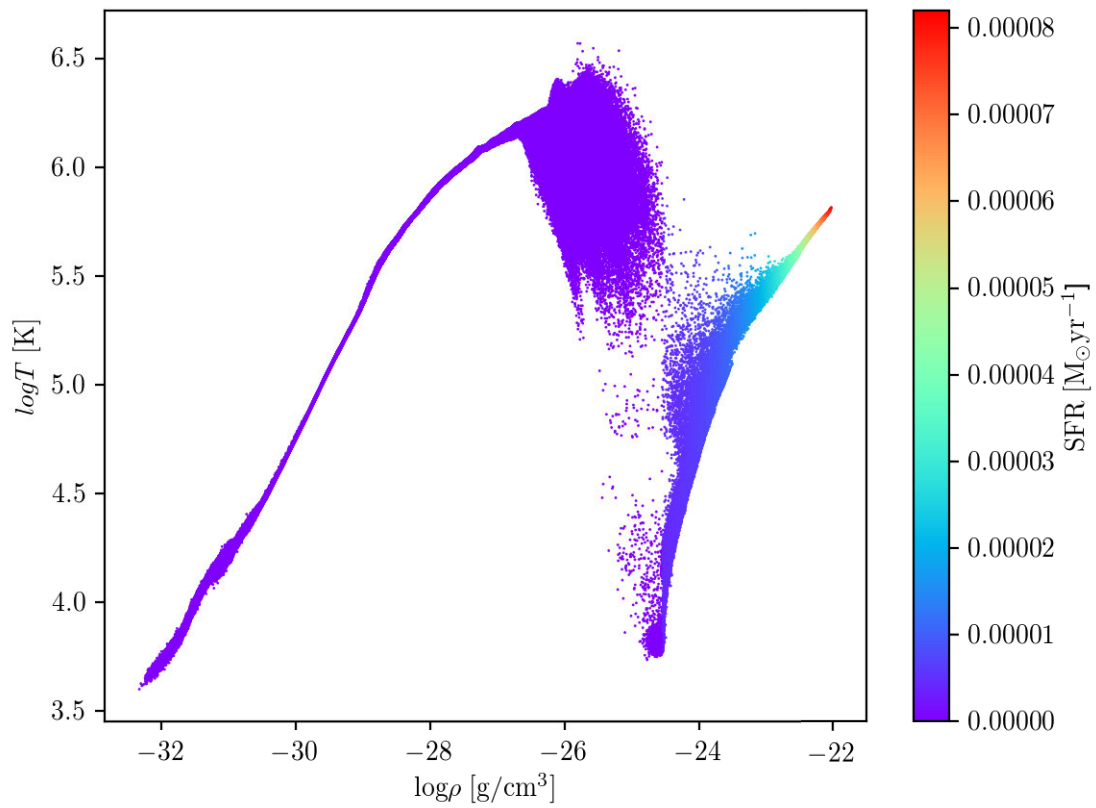


Figure 3.37: Effective temperature as a function of the gas density from the halo-HMG-B simulation. The color bar show the star formation rate per particle. The calculations are done at 2.34 Gyr, when the outflow has already grow above and bellow the galaxy.

Chapter 4

Summary and Conclusions

The progress of the numerical simulations has grown rapidly over the last years which made them an important tool for modern astrophysics. In many physical problems the correlated equations cannot be solved analytically, or in other problems the interplay of a large amount of physical processes make the analytic solution impossible or highly demanding. In the case of galaxy formation the basic interaction that dominates is gravity but is not limited to this. Star formation and feedback, cooling, turbulence, magnetic fields and cosmic rays are a few of the different processes that are taking place in a galaxy. For simulations that deal with the galaxy as a whole is usual not to have enough resolution in order to resolve all the processes that are involved in the evolution of the galaxy. Therefore, a common way to overcome this obstacle is to build realistic sub-grid recipes in order to model the unresolved physics. Here we presented a sub-grid model for star formation and feedback based on ideas of [Springel and Hernquist, 2003] and [Blitz and Rosolowsky, 2006]. The motivation of this work is to couple the sub-grid model for star formation with further physical processes. In our case we couple the star formation model with the magnetic fields and in particular with the supernova seeding model of [Beck et al., 2013]. This allows the interplay of the star formation and the magnetic fields in both directions. The supernova seeding model seeds the magnetic field from the supernova explosions, a parameter which is calculated from the star formation model and at the same time the magnetic pressure influences the star formation rate in our prescription (equation (2.51), equation (2.53)). The latter comes from the connection between the molecular fraction of the gas and the hydrostatic pressure of the galaxy, as calculated from observations [Blitz and Rosolowsky, 2006]. This is an important attribute of the model since it allows the star formation to occur from the molecular part of the gas and additionally introduces the influence of the magnetic field. This model is written in the SPH code GADGET with which we have performed simulations of an isolated galaxy and a galaxy surrounded by a hot gas halo (circum-galactic medium) using the same initial conditions as in Steinwandel *et al.* 2018 (in prep.). We find a well defined spiral structured galaxy and reproduce the basic properties of the ISM. In the case of the isolated disk galaxies (without the circum-galactic medium) we find better magnetic field configuration and amplification using the supernova seeding model instead of the primordial magnetic field. However, the non physical boundary conditions result in

a high magnetic field strength for some particles in the edge of the galactic disk. The star formation rate starts with a very high value that is an outcome of the initial conditions and then gradually decreases. The absence of inflowing gas and low magnetic fields settles the star formation rate below $1 M_{\odot}/\text{yr}$. Testing the new star formation model in galaxies with different total mass we find that all of them reproduce the slope of the Schmidt-Kennicutt relation without any further tuning of parameters.

To further test the star formation model in an isolated galaxy but in more realistic environment we added a circum-galactic medium of hot gas halo [Steinwandel *et al.* 2018 (in prep.)]. This offers the opportunity to study the system in a well-controlled setting without further perturbations. Similar results of the ISM, surface densities and star formation rate are found in this set of simulations as well. The star formation is further supported by the inflowing gas from the halo and the decrease over time is smoother. An interesting feature appears at 2.1 Gyr, namely highly magnetized low density bubbles arise above and below the galactic disk. This is accordance with other similar simulations, for example [Pakmor and Springel, 2013] and Steinwandel *et al.* 2018 (in prep.). The difference in the morphology of the outflow depends on the numerical set up and feedback mechanisms. We suspect that the outflow is a result of high magnetic pressure in the central region of the galaxy. In the case of the primordial magnetic field the outflow results in a steeper decrease of the star formation rate and a dip at ~ 2.6 Gyr. For the simulation with the supernova seeding the decrease remains smoother and the outflow appears later in time. Although the molecular fraction is proportional to the total pressure of the gas (as is the star formation rate) the high magnetic pressure will not increase the star formation since the high magnetic field particles have low density and are located in the bubbles above and below the galactic disk. These magnetic bubbles are rising a few kpc around the galaxy and they fall back in the outer edges of the disk. Furthermore it seems to perturb the disk as is shown in the radial profiles of the star formation rate and surface density of the gas (figure 3.22, figure 3.24). Consequently, because of the mass loss the star formation rate and surface density of the gas drops but also the prominence of the spiral arms is weaker after 3 Gyr of evolution (figure 3.21b, figure 3.21a). For both simulations we produce the magnetic power spectra (figure 3.27a, figure 3.27b). This is an indicator of the presence of small scale turbulence that amplifies the magnetic field in small scales. For the halo-HMG-B that we initiated the magnetic field with primordial field of $\mathbf{B} = (0, 0, 10^{-9} \text{ G})$ the amplification happens after the magnetic outflow. Moreover, from the power spectrum we would not claim that the turbulent dynamo is very efficient in this case. Contrary, the behaviour of the power spectrum for the halo-HMG-snB simulation shows an indication of small scale turbulence. Overall, from the maps of the galaxy (figure 3.28, figure 3.29 and figure 3.30) and the power spectrum (figure 3.27a) we can argue that the magnetic field is amplified from a small scale turbulent dynamo. The magnetic field for the halo-HMG-snB simulation shows a nice structure in the galactic disk which is always improved comparing to the results from the halo-HMG-B simulation.

In general, it seems that the new star formation model performs well but it always needs further testing in different systems, for example in zoom cosmological simulations or mergers. Since we have already introduced the opportunity of adding the effect of different

components of pressure, it would be interesting to add the effect of the turbulence and the cosmic rays in the star formation. As it was already mentioned in the introduction, the thermal and non thermal components of the ISM are dynamically important (figure 1.1). Therefore, to include them in a sub-grid model would potentially lead to a more precise prescription for the star formation. An interesting extension would be to include the magnetic energy in the energy balance of the gas in the interstellar medium (equation (2.60)). Therefore, the equilibrium solution should more accurately allow the influence of the energy of different components of the ISM. In that case, we should carefully think however how the non thermal part of the ISM is distributed between the cold and the hot phase. In the current version of the model we could also think to neglect the assumption of the constant temperature of the cold clouds. In this way we could follow the evolution of both hot and cold phase. This would require other assumptions since as we already fronted in chapter 2.2, is not trivial to implement an equilibrium solution.

Appendix

Here we present a couple of additional plots for completeness. First, we present 4 maps of the $\nabla \cdot \mathbf{B}$ of the Milky Way type galaxy with the circum-galactic medium (halo-HMG) for the 2 magnetic field models (primordial and supernova seeded field) at 2 points in time. This is important since in numerical simulations the divergence of the magnetic field is not always zero. Therefore, is important to keep the $\nabla \cdot \mathbf{B}$ as close to zero as possible so we do not have artificial amplification of the magnetic field.

We also show a sequence for the generation of the outflow for the supernova seeded magnetic field.

The rest of the plots are summarizing the results of the galaxies with different mass. The properties of these simulations are given in table 3.6.

Last, we show the temperature-density phase diagrams for different simulations.

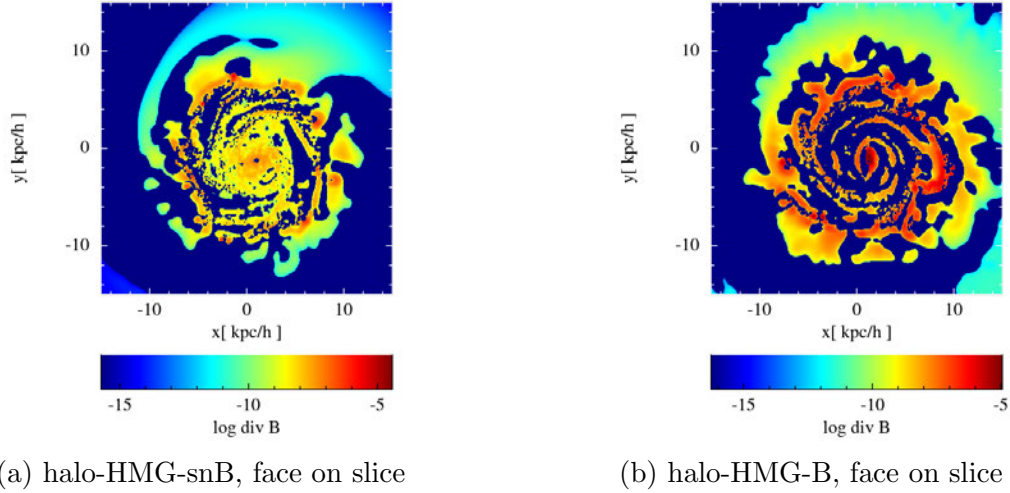


Figure 1: In this figure a cross section slice view of the galaxy is shown for the medium mass galaxy with the circum-galactic medium (halo-HMG-B and halo-HMG-snB) at $t = 2$ Gyr. *left*: simulation with supernova seeded magnetic field, *right*: simulation with the primordial magnetic field. The colorbar shows the divergence of the magnetic field. SPMHD simulations are not divergence free and therefore is important to keep this error as small as possible. Here we show a slice of the galaxy just before the outburst of the outflow, at 2 Gyr. In a few parts of the galaxy we achieve very good cleaning (dark blue regions) while there are others that the divB cleaning is not as efficient (dark red regions). In all cases it seems that the divergence error is small.

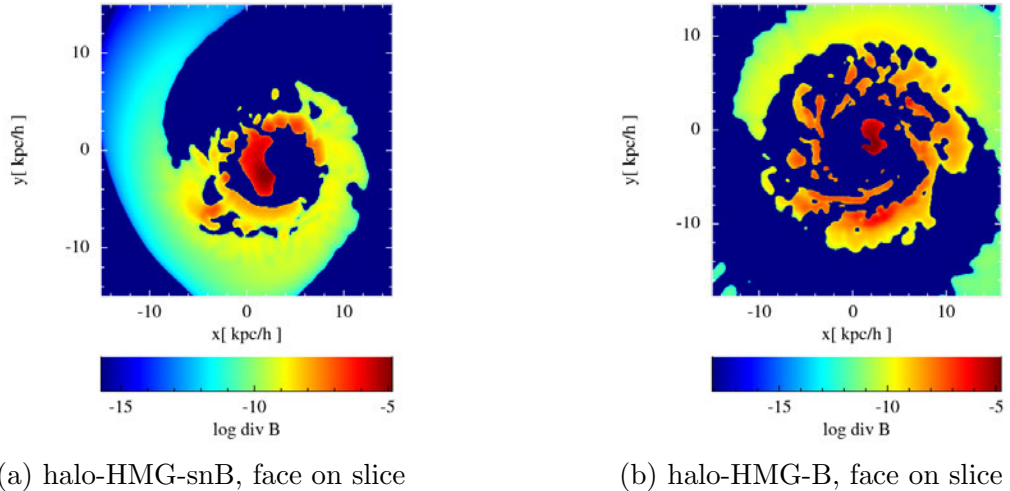


Figure 2: In this figure a cross section view of the galaxy is shown for the medium mass galaxy with the circum-galactic medium (halo-HMG-snB and halo-HMG-B) at $t = 2.7$ Gyr and 2.4 Gyr respectively. *left*: simulation with supernova seeded magnetic field, *right*: simulation with the primordial magnetic field. The colorbar shows divergence of the magnetic field. Here we show a slice of the galaxy after the outburst of the outflow, at ~ 2.4 Gyr for the primordial magnetic field simulation (right) and at ~ 2.7 Gyr for the supernova seeded magnetic field simulation.

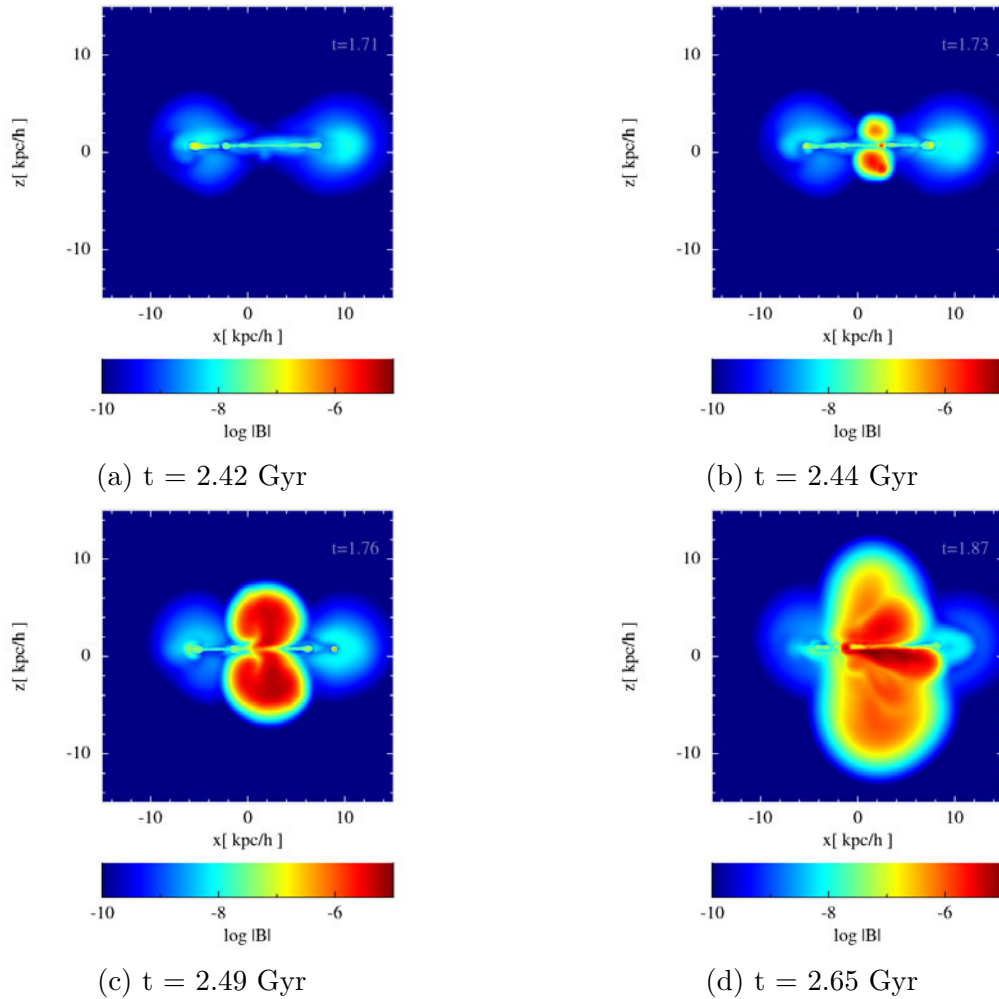


Figure 3: Cross section slice of the simulation halo-HMG-snB at the time of the outflow generation. The colorbar shows the magnetic field strength in Gauss.

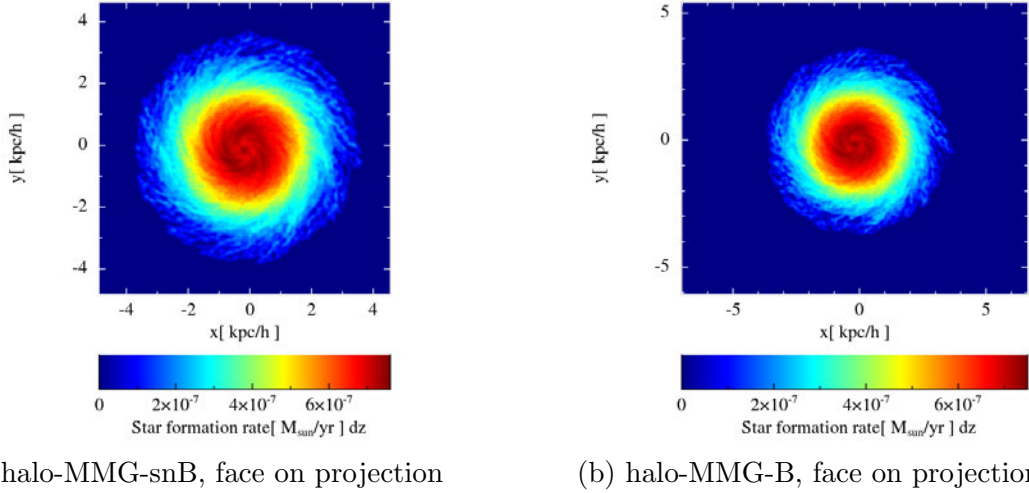


Figure 4: In this figure the projected view of the galaxy is shown for the medium mass galaxy with the circum-galactic medium (halo-MMG-B and halo-MMG-snB) at $t = 0.76$ Gyr. *left*: simulation with supernova seeded magnetic field, *right*: simulation with the primordial magnetic field. The colorbar shows the star formation rate integrated along z axis. The MMG galaxy is obviously smaller than the HMG that we presented in Chapter 3 and its morphological properties are not so prominent at this stage of evolution.

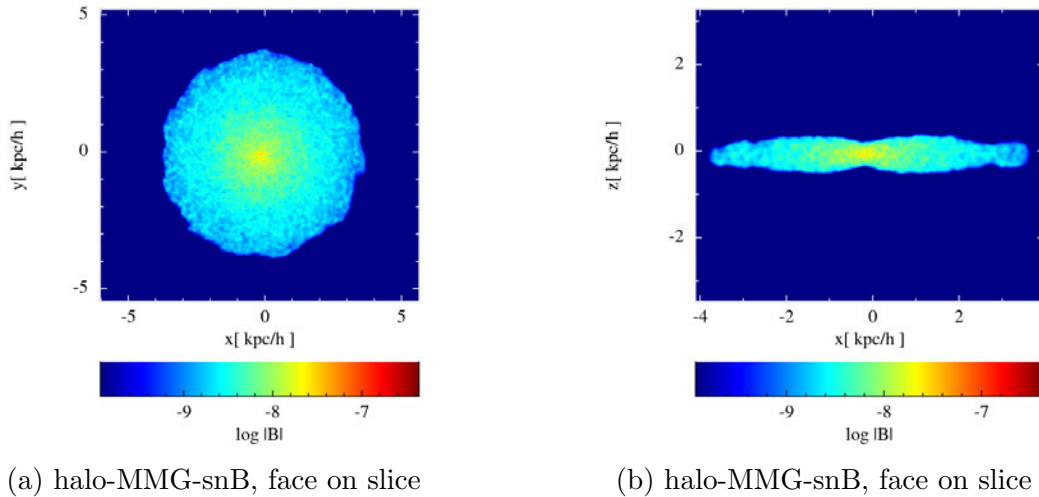


Figure 5: In this figure the cross section view of the galaxy is shown for the medium mass galaxy with the circum-galactic medium and supernova seeded magnetic field (halo-MMG-snB) at $t = 0.76$ Gyr. *left*: face on slice, *right*: edge on slice. The magnetic field is higher in the center due to higher star formation rate and is not enough amplified throughout the disk at this time.

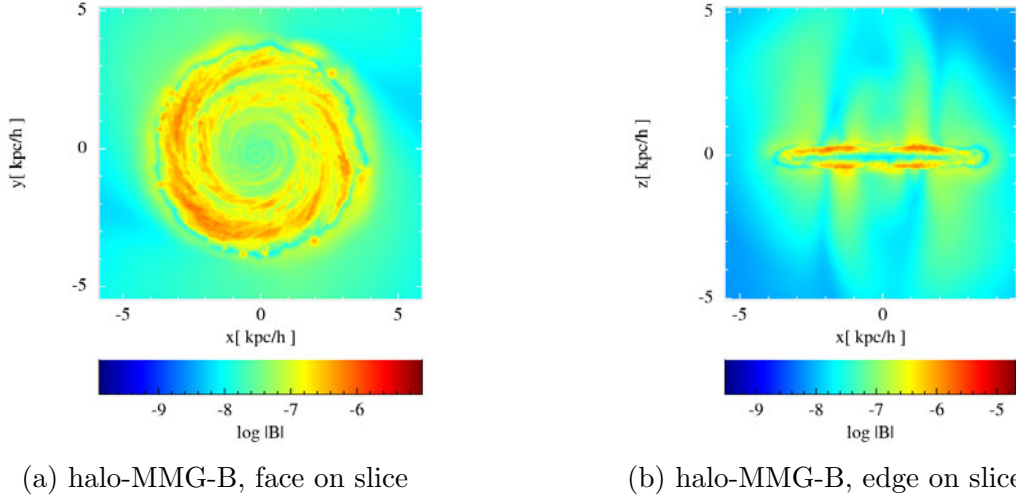


Figure 6: In this figure the cross section view of the galaxy is shown for the medium mass galaxy with the circum-galactic medium and primordial magnetic field assumption (halo-MMG-B) at $t = 0.76$ Gyr. *left*: face on slice, *right*: edge on slice. For this case the magnetic field is amplified due to rotation.

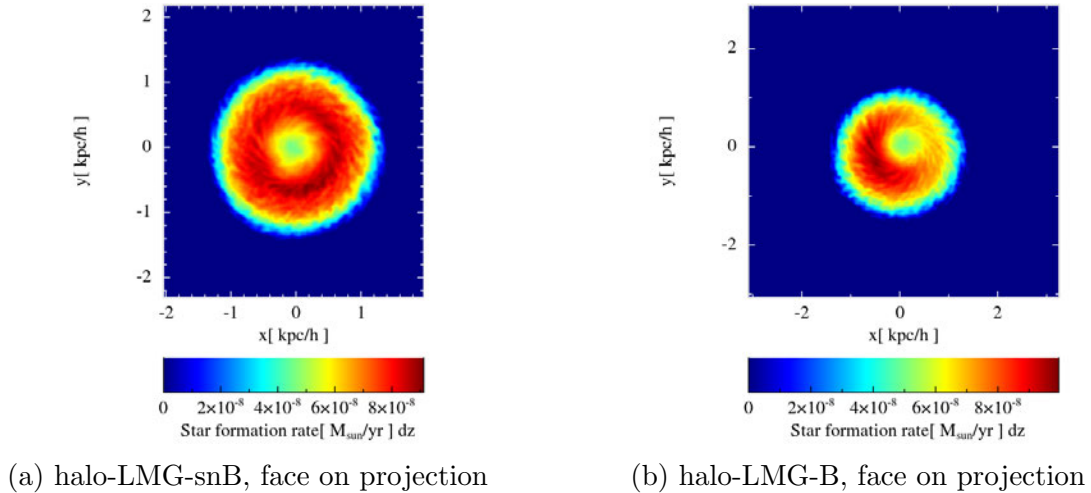
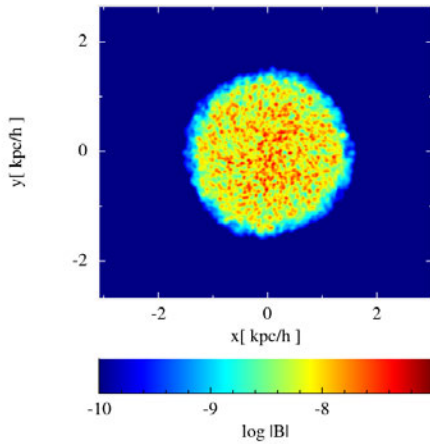
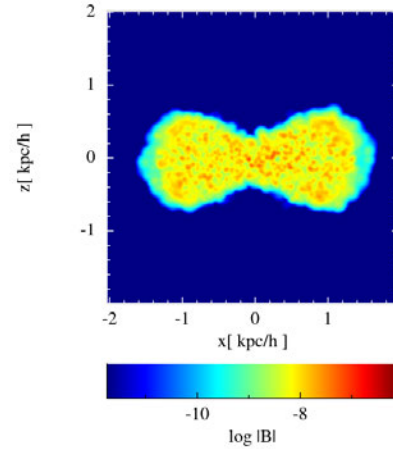


Figure 7: In this figure the projected view of the galaxy is shown for the low mass galaxy with the circum-galactic medium (halo-LMG-snB and halo-LMG-B) at $t = 1$ Gyr. *left*: simulation with supernova seeded magnetic field, *right*: simulation with the primordial magnetic field. The colorbar shows the star formation rate integrated along z axis. Here we suspect that the distorted and not detailed projection is due to over-softening ($\epsilon_{\text{gas}} = 0.1$ kpc/h).

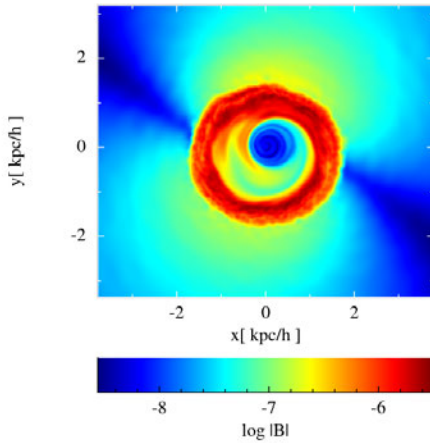


(a) halo-LMG-snB, face on slice

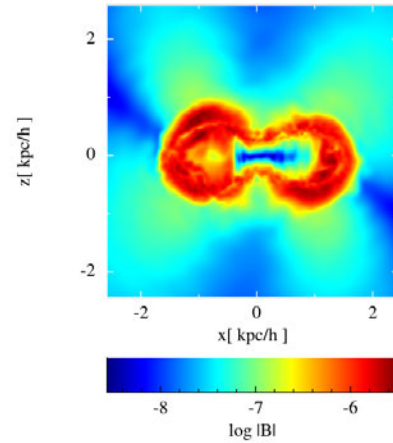


(b) halo-LMG-snB, face on slice

Figure 8: In this figure the cross section view of the galaxy is shown for the low mass galaxy with the circum-galactic medium and supernova seeded magnetic field (halo-LMG-snB) at $t = 1$ Gyr. The colorbar shows the magnetic field in Gauss. *left*: face on slice, *right*: edge on slice. Here the results of over-softening are also obvious. The magnetic field seeding is following the star formation.

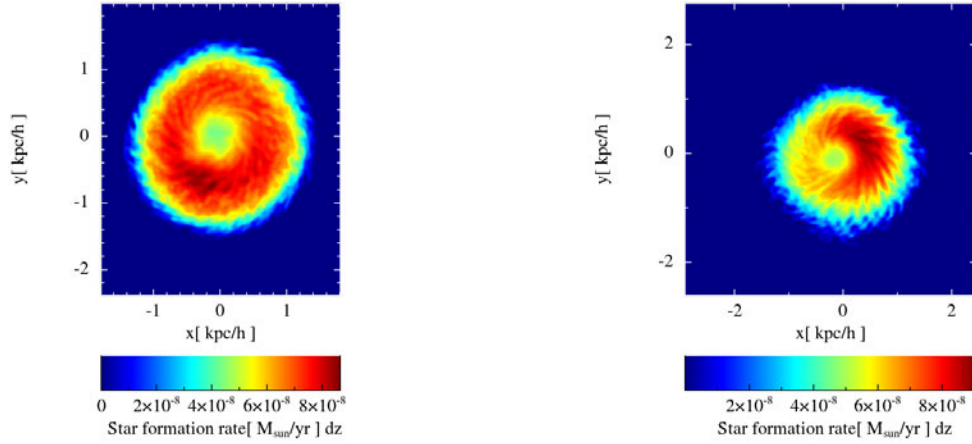


(a) halo-LMG-B, face on slice



(b) halo-LMG-B, face on slice

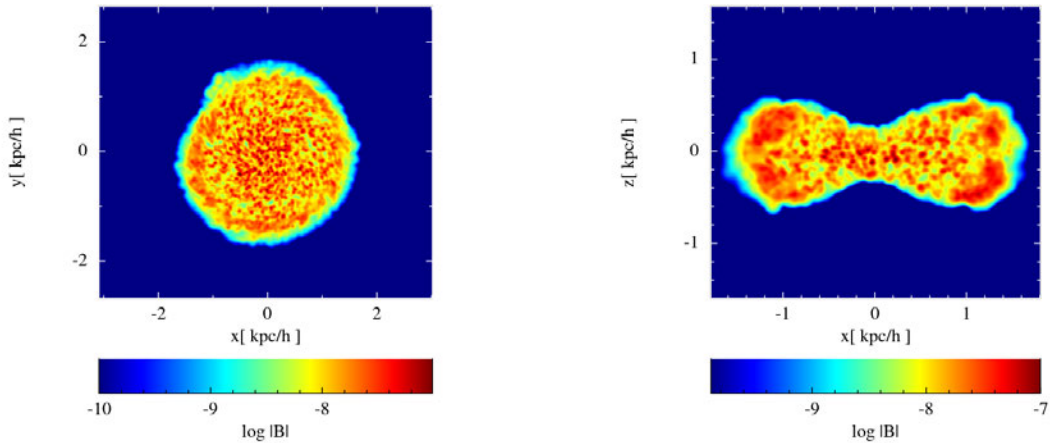
Figure 9: In this figure a cross section view of the galaxy is shown for the low mass galaxy with the circum-galactic medium and primordial magnetic field (halo-LMG-B) at $t = 1$ Gyr. The colorbar shows the magnetic field in Gauss. *left*: face on slice, *right*: edge on slice. In the case of primordial magnetic field seeding we notice a non physical amplification in the surrounding of the galaxy. We suggest to re-run this simulation with better settings.



(a) halo-LMG-snB, face on projection

(b) halo-LMG-B, face on projection

Figure 10: In this figure a projected view of the galaxy is shown for the low mass galaxy with the circumgalactic medium (halo-LMG-B and halo-LMG-snB) at $t = 1.4$ Gyr. *left*: simulation with supernova seeded magnetic field, *right*: simulation with the primordial magnetic field. The colorbar shows the star formation rate integrated along z axis.



(a) halo-LMG-snB, face on slice

(b) halo-LMG-snB, face on slice

Figure 11: In this figure a cross section view of the galaxy is shown for the low mass galaxy with the circumgalactic medium and supernova seeded magnetic field (halo-LMG-snB) at $t = 1$ Gyr. The colorbar shows the magnetic field in Gauss. *left*: face on slice, *right*: edge on slice. Here the results of over-softening are also obvious. The magnetic field seeding is following the star formation.

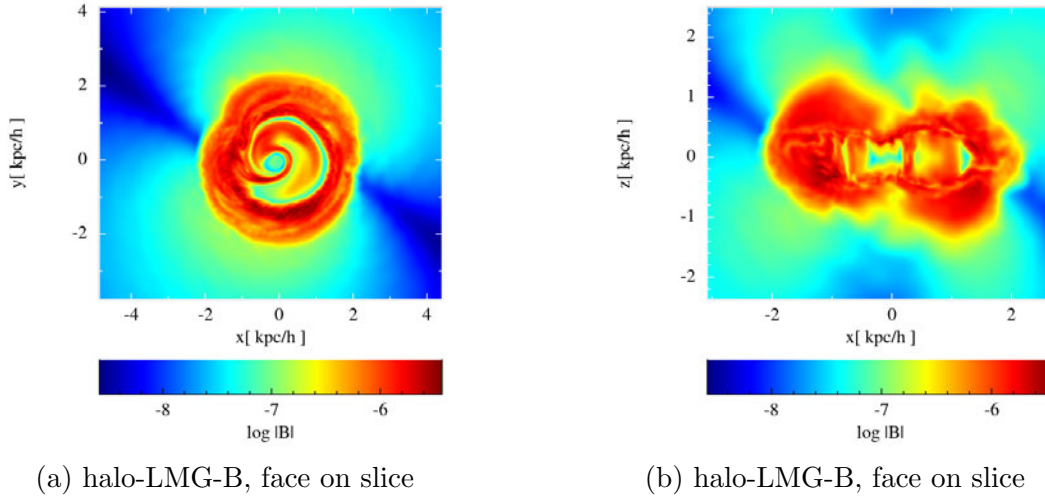


Figure 12: In this figure a cross section view of the galaxy is shown for the low mass galaxy with the circum-galactic medium and primordial magnetic field (halo-LMG-B) at $t = 1.4$ Gyr. The colorbar shows the magnetic field in Gauss. *left*: face on slice, *right*: edge on slice.

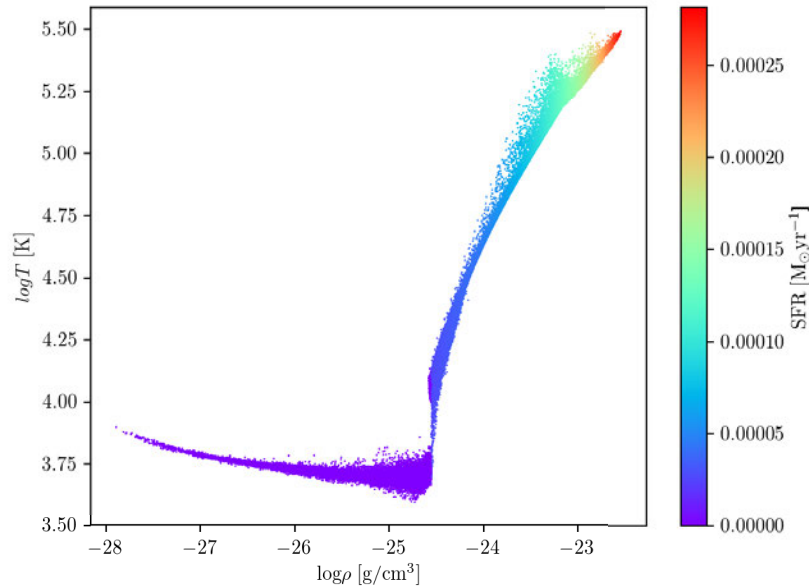


Figure 13: Effective temperature as a function of the gas density. The colorbar shows the star formation rate for each particle. This is at $t = 0.01$ Gyr for the simulation with SH03 and supernova seeded magnetic field.

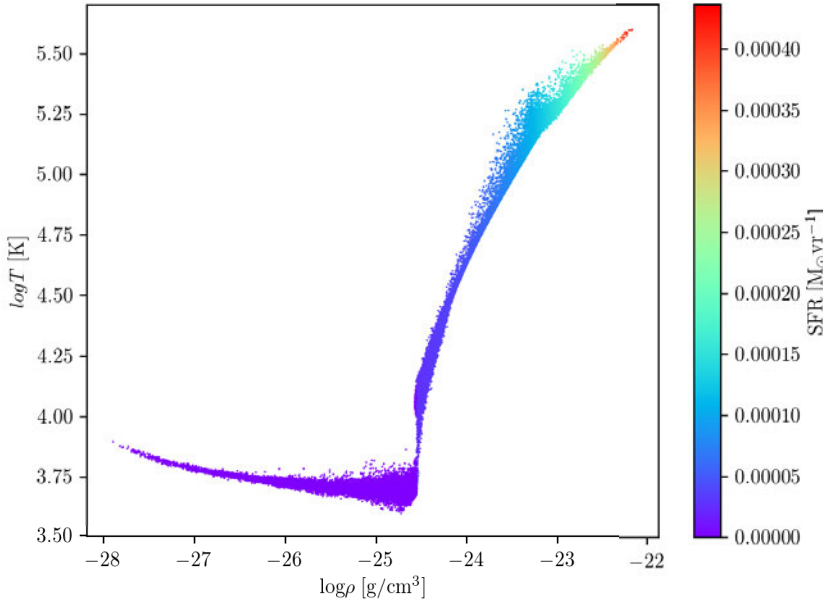


Figure 14: Effective temperature as a function of the gas density. The colorbar shows the star formation rate for each particle. This is at $t = 0.01$ Gyr for the simulation with SH03 and primordial magnetic field.

List of Figures

1.1	Energy densities of different components of the ISM. The component of the turbulent motion of the neutral gas is shown in blue, the total magnetic field in black, the cosmic rays, which are in equipartition with the ordered magnetic field, in green and the thermal energy of the warm was in red ($T = 10^4$ K). Taken from [Beck, 2016]	5
1.2	Magnetic field strengths (total and turbulent) measured by the degree of polarization versus the surface density of the star formation rate. [Tabatabaei et al., 2013]	6
1.3	Schematic representation of the oct-tree method (2D). The particles are first included in a single cube (root node) and then are every time divided until one node includes one particle. Taken from [Springel et al., 2001].	7
1.4	Different approaches to calculate the density from a random particle distribution. Left panel: particle-mesh method, central panel: calculation doing local sampling of the density, right panel: kernel density estimator. Taken from [Price, 2012].	9
1.5	Visual representation of different components of cosmological simulations. The common paradigm for cosmological simulations is to occupy a large box which includes large scale structures such as galaxy and galaxy clusters. It is important to model the physics for the intergalactic medium, then in lower scales the galaxies and the interstellar medium. Many physical processes are happening in small scales, for example star and planet formation, but is not possible to resolve them in the cosmological simulations. Therefore, we build realistic sub-grid models in order to mimic the unresolved physics. Taken from: http://www.usm.uni-muenchen.de/Masterarbeiten.php	13
2.1	Mass flow and description of the processes taking place between the different phases of the gas.	17
2.2	Temperature of the gas plotted against the baryonic overdensity. The temperature has 3 components, i.e., the upper thin line corresponds to the temperature of the hot phase of the gas, the middle to the effective gas and the lower dashed line to the cold clouds. From [Springel and Hernquist, 2003].	19
2.3	Fraction of cold clouds as a function of the baryonic overdensity. From [Springel and Hernquist, 2003].	20

2.4	The star formation rate per unit area as a function of the gas density of the galaxy. The dashed inclined line shows the observational Schmidt-Kennicutt relation while the vertical dashed line indicates the observational cut-off. The upper dotted line is the prediction of the model for $t_0^* = 0.53$ Gyr, the lower for $t_0^* = 8.4$ Gyr and the solid line is the best fit for $t_0^* = 2.1$ Gyr. Plot taken from [Springel and Hernquist, 2003]	22
2.5	Mass flow and physical processes between the different phases of the interstellar medium.	25
2.6	Cold fraction as a function of density. In orange points is the result of the new -pressure based- star formation model and in green the result from [Springel and Hernquist, 2003] are shown for comparison.	33
2.7	Star formation rate per surface as a function of the surface density of the gas in a galaxy for different star formation efficiency parameters. The black solid line is the observational Schmidt Kennicutt relation and the grey lines its errors. (The quantities are azimuthally averaged).	35
2.8	Star formation rate per surface as a function of the surface density of the gas in a galaxy for different values of the parameter P_0 . The black solid line is the observational Schmidt Kennicutt relation and the grey lines its errors.	36
2.9	Cold fraction as a function of the gas density. In orange is the result of the new -pressure based- star formation model and in green the case for lower temperature of the cold clouds.	37
2.10	Star formation rate per surface as a function of the surface density of the gas in a galaxy for different temperature of cold clouds. The black solid line is the observational Schmidt Kennicutt relation and the grey lines its errors.	38
3.1	RJ1A test, $t = 5.25$. In all plots the red line shows the result from ATHENA code while the black lines are the results from the tests using GADGET code. From left to right in the upper row the first panel shows the density, the middle shows the $v_{x,z}$ and the right panel the total energy and thermal energy. In the low row the first panel shows the v_y , the middle shows all the components of the magnetic field and the last one shows the relative divergence error. In the x axis is always the x-direction of the tube.	43
3.2	Test RJ2A, $t = 24.5$. Same plots as in figure 3.1.	44
3.3	Test RJ5A, $t = 7$. Same plots as in figure 3.1	44
3.4	Phase diagram at $t = 0.01$ Gyr for the high mass galaxy (HMG-SH) color coded by the star formation rate per particle.	48
3.5	Radial profile of star formation rate for the HMG using SH03. As the legend implies, the light blue line corresponds to the simulation without magnetic fields, the orange to the simulation with magnetic fields and finally the green to the simulation with the supernova seeded magnetic fields.	48

3.6	Star formation rate as a function of the time. The colors indicate the different set up for the magnetic field. In blue the galaxy without magnetic field, in orange with primordial magnetic field and in green the galaxy with supernova seeded magnetic field.	49
3.7	Pressure radial profiles at different times for the simulation with primordial magnetic field (solid lines) and with the simulation with the supernova seeding model (dashed lines). In blue the thermal gas pressure is shown while in magenta is shown the magnetic pressure.	50
3.8	High mass galaxy (HMG-SH03) at 1 Gyr with different magnetic field models. The panel (a) shows the face on projection of the galaxy with supernova seeded magnetic field. The panel (b) shows the face on projection of the galaxy with primordial magnetic field. The color bar shows the integrated magnetic field strength over the z (vertical) direction.	50
3.9	Phase diagram of the high mass galaxy (HMG-B) with magnetic fields and the new star formation model at $t = 0.01$ Gyr. The color code shows the star formation rate that corresponds to each particle.	51
3.10	Thermal and magnetic pressure as a function of the galactic radius. The thermal (blue) and magnetic (magenta) are shown for the 2 different magnetic field models, i.e. the solid lines are from the high mass galaxy with primordial magnetic field and the dashed lines are from the high mass galaxy simulation with supernova seeded magnetic field.	52
3.11	High mass galaxy, with the new star formation model, at 1 Gyr with different magnetic field models. The panel (a) shows the face on projection of the galaxy with supernova seeded magnetic field. The panel (b) shows the face on projection of the galaxy with primordial magnetic field. The color bar shows the integrated magnetic field strength (in gauss) over the z (vertical) direction.	53
3.12	Radial profile of the star formation rate of the high mass galaxy (HMG). The different colors correspond to different magnetic field models, with no magnetic field (light blue), primordial magnetic field (orange) and supernova seeded magnetic field (green).	54
3.13	High mass galaxy, with the new star formation model, at 1 Gyr with different magnetic field models. The panel (a) shows the face on projection of the galaxy with supernova seeded magnetic field. The panel (b) shows the face on projection of the galaxy with primordial magnetic field and the panel (c) without magnetic field. The color bar shows the star formation rate integrated over the z (vertical) direction.	55
3.14	Surface density radial profiles of different components of the interstellar medium. The different colors show different components of the ISM with green to be the total gas, blue the cold gas, and red the molecular gas. The solid lines represent calculations from the HMG-B simulation while the dashed lines for the HMG-snB.	56

3.15	Star formation rate as a function of time for the set of simulations with the new star formation model. The simulations are performed for the high mass galaxy without magnetic fields (HMG-noB, light blue line), with primordial magnetic field (HMG-B, orange line), and with the supernova seeding model (HMG-snB, light green).	57
3.16	Schmidt Kennicutt relation for galaxy simulations with different masses. In solid line the observational Schmidt Kennicutt relation its shown and the grey lines are the errors (equation (2.22)). The different galaxies have total mass : LMG - $M = 10^{10} M_{\odot}$, MMG - $M = 10^{11} M_{\odot}$, HMG - $M = 10^{12} M_{\odot}$ and VHMG - $M = 10^{13} M_{\odot}$	57
3.17	Temperature-density diagram for the halo-HMG-B system at $t = 0.01$ Gyr. The upper group of particles corresponds to the particles of the gas halo while the down part corresponds to the gas particles of the galaxy	61
3.18	Temperature-density diagram for the halo-HMG-B system at $t = 1$ Gyr. The colorbar shows the star formation rate per particle.	62
3.19	High mass galaxy with gas halo (halo-HMG) projection at $t = 1$ Gyr for the simulation with the supernova seeded magnetic field. The color code in the plots is the star formation rate integrated along the z direction.	63
3.20	High mass galaxy with gas halo (halo-HMG) projection at $t = 2$ Gyr. The left panel shows a projection of the galactic disk for the simulation with the supernova seeded magnetic field. The right panel show the projected disk of the simulation with the primordial magnetic field. The color code in all plots is the star formation rate integrated along the z direction.	63
3.21	High mass galaxy with gas halo (halo-HMG) projection at $t = 3$ Gyr. The left panel shows a projection of the galactic disk for the simulation with the supernova seeded magnetic field. The right panel show the projected disk of the simulation with the primordial magnetic field. The color code in all plots is the star formation rate integrated along the z direction.	64
3.22	Star formation rate calculated in radial bins of the galactic radius. In orange is plotted the result from the halo-HMG-B and with light green from the halo-HMG-snB.	64
3.23	Mean pressure calculated in radial bins of the galactic radius in 3 different points in time. The dark blue lines show the thermal gas pressure while the magenta lines show the magnetic pressure. The solid lines are calculations from the halo-HMG-B simulation and the dashes lines are results from the simulation halo-HMG-snB.	65
3.24	Radial profile of the surface density for different components of the ISM. The mean surface density of the total gas (green), the cold gas (blue) and the molecular fraction (red) are shown as a function of the galactic radius. The solid lines correspond to the halo-HMG-B simulation and the dashed lines to the halo-HMG-snB simulation.	66

3.25	Mean magnetic field evolution with time. In dark blue is the result from the halo-HMG-B simulation while in light blue is the result from the halo-HMG-snB simulation.	67
3.26	Star formation rate as a function of time. The star formation rate from the simulation with the primordial magnetic field is shown in light green, while the star formation rate of the simulation with the supernova seeding is shown in light orange.	67
3.27	Magnetic power spectra for the simulations halo-HMG-snB (left) and halo-HMG-B (right) for different points in time as it is indicated in the legends. For early times the turbulent dynamo theory predicts $P(k) \propto k^{3/2}$ [Kazantsev et al., 1985] and at later times the small scale dynamo stops and the power spectra follows $P(k) \propto k^{-3/2}$ [Iroshnikov, 1963]. For the case of halo-HMG-snB the power spectrum seems to follow the expected slopes and we could claim that there is an evidence for the operation of turbulent dynamo in the disk. However this is not the case for the simulation. It is not clear if the power spectrum follows the Kazantsev slope in early times. This is in accordance to the rest of our results since in the case of halo-HMG-B we do not notice an efficient amplification of the magnetic field strength before 2 Gyr (figure 3.25).	69
3.28	High mass galaxy with gas halo (halo-HMG) at $t = 1$ Gyr. The upper 2 panels show a slice of the simulation with the supernova seeded magnetic field. The lower 2 panels show a slice of the simulation with the primordial magnetic field. The color code shows the magnetic field strength in G and is unique for each of the subplots.	70
3.29	High mass galaxy with gas halo (halo-HMG) at $t = 2$ Gyr. The upper 2 panels show a slice of the simulation with the supernova magnetic seeded magnetic field. The lower 2 panels show a slice of the simulation with the primordial magnetic field. The color code shows the magnetic field strength in G and is unique for each of the subplots.	71
3.30	High mass galaxy with gas halo (halo-HMG) at $t = 3$ Gyr. The upper 2 panels show a slice of the simulation with the supernova magnetic seeded magnetic field. The lower 2 panels show a slice of the simulation with the primordial magnetic field. The color code shows the magnetic field strength in G and is unique for each of the subplots.	72
3.31	Edge on cross section slices of the simulation halo-HMG-B that show the start and evolution of the magnetic driven outflow. The color bar (same scale in every plot) show the magnetic field strength in Gauss.	74
3.32	Face on cross section slices of the simulation halo-HMG-B before and at the start of the magnetic driven outflow. The color bar (same scale in every plot) shows the magnetic field strength in Gauss.	74
3.33	Face on cross section slice of the simulation halo-HMG-B before and at the start of the magnetic driven outflow. The color bar (same scale in every plot) shows the gas density.	75

3.34	Radial profile of the thermal (dark blue) and magnetic (magenta) pressure of the gas before the outflow, at the start of the outflow and after a few years of evolution. With solid lines are shown the results from the halo-HMG-B simulation while the dashed lines show the results from the simulation halo-HMG-snB.	75
3.35	Mean star formation rate calculated in radial bins of the galactic radius before, at the start and a few years after the outflow. The simulation with the primordial magnetic field (halo-HMG-B) is shown in light green and the simulation with the supernova seeded field (halo-HMG-snB) is shown in orange.	76
3.36	Radial profile of the surface density of different components of the gas before the outflow, at the start of the outflow and after a few years of evolution. In green is displayed the total gas of the galaxy, with dark blue the cold fraction of the gas and with dark red the molecular fraction. With solid lines are shown the results from the halo-HMG-B simulation while the dashed lines show the results from the simulation halo-HMG-snB.	76
3.37	Effective temperature as a function of the gas density from the halo-HMG-B simulation. The color bar show the star formation rate per particle. The calculations are done at 2.34 Gyr, when the outflow has already grow above and bellow the galaxy.	77
1	In this figure a cross section slice view of the galaxy is shown for the medium mass galaxy with the circum-galactic medium (halo-HMG-B and halo-HMG-snB) at $t = 2$ Gyr. <i>left</i> : simulation with supernova seeded magnetic field, <i>right</i> : simulation with the primordial magnetic field. The colorbar shows the divergence of the magnetic field. SPMHD simulations are not divergence free and therefore is important to keep this error as small as possible. Here we show a slice of the galaxy just before the outburst of the outflow, at 2 Gyr. In a few parts of the galaxy we achieve very good cleaning (dark blue regions) while there are others that the divB cleaning is not as efficient (dark red regions). In all cases it seems that the divergence error is small.	84
2	In this figure a cross section view of the galaxy is shown for the medium mass galaxy with the circum-galactic medium (halo-HMG-snB and halo-HMG-B) at $t = 2.7$ Gyr and 2.4 Gyr respectively. <i>left</i> : simulation with supernova seeded magnetic field, <i>right</i> : simulation with the primordial magnetic field. The colorbar shows divergence of the magnetic field. Here we show a slice of the galaxy after the outburst of the outflow, at ~ 2.4 Gyr for the primordial magnetic field simulation (right) and at ~ 2.7 Gyr for the supernova seeded magnetic field simulation.	84
3	Cross section slice of the simulation halo-HMG-snB at the time of the outflow generation. The colorbar shows the magnetic field strength in Gauss.	85

-
- 4 In this figure the projected view of the galaxy is shown for the medium mass galaxy with the circum-galactic medium (halo-MMG-B and halo-MMG-snB) at $t = 0.76$ Gyr. *left*: simulation with supernova seeded magnetic field, *right*: simulation with the primordial magnetic field. The colorbar shows the star formation rate integrated along z axis. The MMG galaxy is obviously smaller than the HMG that we presented in Chapter 3 and its morphological properties are not so prominent at this stage of evolution. 86
- 5 In this figure the cross section view of the galaxy is shown for the medium mass galaxy with the circum-galactic medium and supernova seeded magnetic field (halo-MMG-snB) at $t = 0.76$ Gyr. *left*: face on slice, *right*: edge on slice. The magnetic field is higher in the center due to higher star formation rate and is not enough amplified throughout the disk at this time. 86
- 6 In this figure the cross section view of the galaxy is shown for the medium mass galaxy with the circum-galactic medium and primordial magnetic field assumption (halo-MMG-B) at $t = 0.76$ Gyr. *left*: face on slice, *right*: edge on slice. For this case the magnetic field is amplified due to rotation. . . . 87
- 7 In this figure the projected view of the galaxy is shown for the low mass galaxy with the circum-galactic medium (halo-LMG-snB and halo-LMG-B) at $t = 1$ Gyr. *left*: simulation with supernova seeded magnetic field, *right*: simulation with the primordial magnetic field. The colorbar shows the star formation rate integrated along z axis. Here we suspect that the distorted and not detailed projection is due to over-softening ($\epsilon_{\text{gas}} = 0.1$ kpc/h). . . . 87
- 8 In this figure the cross section view of the galaxy is shown for the low mass galaxy with the circum-galactic medium and supernova seeded magnetic field (halo-LMG-snB) at $t = 1$ Gyr. The colorbar shows the magnetic field in Gauss. *left*: face on slice, *right*: edge on slice. Here the results of over-softening are also obvious. The magnetic field seeding is following the star formation. 88
- 9 In this figure a cross section view of the galaxy is shown for the low mass galaxy with the circum-galactic medium and primordial magnetic field (halo-LMG-B) at $t = 1$ Gyr. The colorbar shows the magnetic field in Gauss. *left*: face on slice, *right*: edge on slice. In the case of primordial magnetic field seeding we notice a non physical amplification in the surrounding of the galaxy. We suggest to re-run this simulation with better settings. 88
- 10 In this figure a projected view of the galaxy is shown for the low mass galaxy with the circum-galactic medium (halo-LMG-B and halo-LMG-snB) at $t = 1.4$ Gyr. *left*: simulation with supernova seeded magnetic field, *right*: simulation with the primordial magnetic field. The colorbar shows the star formation rate integrated along z axis. 89

11	In this figure a cross section view of the galaxy is shown for the low mass galaxy with the circum-galactic medium and supernova seeded magnetic field (halo-LMG-snB) at $t = 1$ Gyr. The colorbar shows the magnetic field in Gauss. <i>left</i> : face on slice, <i>right</i> : edge on slice. Here the results of over-softening are also obvious. The magnetic field seeding is following the star formation.	89
12	In this figure a cross section view of the galaxy is shown for the low mass galaxy with the circum-galactic medium and primordial magnetic field (halo-LMG-B) at $t = 1.4$ Gyr. The colorbar shows the magnetic field in Gauss. <i>left</i> : face on slice, <i>right</i> : edge on slice.	90
13	Effective temperature as a function of the gas density. The colorbar shows the star formation rate for each particle. This is at $t = 0.01$ Gyr for the simulation with SH03 and supernova seeded magnetic field.	90
14	Effective temperature as a function of the gas density. The colorbar shows the star formation rate for each particle. This is at $t = 0.01$ Gyr for the simulation with SH03 and primordial magnetic field.	91

List of Tables

2.1	Table of model parameters	37
3.1	Initial conditions for the left and right side of the shock tubes for the MHD tests.	42
3.2	Parameters for the initial conditions of isolated Milky Way type galaxy . .	46
3.3	Number of different particle types	46
3.4	Mass resolution	46
3.5	Parameters for the gas halo	59
3.6	Parameters for the systems with disk galaxy and gas halo	59

Bibliography

- [Adebahr et al., 2013] Adebahr, B., Krause, M., Klein, U., Weżgowiec, M., Bomans, D., and Dettmar, R.-J. (2013). M 82–a radio continuum and polarisation study-i. data reduction and cosmic ray propagation. *Astronomy & Astrophysics*, 555:A23.
- [Arshakian et al., 2009] Arshakian, T. G., Beck, R., Krause, M., and Sokoloff, D. (2009). Evolution of magnetic fields in galaxies and future observational tests with the square kilometre array. *Astronomy & Astrophysics*, 494(1):21–32.
- [Balsara, 1995] Balsara, D. S. (1995). Von neumann stability analysis of smoothed particle hydrodynamic suggestions for optimal algorithms. *Journal of Computational Physics*, 121(2):357–372.
- [Beck et al., 2013] Beck, A. M., Dolag, K., Lesch, H., and Kronberg, P. P. (2013). Strong magnetic fields and large rotation measures in protogalaxies from supernova seeding. *Monthly Notices of the Royal Astronomical Society*, 435(4):3575–3586.
- [Beck, 2016] Beck, R. (2016). Magnetic fields in spiral galaxies. *The Astronomy and Astrophysics Review*, 24(1):4.
- [Beck et al., 1996] Beck, R., Brandenburg, A., Moss, D., Shukurov, A., and Sokoloff, D. (1996). Galactic magnetism: recent developments and perspectives. *Annual review of astronomy and astrophysics*, 34(1):155–206.
- [Beck et al., 1994] Beck, R., Poezd, A., Shukurov, A., and Sokoloff, D. (1994). Dynamos in evolving galaxies. *Astronomy and Astrophysics*, 289:94–100.
- [Bell, 2003] Bell, E. F. (2003). Estimating star formation rates from infrared and radio luminosities: the origin of the radio-infrared correlation. *The Astrophysical Journal*, 586(2):794.
- [Biermann, 1950] Biermann, L. (1950). L. biermann, z. naturforsch. 5a, 65 (1950). *Z. Naturforsch.*, 5:65.
- [Bisnovatyi-Kogan et al., 1973] Bisnovatyi-Kogan, G., Ruzmaikin, A., and Syunyaev, R. (1973). Star contraction and magnetic-field generation in protogalaxies. Technical report, Institute of Applied Mathematics, Academy of Sciences of the USSR.

- [Blitz and Rosolowsky, 2006] Blitz, L. and Rosolowsky, E. (2006). The role of pressure in gmc formation ii: The h2-pressure relation. *The Astrophysical Journal*, 650(2):933.
- [Brio and Wu, 1988] Brio, M. and Wu, C. C. (1988). An upwind differencing scheme for the equations of ideal magnetohydrodynamics. *Journal of computational physics*, 75(2):400–422.
- [Cavaliere and Fusco-Femiano, 1978] Cavaliere, A. and Fusco-Femiano, R. (1978). The distribution of hot gas in clusters of galaxies. *Astronomy and Astrophysics*, 70:677.
- [Chorin, 1967] Chorin, A. J. (1967). A numerical method for solving incompressible viscous flow problems. *Journal of computational physics*, 2(1):12–26.
- [Chyży, 2008] Chyży, K. (2008). Magnetic fields and gas in the cluster-influenced spiral galaxy ngc 4254-ii. structures of magnetic fields. *Astronomy & Astrophysics*, 482(3):755–769.
- [Chyży et al., 2007] Chyży, K., Bomans, D., Krause, M., Beck, R., Soida, M., and Urbanik, M. (2007). Magnetic fields and ionized gas in nearby late type galaxies. *Astronomy & Astrophysics*, 462(3):933–941.
- [Cox, 2005] Cox, D. P. (2005). The three-phase interstellar medium revisited. *Annu. Rev. Astron. Astrophys.*, 43:337–385.
- [Dehnen and Aly, 2012] Dehnen, W. and Aly, H. (2012). Improving convergence in smoothed particle hydrodynamics simulations without pairing instability. *Monthly Notices of the Royal Astronomical Society*, 425(2):1068–1082.
- [Di Matteo et al., 2005] Di Matteo, T., Springel, V., and Hernquist, L. (2005). Energy input from quasars regulates the growth and activity of black holes and their host galaxies. *Nature*, 433(7026):604.
- [Dolag et al., 2015] Dolag, K., Gaensler, B. M., Beck, A. M., and Beck, M. C. (2015). Constraints on the distribution and energetics of fast radio bursts using cosmological hydrodynamic simulations. *Monthly Notices of the Royal Astronomical Society*, 451(4):4277–4289.
- [Dolag et al., 2004] Dolag, K., Jubelgas, M., Springel, V., Borgani, S., andasia, E. (2004). Thermal conduction in simulated galaxy clusters. *The Astrophysical Journal Letters*, 606(2):L97.
- [Dolag and Stasyszyn, 2009] Dolag, K. and Stasyszyn, F. (2009). An mhd gadget for cosmological simulations. *Monthly Notices of the Royal Astronomical Society*, 398(4):1678–1697.

- [Durrer and Neronov, 2013] Durrer, R. and Neronov, A. (2013). Cosmological magnetic fields: their generation, evolution and observation. *The Astronomy and Astrophysics Review*, 21(1):62.
- [Efstathiou et al., 1985] Efstathiou, G., Davis, M., White, S., and Frenk, C. (1985). Numerical techniques for large cosmological n-body simulations. *The Astrophysical Journal Supplement Series*, 57:241–260.
- [Ferriere, 1996] Ferriere, K. (1996). Alpha-tensor and diffusivity tensor due to supernovae and superbubbles in the galactic disk near the sun. *Astronomy and Astrophysics*, 310:438–455.
- [Gingold and Monaghan, 1977] Gingold, R. A. and Monaghan, J. J. (1977). Smoothed particle hydrodynamics: theory and application to non-spherical stars. *Monthly notices of the royal astronomical society*, 181(3):375–389.
- [Hanayama et al., 2005] Hanayama, H., Takahashi, K., Kotake, K., Oguri, M., Ichiki, K., and Ohno, H. (2005). Biermann mechanism in primordial supernova remnant and seed magnetic fields. *The Astrophysical Journal*, 633(2):941.
- [Harlow and Evans, 1955] Harlow, F. H. and Evans, M. (1955). A machine calculation method for hydrodynamic problems. *LAMS-1956*.
- [Hernquist, 1993] Hernquist, L. (1993). N-body realizations of compound galaxies. *The Astrophysical Journal Supplement Series*, 86:389–400.
- [Hirschmann et al., 2014] Hirschmann, M., Dolag, K., Saro, A., Bachmann, L., Borgani, S., and Burkert, A. (2014). Cosmological simulations of black hole growth: Agn luminosities and downsizing. *Monthly Notices of the Royal Astronomical Society*, 442(3):2304–2324.
- [Hockney and Eastwood, 1988] Hockney, R. W. and Eastwood, J. W. (1988). *Computer simulation using particles*. crc Press.
- [Hu et al., 2016] Hu, C.-Y., Naab, T., Walch, S., Glover, S. C., and Clark, P. C. (2016). Star formation and molecular hydrogen in dwarf galaxies: a non-equilibrium view. *Monthly Notices of the Royal Astronomical Society*, 458(4):3528–3553.
- [Iroshnikov, 1963] Iroshnikov, P. (1963). Turbulence of a conducting fluid in a strong magnetic field. *Astronomicheskii Zhurnal*, 40:742.
- [Jubelgas et al., 2004] Jubelgas, M., Springel, V., and Dolag, K. (2004). Thermal conduction in cosmological sph simulations. *Monthly Notices of the Royal Astronomical Society*, 351(2):423–435.
- [Katz et al., 1995] Katz, N., Weinberg, D. H., and Hernquist, L. (1995). Cosmological simulations with treesph. *arXiv preprint astro-ph/9509107*.

- [Kazantsev et al., 1985] Kazantsev, A., Ruzmaikin, A., and Sokolov, D. (1985). Magnetic field transport by an acoustic turbulence-type flow. *Zhurnal Eksperimental'noi i Teoreticheskoi Fiziki*, 88:487–494.
- [Kennicutt Jr, 1998] Kennicutt Jr, R. C. (1998). The global schmidt law in star-forming galaxies. *The Astrophysical Journal*, 498(2):541.
- [Kim et al., 2006] Kim, C.-G., Kim, W.-T., and Ostriker, E. C. (2006). Interstellar turbulence driving by galactic spiral shocks. *The Astrophysical Journal Letters*, 649(1):L13.
- [Kotarba et al., 2009] Kotarba, H., Lesch, H., Dolag, K., Naab, T., Johansson, P., and Staszczyn, F. (2009). Magnetic field structure due to the global velocity field in spiral galaxies. *Monthly Notices of the Royal Astronomical Society*, 397(2):733–747.
- [Kronberg et al., 1999] Kronberg, P. P., Lesch, H., and Hopp, U. (1999). Magnetization of the intergalactic medium by primeval galaxies. *The astrophysical journal*, 511(1):56.
- [Lazar et al., 2009] Lazar, M., Schlickeiser, R., Wielebinski, R., and Poedts, S. (2009). Cosmological effects of weibel-type instabilities. *The Astrophysical Journal*, 693(2):1133.
- [Lucy, 1977] Lucy, L. B. (1977). A numerical approach to the testing of the fission hypothesis. *The astronomical journal*, 82:1013–1024.
- [Marinacci et al., 2011] Marinacci, F., Fraternali, F., Nipoti, C., Binney, J., Ciotti, L., and Londrillo, P. (2011). Galactic fountains and the rotation of disc-galaxy coronae. *Monthly Notices of the Royal Astronomical Society*, 415(2):1534–1542.
- [McKee and Ostriker, 1977] McKee, C. F. and Ostriker, J. P. (1977). A theory of the interstellar medium—three components regulated by supernova explosions in an inhomogeneous substrate. *The Astrophysical Journal*, 218:148–169.
- [Miller and Bregman, 2013] Miller, M. J. and Bregman, J. N. (2013). The structure of the milky way’s hot gas halo. *The Astrophysical Journal*, 770(2):118.
- [Monaco, 2004] Monaco, P. (2004). Physical regimes for feedback in galaxy formation. *Monthly Notices of the Royal Astronomical Society*, 352(1):181–204.
- [Monaghan and Gingold, 1983] Monaghan, J. and Gingold, R. A. (1983). Shock simulation by the particle method sph. *Journal of computational physics*, 52(2):374–389.
- [Moster et al., 2010] Moster, B. P., Macciò, A. V., Somerville, R. S., Johansson, P. H., and Naab, T. (2010). Can gas prevent the destruction of thin stellar discs by minor mergers? *Monthly Notices of the Royal Astronomical Society*, 403(2):1009–1019.
- [Murante et al., 2014] Murante, G., Monaco, P., Borgani, S., Tornatore, L., Dolag, K., and Goz, D. (2014). Simulating realistic disc galaxies with a novel sub-resolution ism model. *Monthly Notices of the Royal Astronomical Society*, 447(1):178–201.

- [Murante et al., 2010] Murante, G., Monaco, P., Giovalli, M., Borgani, S., and Diaferio, A. (2010). A subresolution multiphase interstellar medium model of star formation and supernova energy feedback. *Monthly Notices of the Royal Astronomical Society*, 405(3):1491–1512.
- [Niklas, 1995] Niklas, S. (1995). PhD thesis, PhD Thesis, Univ. Bonn, (1995).
- [Pakmor and Springel, 2013] Pakmor, R. and Springel, V. (2013). Simulations of magnetic fields in isolated disc galaxies. *Monthly Notices of the Royal Astronomical Society*, 432(1):176–193.
- [Press and Schechter, 1974] Press, W. H. and Schechter, P. (1974). Formation of galaxies and clusters of galaxies by self-similar gravitational condensation. *The Astrophysical Journal*, 187:425–438.
- [Price, 2012] Price, D. J. (2012). Smoothed particle hydrodynamics and magnetohydrodynamics. *Journal of Computational Physics*, 231(3):759–794.
- [Robitaille and Whitney, 2010] Robitaille, T. P. and Whitney, B. A. (2010). The present-day star formation rate of the milky way determined from spitzer-detected young stellar objects. *The Astrophysical Journal Letters*, 710(1):L11.
- [Röttgers and Arth, 2018] Röttgers, B. and Arth, A. (2018). Sph to grid: a new integral conserving method. *arXiv preprint arXiv:1803.03652*.
- [Ryu et al., 1995] Ryu, D., Jones, T., and Frank, A. (1995). Numerical magnetohydrodynamics in astrophysics: Algorithm and tests for multi-dimensional flow. *arXiv preprint astro-ph/9505073*.
- [Salpeter, 1955] Salpeter, E. E. (1955). The luminosity function and stellar evolution. *The Astrophysical Journal*, 121:161.
- [Schleicher and Beck, 2013] Schleicher, D. R. and Beck, R. (2013). A new interpretation of the far-infrared–radio correlation and the expected breakdown at high redshift. *Astronomy & Astrophysics*, 556:A142.
- [Schlickeiser, 2012] Schlickeiser, R. (2012). Cosmic magnetization: from spontaneously emitted aperiodic turbulent to ordered equipartition fields. *Physical Review Letters*, 109(26):261101.
- [Schmidt, 1959] Schmidt, M. (1959). The rate of star formation. *The Astrophysical Journal*, 129:243.
- [Sharda et al., 2018] Sharda, P., Federrath, C., da Cunha, E., Swinbank, A., and Dye, S. (2018). Testing star formation laws in a starburst galaxy at redshift 3 resolved with alma. *Monthly Notices of the Royal Astronomical Society*, 477(4):4380–4390.

- [Springel, 2005] Springel, V. (2005). The cosmological simulation code gadget-2. *Monthly notices of the royal astronomical society*, 364(4):1105–1134.
- [Springel and Hernquist, 2003] Springel, V. and Hernquist, L. (2003). Cosmological smoothed particle hydrodynamics simulations: a hybrid multiphase model for star formation. *Monthly Notices of the Royal Astronomical Society*, 339(2):289–311.
- [Springel and White, 1999] Springel, V. and White, S. D. (1999). Tidal tails in cold dark matter cosmologies. *Monthly Notices of the Royal Astronomical Society*, 307(1):162–178.
- [Springel et al., 2005] Springel, V., White, S. D., Jenkins, A., Frenk, C. S., Yoshida, N., Gao, L., Navarro, J., Thacker, R., Croton, D., Helly, J., et al. (2005). Simulations of the formation, evolution and clustering of galaxies and quasars. *nature*, 435(7042):629.
- [Springel et al., 2001] Springel, V., Yoshida, N., and White, S. D. (2001). Gadget: a code for collisionless and gasdynamical cosmological simulations. *New Astronomy*, 6(2):79–117.
- [Stone et al., 2008] Stone, J. M., Gardiner, T. A., Teuben, P., Hawley, J. F., and Simon, J. B. (2008). Athena: a new code for astrophysical mhd. *The Astrophysical Journal Supplement Series*, 178(1):137.
- [Tabatabaei et al., 2013] Tabatabaei, F., Schinnerer, E., Murphy, E., Beck, R., Groves, B., Meidt, S., Krause, M., Rix, H.-W., Sandstrom, K., Crocker, A., et al. (2013). A detailed study of the radio-fir correlation in ngc 6946 with herschel-pacs/spire from kingfish. *Astronomy & Astrophysics*, 552:A19.
- [Toomre and Toomre, 1972] Toomre, A. and Toomre, J. (1972). Galactic bridges and tails. *The Astrophysical Journal*, 178:623–666.
- [White et al., 1996] White, S., Schaeffer, R., Silk, J., Spiro, M., and Zinn-Justin, J. (1996). Cosmology and large-scale structure. *Proceedings of Les Houches Summer School, R. Schaeffer et al., editors, (Elsevier, Amsterdam)*.
- [Xu et al., 2008] Xu, H., OShea, B. W., Collins, D. C., Norman, M. L., Li, H., and Li, S. (2008). The biermann battery in cosmological mhd simulations of population iii star formation. *The Astrophysical Journal Letters*, 688(2):L57.
- [Yepes et al., 1997] Yepes, G., Kates, R., Khokhlov, A., and Klypin, A. (1997). Hydrodynamical simulations of galaxy formation: effects of supernova feedback. *Monthly Notices of the Royal Astronomical Society*, 284(1):235–256.
- [Zeeman, 1897] Zeeman, P. (1897). Vii. doublets and triplets in the spectrum produced by external magnetic forces. *The London, Edinburgh, and Dublin Philosophical Magazine and Journal of Science*, 44(266):55–60.

Aknowledgments

First of all, I would like to sincerely thank my supervisor, PD Dr. Klaus Dolag for giving me the opportunity to work with him on this interesting project, for being available to answer all my questions, his generous patience, guidance, discussions and for providing me all the tools that I need to further continue my academic studies.

I would also like to genuinely thank Ulrich Steinwandel for always being willing to help me, guide me and encourage me even when he was a 9h flight away.

Many thanks to the whole CAST group, and its leader Prof. Andreas Burkert, for this delightful year, for all the interesting discussions either at a seminar room or around many liters of bier (and wine). Special thanks to Antonio for all the help with python, Alex for the power spectra and Tadziu for all the computing issues. Many thanks to Alkistis, Lisa and Ulli for further inputs and corrections of this manuscript.

Furthermore, I would like to thank my best friend Alkistis, Mario and my family for always being by my side and for the sincere encouragement and support.

Last but not least, I want to thank Magnetic Fields for existing and making Astrophysics more interesting.

Declaration:

I hereby declare that this thesis is my own work and that I have not used any sources and aids other than those stated in the thesis.

München, 20.08.2018

Eirini Batziou